THE EFFECT OF DIODE AND ARRAY GEOMETRICAL PARAMETERS ON PERFORMANCE OF HIGH FIELD ELECTRON EMITTERS FORMED FROM UNIDIRECTIONALLY SOLIDIFIED URANIUM DIOXIDE-TUNGSTEN COMPOSITES

A THESIS

Presented to

The Faculty of the Division of Graduate Studies

By

Wayne Laurance Ohlinger

In Partial Fulfillment

of the Requirements for the Degree

Doctor of Philosophy in the School of Ceramic Engineering

Georgia Institute of Technology

August, 1977

THE EFFECT OF DIODE AND ARRAY GEOMETRICAL PARAMETERS ON PERFORMANCE OF HIGH FIELD ELECTRON EMITTERS FORMED FROM UNIDIRECTIONALLY SOLIDIFIED URANIUM DIOXIDE-TUNGSTEN COMPOSITES

Approved:

Robert K. Feeney, Chairman

A. T. Chapman

Joe K. Cochran

Date approved by Chairman: 8/26/77

ACKNOWLEDGMENTS

I would first like to thank my advisor, Dr. R. K. Feeney, for his help and encouragement. His willingness to explain the mysteries of electronics to a poor Ceramic Engineer were appreciated.

Drs. A. T. Chapman and Joe K. Cochran have both been extremely helpful and their time spent in reading this manuscript and suggesting improvements deserves a special note of thanks.

It is difficult to express the enormous debt of gratitude owed to Tom Mackrovitch. Always willing to help with any problem, his efforts provided solutions to countless difficulties.

To my wife, Lynn, I am deeply indebted. Her support throughout graduate school was a constant source of inspiration.

Finally, to my grandfather, E. L. Wirt, and to my mother, I owe thanks for the stimulation to attain the level of education which I have now achieved.

TABLE OF CONTENTS

Page

ACKNOWLEDGMENTS ii

LIST OF TABLES v

LIST OF ILLUSTRATIONS vii

SUMMARY x

Chapter

I. INTRODUCTION 1

History
Survey of Literature
The Fowler-Nordheim Model
The Fowler-Nordheim Plot
Single Pin Geometries
Multi-Pin Cathode Arrays
Applications of Multi-Pin Emitters

II. PROCEDURE 37

Composite Growth
Emitter Fabrication
Experimental Apparatus
Vacuum Systems
Diodes
Electronics
Emitter Installation and Pumpdown Procedures
Diffusion Pumped System-Water Cooled Diode
Ion Pumped System-Variable Spacing Diode
Emitter Activation
V-I Data Collection
Interelectrode Spacing Test
Pin Tip Radius Test
Pin Packing Density Test
Gross Emission Tests
V-I Data Reduction

III. RESULTS AND DISCUSSION 72

Effects of Anode-Cathode Geometry
Effects of Interelectrode Spacing, Pin Tip
Radius and Pin Packing Density
Interelectrode Spacing

Page

Pin Tip Radius
Pin Packing Density
Performance Limitations

IV. CONCLUSIONS 139

V. RECOMMENDATIONS 144

APPENDIX

A. TABLES OF CONSTANTS AND NOMENCLATURE 148

B. RAW V-I DATA FROM INTERELECTRODE SPACING TESTS . 152

C. RAW V-I DATA FROM PIN TIP RADIUS TESTS 163

D. RAW V-I DATA FROM PIN PACKING DENSITY TESTS . . . 167

E. RAW V-I DATA FOR EXPERIMENTAL PLOT SAMPLE W-6 . . 170

F. RAW V-I DATA FOR EXPERIMENTAL FOWLER-NORDHEIM PLOTS, SAMPLE P-9 172

G. REPORT OF PRELIMINARY HEATING AND FIELD DESORPTION TEST RESULTS 175

BIBLIOGRAPHY. 179

VITA. 184

LIST OF TABLES

Table		Page
1.	Values of the Functions f(y), t(y) and s(y) . . .	12
2.	High Voltage dc Power Supplies Used	53
3.	Field Values from Resistance Paper Analog	80
4.	Experimental Fowler-Nordheim Plot Slopes with Experimental and Theoretical β Values for Interelectrode Spacing Test	89
5.	Reported Overall Work Function Values for Oxygen-Contaminated Tungsten	91
6.	Experimental Fowler-Nordheim Plot Slopes and Experimental β Values for Pin Tip Radius Test . .	100
7.	Comparison of Experimental and Theoretical β Values for Pin Tip Radius Test	101
8.	Experimentally Determined Emitting Area Radii . .	102
9.	Experimental Fowler-Nordheim Plot Slopes and Experimental β Values for Pin Packing Density Test	107
10.	Comparison of Experimental and Theoretical β Values for Pin Packing Density Test	108
11.	Calculated Current Densities and Gross Emission Currents for the Theoretical Array as a Function of Applied Field	112
12.	Data for Fowler-Nordheim Plot for Theoretical Array	116
13.	Assumed Distribution of Pin Tip Radii	123
14.	Fowler-Nordheim Data for Array with Assumed Distribution of Pin Tip Radii	124
15.	Summary of Conditions and Results for Several Gross Emission Current Tests Under dc Conditions	128

Table | Page

16. Summary of Conditions and Results for Several Gross Emission Current Tests Under Pulsed Conditions 132

17. Values of Appropriate Universal Constants . . . 149

18. Nomenclature 150

19. V-I Data Set No. 1 153

20. V-I Data Set No. 2 154

21. V-I Data Set No. 3 155

22. V-I Data Set No. 4 156

23. V-I Data Set No. 5 157

24. V-I Data Set No. 6 158

25. V-I Data Set No. 7 159

26. V-I Data Set No. 8 160

27. V-I Data Set No. 9 161

28. V-I Data Set No. 10 162

29. V-I Data Set for Sample R-1 164

30. V-I Data Set for Sample R-2 165

31. V-I Data Set for Sample R-3 166

32. V-I Data Set for Sample D-1 168

33. V-I Data Set for Sample D-2 169

34. V-I Data Set for Sample W-6 171

35. V-I Data Set for Sample P-9 at 0.285" Spacing . 173

36. V-I Data Set for Sample P-9 at 0.116" Spacing . 174

LIST OF ILLUSTRATIONS

Figure		Page
1.	Example of a Typical Fowler-Nordheim Plot	18
2.	Packing Effect for Arrays of 0.1 and 0.2 mm Diameter Wires (After Garber, et al.[7])	28
3.	Schematic Drawing of the Procedure for Producing an Emitter Array with Conically Pointed Pins	40
4.	Overall View of the Ion-Pumped Vacuum System With the Small, Variable-Spacing Diode in Place	45
5.	Overall View of the Diffusion-Pumped Vacuum System with the Water-Cooled Diode in Place	46
6.	Overall View of the Experimental Equipment Used for Pulse Testing with Large, Variable-Spacing Diode in Place	48
7.	Photograph of the Water-Cooled Diode	50
8.	Schematic Diagram of the Experimental Apparatus Used for Pulse Testing	52
9.	Typical Uncompensated Diode Current	55
10.	Typical Output Signal from Compensating Capacitor	55
11.	Typical Baseline Obtained by Subtraction of Signal Shown in Figure 10 from that Shown in Figure 9	56
12.	Typical Emission Current Waveform as Observed Without Capacitive Current Compensation	56
13.	Typical Emission Current Waveform as Observed Using the Compensating Capacitor	57
14.	Typical Waveform of the Applied Voltage	57
15.	Schematic Diagrams of the Diode Geometries Studied by the Resistance Paper Analog Method	74

Figure Page

16. Drawing of Typical Array Studied with Resistance Paper Analog Method (One-Half Size) 76

17. Potential Variation Above Edge Pin and Center Pin for Small Cathode-Large Anode 77

18. Potential Variation Above Edge Pin and Center Pin for Large Cathode-Small Anode 77

19. Potential Variation Above Edge Pin and Center Pin for Same Size Anode and Cathode 78

20. Potential Variation Above Edge Pin and Center Pin for Guarded Cathode 78

21. Logarithm of the Normalized Macroscopic Current Density as a Function of Pin Packing Density (ρ from 1×10^3 to 1×10^7 pins/cm^2) 84

22. Logarithm of the Normalized Macroscopic Current Density as a Function of Pin Packing Density (ρ from 1×10^3 to 3×10^5 pins/cm^2) 85

23. Scanning Electron Micrograph of the Sample Used in the Interelectrode Spacing test. x 2550 . . . 88

24. The Function s(y) as a Function of y 93

25. Experimental and Theoretical Values of β as a Function of Interelectrode Spacing 94

26. Scanning Electron Micrographs of the Samples Used in the Pin Tip Radius Test. (a) x 15050, (b) x 15750, (c) x 8190 97

27. Scanning Electron Micrographs of the Samples Used in the Pin Packing Density Test. (a) x 12000, (b) x 7900 105

28. Scanning Electron Micrograph of Sample W-6 . . . 110

29. The Image Correction Function f(y) as a Function of y 114

30. The Image Correction Function t(y) as a Function of y 115

31. Fowler-Nordheim Plots for Sample W-6 and the Theoretical Arrays 117

Figure Page

32. Fowler-Nordheim Plots Showing the Effect of a Distribution of Tip Radii 120

33. Assumed Distribution of Tip Radii 122

34. Emission Current versus Time for Sample W-6 . . . 125

35. Scanning Electron Micrograph of Emission Damaged Area on Sample W-6 Showing Typical Appearance of Damaged Pins. x 1580 127

36. Scanning Electron Micrograph of the Pot-Hole Structure. x 1060 131

37. Scanning Electron Micrograph of Sample P-12 . . . 135

38. Fowler-Nordheim Curves Plotted from Current and Voltage Decay Traces for Two Interelectrode Spacings, Sample P-9 136

SUMMARY

The use of unidirectionally solidified composite materials provides a unique opportunity to form high packing density (>1 x 10^6 pins/cm^2) arrays suitable for application as high-field electron emitters. Multiple-pin field emission cathodes show great theoretical promise to fulfill the need for a high current density (>10 A/cm^2) electron source. The purpose of this work was to assess the capabilities of UO_2-W composites applied as multi-pin field emission cathodes, to evaluate the effects of variation of certain geometrical diode and array parameters on emission performance, and to compare the experimentally demonstrated capabilities with theoretical predictions.

Results from three specific areas of investigation are presented. The first assesses the effects of anode-cathode geometry on emission performance, particularly the means by which diode design can influence the uniformity of the emission from the cathode. The second quantitatively determines the value of the field enhancement factor for the arrays as a function of interelectrode spacing, pin tip radius, and pin packing density. The results are compared with the theoretical predictions of the only available theory, and allow certain conclusions to be reached concerning the geometry of the emission sites. In the third portion of the

study the maximum macroscopic current density obtainable from the arrays is reported and compared with a realistic model developed on the basis of the experimental results. In this section several possible reasons for failing to reach the predicted performance levels are discussed, and the probable mechanism of failure which limits the achieveable current density is described.

Pulsed and dc modes of emitter operation were used in this research, and it is concluded that under the conditions of this investigation there are no differences between the two operating modes.

Macroscopic current densities of up to 1.2 are A/cm^2 demonstrated, and the effects of variation of diode and array geometry on the gross emission current are qualitatively reported. Only use of minimum interelectrode spacings is conclusively shown to have a beneficial effect on performance.

The model of the emission performance of the arrays developed on the basis of the experimental results predicts macroscopic current densities of up to 100 A/cm^2. The difference between the predicted performance and that experimentally observed is concluded to result from non-uniform current contribution from individual pins of the array. The percentage of pins contributing to the emission current is estimated to be one percent or less.

The model proposed here differs significantly from those previously presented by other investigators. All others

have assumed that the radii of the emitting areas are approximately equivalent to the pin tip radii as observed by the scanning electron microscope, i.e., in the range of 500Å to 5000Å. It is concluded in this work that the most probable value of the emitting area radii lies between 75Å and 285Å. Thus the emitting areas are shown to be much smaller than previously assumed.

Operation of the UO_2-W field emission cathode arrays has been demonstrated at levels commensurate with a limited number of commercial applications. Performance matching that of the best alternative sources has not been obtained. A reasonable theoretical model, however, demonstrated that such performance is readily within the capabilities of these arrays.

CHAPTER I

INTRODUCTION

The intent of this research was to investigate the field emission properties of multiple-pin arrays formed from unidirectionally solidified UO_2-W composites. There were three principal objectives. The first was to determine what the effect of the anode-cathode geometry was on the emission performance. The second was to quantitatively study the effects of interelectrode spacing, pin tip radius, and pin packing density on the field enhancement factor of the pins in an array. The third was to determine the maximum macroscopic current density obtainable from arrays of this kind, and to compare this value with available theoretical predictions.

Field emission from single tips has been thoroughly studied, and has proven to be a valuable scientific tool in numerous fields of investigation. To make field emitters a viable electron source for most engineering applications, however, the total current available must be increased significantly over that available from single pin emitters. The concept of using multiple pins to achieve this has been investigated by numerous workers, but few have utilized arrays of extremely high packing density, i.e., greater than 1×10^5 pins/cm^2. The few investigations reported have used unidirectionally solidified metal-metal composites and have been very

cursory.

This study represents the first quantitative comparison of experimental field emission performance of high density arrays with a valid theoretical model. It is also the first attempt to quantitatively determine the effects of the variation of diode and array parameters on the field enhancement factor. These effects are compared with the behavior predicted by the only available theory.

A brief history of the study of and advancements in field emission is included for introductory purposes. This section is followed by a comprehensive review of the Fowler-Nordheim theory and its development. A description of the general results reported by several workers using single-pin emitters is given; followed by a detailed look at the theoretical treatments of and experimental results from numerous investigators of multiple-pin field emitter arrays. The survey of the literature is completed by a brief description of a few of the applications in which use of field emitter arrays is currently being investigated.

The second chapter of this dissertation gives complete descriptions of all experimental techniques and apparatuses used. The growth process used for producing the unidirectionally solidified UO_2-W composites from which the field emitter arrays were formed is briefly described. Emitter fabrication is discussed in detail, and chemical etchant compositions developed in the course of earlier work by the author are presented.

Details of the two vacuum systems and three test diodes used are described, and all associated electronics for both dc and pulse testing are reported. The final sections of the Procedure delineate the exact data collection and data treatment technqiues which were used in the course of performing each of the various experiments.

The results of a theoretical investigation of the effects of anode-cathode geometry are reported. The results obtained in this portion of the study were important to the diode designs used in the subsequent experiments, and also proved to be valuable later in the discussion where an explanation of certain experimental results is provided by the findings of this initial investigation.

A series of experiments are reported in which the effects of interelectrode spacing, pin tip radius, and pin packing density on the field enhancement factor are studied. The conclusions reached in this portion of the investigation provide the basis for the final section of the discussion.

In this final section the theoretical capabilities of the arrays are defined on the basis of a model derived from the previously reported experimental results. The experimental results obtained from gross current emission tests are compared with this model, and it is evident that actual performance is far below expectations. The possible reasons for this discrepancy are discussed and conclusions drawn as to the most probable cause. The physical indications of individual pin failure are

reported.

All samples used in this research were unidirectionally solidified UO_2-W composite materials. The samples consisted of a uniform array of less than one μm diameter tungsten fibers arranged in parallel fashion within the uranium dioxide matrix. Fiber packing densities ranged from 2×10^6 to $20 \times 10^6/cm^2$.

History

The process by which electron emission is obtained from a metal or semiconductor due to the presence of a high electric field at the surface is called field emission. It was first observed by Wood[1] in 1897. A theoretical development based on quantum mechanical tunneling was published by Fowler and Nordheim[2] in 1928 and later modified by Nordheim[3] to account for the image-force. The modifications proposed by the latter provided good quantitative agreement with experimental results obtained by Dyke and co-workers.[4] Although current densities of up to 10^8 A/cm^2 have been realized before disruption of the field emitter tip by thermal proceses, the total current capable of being drawn from a single tip is limited to considerably less than one ampere due to the extremely small area available on the tip (radius typically of the order of 10^{-5} cm) if electric fields of the required level ($10^7 < E < 10^8$ V/cm) are to be achieved at reasonable operating voltages (25 kV or less).

One obvious approach to the problem of increasing the total available current is to increase the number of field emission tips, operating them in parallel with each providing an equal contribution to the total current. Multi-pin field emission arrays have been investigated by a number of workers. Dyke and co-workers[4,5] and Shirokov[6] utilized pocket-comb structures consisting of a small number of emitter tips (40 or less) arrayed in line along a common support wire. Garber, et al.,[7] have studied mechanically constructured arrays of 0.1 and 0.2 mm diameter tungsten wires, and Okulov, et al.,[8] have studied a mechanically constructed composite of 0.1 mm diameter W pins in a Cu matrix with a packing density of 3 x 10^3 pins/cm^2. Bugaev, et al.,[9] have studied serrated blades forming large area (200 cm^2) arrays of very low density (4 tips/cm^2). All of these consider multiple pin arrays of low density, <1 x 10^4 pins/cm^2. A thin-film sandwich structure array of 6.5 x 10^5 tips/cm^2 packing density has been developed by Spindt and co-workers[10]. Recently, unidirectionally solidifed eutectic composites have attracted the attention of several investigators since these materials provide considerably greater packing densities (of the order of 10^6 to 10^7 pins/cm^2) than those obtainable with the previously mentioned techniques.

Among the groups performing this work brief reports by Cline[11] on emission from the Ni-W eutectic, and Pfleiderer and Rehme[12] on emission from CrSb and NiSb needles in InSb matrices have appeared. Cline does not report the packing density of

the W pins in the Ni-W material, but from his published photomicrograph it is estimated to be approximately 10^7 pins/cm^2. Pfleiderer and Rehme report the density of the CrSb tips as 4×10^5 pins/cm^2 and that for the NiSb tips as 8×10^6 pins/cm^2.

More extensive investigations of the applications of unidirectionally solidified eutectics as multi-pin field emission arrays have been carried out by Feeney, Chapman and co-workers[13,14,15]. In contrast to other work using metal-metal eutectics the work of this group has used oxide-metal eutectics exclusively. Field emission has been reported from ZrO_2-W, Gd_2O_3-Mo and UO_2-W composite arrays. Use of samples with pin packing densities from 7.5×10^6 to 50×10^6 pins/cm^2 has been reported. The UO_2-W system has been utilized most extensively and has provided the best emission results. This fact is largely attributed to the relative ease with which a variety of pin tip geometries can be obtained, and a number of chemical etching, heating and ion milling techniques have been devised for this purpose. Current densities (referral to total array area) of up to 500 mA/cm^2 have been reported. Theoretical studies of the current densities available from these arrays have been developed using several simplistic models, and have estimated that current densities of over 100 A/cm^2 should be attainable.

Survey of Literature

Before delineating the extent of the literature available concerning field emission from multiple-pin arrays, it is

advantageous to outline the available field emission theory and the results of some of the investigations which have been performed utilizing single pins. Also a section is included concerning the potential significance and applications of the particular type of materials investigated in the present study.

The Fowler-Nordheim Model

The Fowler-Nordheim equation[2,3] provides a description of the field emission process from metals on the basis of the following assumptions:

1) The temperature of the metal is 0°K;
2) The free-electron approximation applies inside the metal;
3) The surface of the metal is smooth and uncontaminated;
4) The potential barrier near the surface consists of a classical image force potential and a potential due to the applied electric field.

The form of the potential barrier or the potential energy of an electron outside the metal ($x > 0$) is defined by,

$$V(x) = -\frac{e^2}{4x} - eEx \qquad (1)$$

where e is the electron charge, E is the applied electric field, and x is the distance from the metal-vacuum interface. The Fowler-Nordheim model is based upon tunneling through this potential barrier, and expresses the relationship between the current density, J; the applied field strength, E; and the work function, Ø. Only, W, the component of the energy of the

electrons inside the metal which is normal to the surface, i. e., in the x-direction, is considered.

A supply function, N(W) dW defines the number of electrons with the x-component of their energy in the range W to W + dW incident upon the barrier per unit area per unit time. The product of this supply function and an energy-dependent probability for penetration of the barrier, D(W), defines the number of electrons in the energy range W to W + dW which tunnel into the vacuum from the metal and is called the normal energy distribution:

$$P(W)\,dW = D(W)\,N(W)\,dW \tag{2}$$

The Fowler-Nordheim equation results from integrating the normal energy distribution over all accessible values of W;

$$J = e\int_{w_a}^{\infty} P(W)\,dW \tag{3}$$

where w_a = the electron energy at the bottom of the conduction band. It should be noted that although not true in a strict sense, the assumption is made that even though electrons are escaping from the metal, equilibrium of the electrons inside is assumed.

The supply function can be derived from the Fermi-Dirac energy distribution, and has the form:

$$N(W)\,dW = \frac{4\pi m_e kT}{h^3}\,\ell n\left[1 + \exp\left(-\frac{W-\phi}{kT}\right)\right]\,dW \tag{4}$$

where, k = Boltzmann's constant

h = Planck's constant

m_e = electron mass

T = temperature in °K

For low temperatures $|(W - \phi)/kT| >> 1$ and if $W \leq \phi$,

$$kT \ln [1 + \exp (- \frac{w-\phi}{kT})] = \phi - W,$$

yielding,

$$N(W)dW = \frac{4\pi m_e (\phi - W)}{h^3} . \tag{5}$$

The barrier penetration probability, $D(W)$, is found by solving the Schroedinger equation with the potential energy $V(x)$ as given in equation (1). Applying a WKB approximation[16] and manipulating gives,

$$D(W) = \exp [-c + \frac{W-\phi}{d}] \tag{6}$$

where

$$c = \frac{4(2m_e\phi^3)^{1/2}}{3\hbar eE} \tag{6a}$$

$$d = \frac{\hbar eE}{2(2m_e\phi)^{1/2}\, t(y)} \tag{6b}$$

$$t(y) = f(y) - 2/3\ y\ [\frac{df(y)}{dy}] \tag{6c}$$

and

$$y = \frac{(e^3E)^{1/2}}{\phi} \tag{7}$$

Substitution of the results obtained in (5) and (6) into (2) gives,

$$P(W)dW = \frac{4\pi m_e(\phi-W)}{h^3} \exp\ [-c + \frac{W-\phi}{d}]dW \tag{8}$$

and finally integrating over all W as indicated by (3) results in,

$$J = \frac{e^3E^2}{8\pi h\phi t^2(y)} \exp\ [-\frac{4(2m_e)^{1/2}\ \phi^{3/2}\ f(y)}{3\hbar eE}] \tag{9}$$

Substituting numerical values for all constants and expressing J in A/cm^2, E in V/cm, and ϕ in eV results in the following expression,

$$J = \frac{1.54 \times 10^{-6}E^2}{\phi t^2(y)} \exp\ [\frac{-6.83 \times 10^7\ \phi^{3/2}\ f(y)}{E}] \ . \tag{10}$$

Substitution of constants in equation (7) yields the following expression for y,

$$y = \frac{3.79 \times 10^{-4}\ E^{1/2}}{\phi} \tag{11}$$

The functions f(y) and t(y) appear in equation (10) as a result of inclusion of the image force. f(y) is an elliptic function defined by the following:

$$f(y) = 2^{-1/2} \sqrt{1 + \sqrt{1 - y^2}} \left[E(k^2) - (1 - \sqrt{1 - y^2})K(k^2)\right] \quad (12)$$

where K and E are complete elliptic integrals of the first and second kinds and,

$$k^2 = \frac{2\sqrt{1 - y^2}}{1 + \sqrt{1 - y^2}} . \quad (13)$$

t(y) is a function whose value is always near unity and is defined as shown previously (6a).

Values of f(y) were calculated be Nordheim[3] and corrected by Burgess, Kroemer, and Houston[17]; and values of t(y) have been reported by Good and Müller[18]. Their values of these functions for several values of y are reported in Table 1. Also given here are values of s(y), a function arising in the expression for the slope of a logarithmic plot of the Fowler-Nordheim equation, as reported by Burgess, et al.[17] The function s(y) and its significance will be discussed more thoroughly later.

It is appropriate at this time to consider several important points related to the field emission process. The first of these is the effect of temperature. The Fowler-Nordheim theory is developed assuming the metal to be at 0°K. This condition is unfulfillable in practice, however, and the effect of failing to fulfill this assumption must be considered. Increasing the temperature above 0°K will add a "thermal tail"

Table 1. Values of the Functions f(y), t(y), and s(y).

y	f(y)	t(y)	s(y)
0.00	1.0000	1.0000	1.0000
0.05	0.9948	1.0011	0.9995
0.10	0.9817	1.0036	0.9981
0.15	0.9622	1.0070	0.9958
0.20	0.9370	1.0111	0.9926
0.25	0.9068	1.0157	0.9885
0.30	0.8718	1.0207	0.9835
0.35	0.8323	1.0262	0.9777
0.40	0.7888	1.0319	0.9711
0.45	0.7413	1.0378	0.9637
0.50	0.6900	1.0439	0.9554
0.55	0.6351	1.0502	0.9464
0.60	0.5768	1.0565	0.9366
0.65	0.5152	1.0631	0.9261
0.70	0.4504	1.0697	0.9149
0.75	0.3825	1.0765	0.9030
0.80	0.3117	1.0832	0.8903
0.85	0.2379	1.0900	0.8770
0.90	0.1613	1.0969	0.8630
0.95	0.0820	1.1037	0.8483
1.00	0.0000	1.1107	0.8330

to the supply function (equation 5) elevating some electrons in the metal to energies greater than the Fermi energy. The effect of temperature, T, has been shown by Murphy and Good[19] to be defined by the following,

$$J(T) = J(0) \frac{\mu T}{\sin \mu T} , \tag{14}$$

where

$$\mu = \frac{\pi k}{d} . \tag{14a}$$

The value of d is as defined in equation (6b). The relative increase in the current, I, can be shown to be defined by,

$$\frac{\Delta I}{I} = 1.279 \times 10^{8} \frac{T^2 \phi t^2(y)}{E^2} \tag{15}$$

The effect on the emission is minimal for temperatures of less than 1000°K and is therefore not of concern in most field emission experiments.

Another important consideration is the energy-distribution of the emitted electrons. Young[20] has derived the Fowler-Nordheim equation using the total energy distribution to define the supply function rather than the normal energy distribution as used by Fowler and Nordheim.[2] This total energy distribution is of importance in electron optics problems concerned with non-planar geometries as noted by Young[20] and is considerably narrower than the normal energy distribution. The half-width of the total energy distribution as derived in the reference

cited above is σ (0) = 0.693d (again, d is as defined in equation (6b)) compared with a value of 2.45d for the normal energy distribution. A significant advantage of field emission devices over thermionic electron sources is recognizable when the total energy distribution of the latter is investigated. The same total energy supply function described above can be used for the thermionic case, and when integrated over all energies results in the Richardson-Dushman equation. The half width of the total energy distribution in this case is found to be 2.45kT. Since d and kT are numerically very nearly equal it is apparent that the half-width of the total energy distribution for field emission is about one-third that for thermionic emission. It should be noted that the advantage shifts to the thermionic sources in cases where the normal energy distribution is of importance. The normal energy distribution half-width for thermionic sources is 0.693kT, and is approximately one-third the width of that found for field emission sources. The actual numerical value of the total energy distribution half-width for a field emitter operating at a field of 6×10^7 V/cm with $\phi = 6.0$ and for the normal energy distribution half-width for a thermionic source at 3000°K and $\phi = 6.0$ is 0.18 eV.

Tha values of the energy distribution half-widths quoted above for field emission are theoretical values for a temperature of 0°K. From the earlier discussion of the effect of temperature on field emission it is apparent that increased temperature has an effect on the energy distribution as a result of

the "thermal tail" added to the supply function at energies above the Fermi level. Van Oostrom[21] has shown that a field emitter operating at a current density of 1×10^6 A/cm^2 should have a total energy distribution half-width of 0.158 eV at 0°K and 0.256 eV at 300°K. Experimental results in the same reference show excellent agreement with the predicted values. Based on the theoretical results of Young[20] previously mentioned a thermionic source would be expected to display a total energy distribution half-width approximately three times greater.

A final consideration important to field emitter operation is noise. Two primary types are of interest, shot noise and flicker noise. Noise measurements are usually expressed in terms of the mean square noise power which is related to the spectral density function W(f) (f is frequency). According to early work by Schottky[22] in regards to shot noise in thermionic emission, W(f) is independent of frequency and linearly dependent on the emission current. These effects have also been observed for field emission from clean surfaces over the frequency range 10^2-10^5 Hz and a factor of ten change in current.[23,24] The similarity between shot noise in thermionic and field emission sources is not unexpected. It is a modulation of the current density occurring as a result of the randomness in time of individual electron departures and the similarity of the supply functions for the two types of emission infers that this behavior should be observed. When adsorbed gas layers are present on the emission surface flicker noise

becomes dominant. It has generally been found to be related to f by,

$$W(f) \alpha 1/f^{\varepsilon}, \tag{16}$$

where $0.95 < \varepsilon < 1.2$ for gas adsorbates[24] and $0.8 < \varepsilon < 1.3$ for adsorbed potassium[25]. Gomer[26] has considered the noise generation mechanism for an adsorbed layer on a field emitter. His model consisted of deriving an expression for fluctuations in the work function and the instantaneous current. Fluctuations in work function were assumed to be caused by adsorbate concentration fluctuations. Further consideration was given to the generation of noise by adsorption state transitions and adsorption-desorption reactions. Swanson and Martin[27] present experimental evidence that the frequency and current dependence of the flicker noise can be described by the diffusion and state transition model of Gomer.

The Fowler-Nordheim Plot

In performing experimental field emission work, the gross current, I, in amperes and the potential difference between the anode and cathode, V, in volts can be measured directly. The Fowler-Nordheim relationship (10) as derived expresses current density, J, as a function of applied field, E, and work function, ϕ. Rewriting with the aid of the following expressions,

$$I = JA \tag{17}$$

and

$$E = \beta V, \tag{17a}$$

where A = emitting surface area in cm^2,

β = geometrical parameter in cm^{-1},

allows expression of I as a function of V, as follows,

$$I = \frac{1.54 \times 10^{-6} \beta^2 V^2 A}{\phi t^2(y)} \exp\left[\frac{-6.83 \times 10^7 \phi^{3/2} f(y)}{\beta V}\right]. \tag{18}$$

Although numerous investigators have used this equation in logarithmic form to plot log I as a function of V^{-1} obtaining essentially straight lines, it is more common to rewrite the equation as follows,

$$\log I/V^2 = \log\left[\frac{1.54 \times 10^{-6} \beta^2 A}{\phi t^2(y)}\right] - \frac{2.97 \times 10^7 \phi^{3/2} f(y)}{\beta V}. \tag{19}$$

A plot of log (I/V^2) versus $10^4/V$ as shown in Figure 1 is called the Fowler-Nordheim plot. A theoretical plot assuming constant values of ϕ, A and β will not of course produce a perfectly linear relationship due to the effect of the image force correction terms, but the deviation is minimal and for most experiments is undetectable.

The slope of this curve, m, at any point is given by

$$m = \frac{-2.97 \times 10^7 \phi^{3/2} s(y)}{\phi} \tag{20}$$

where

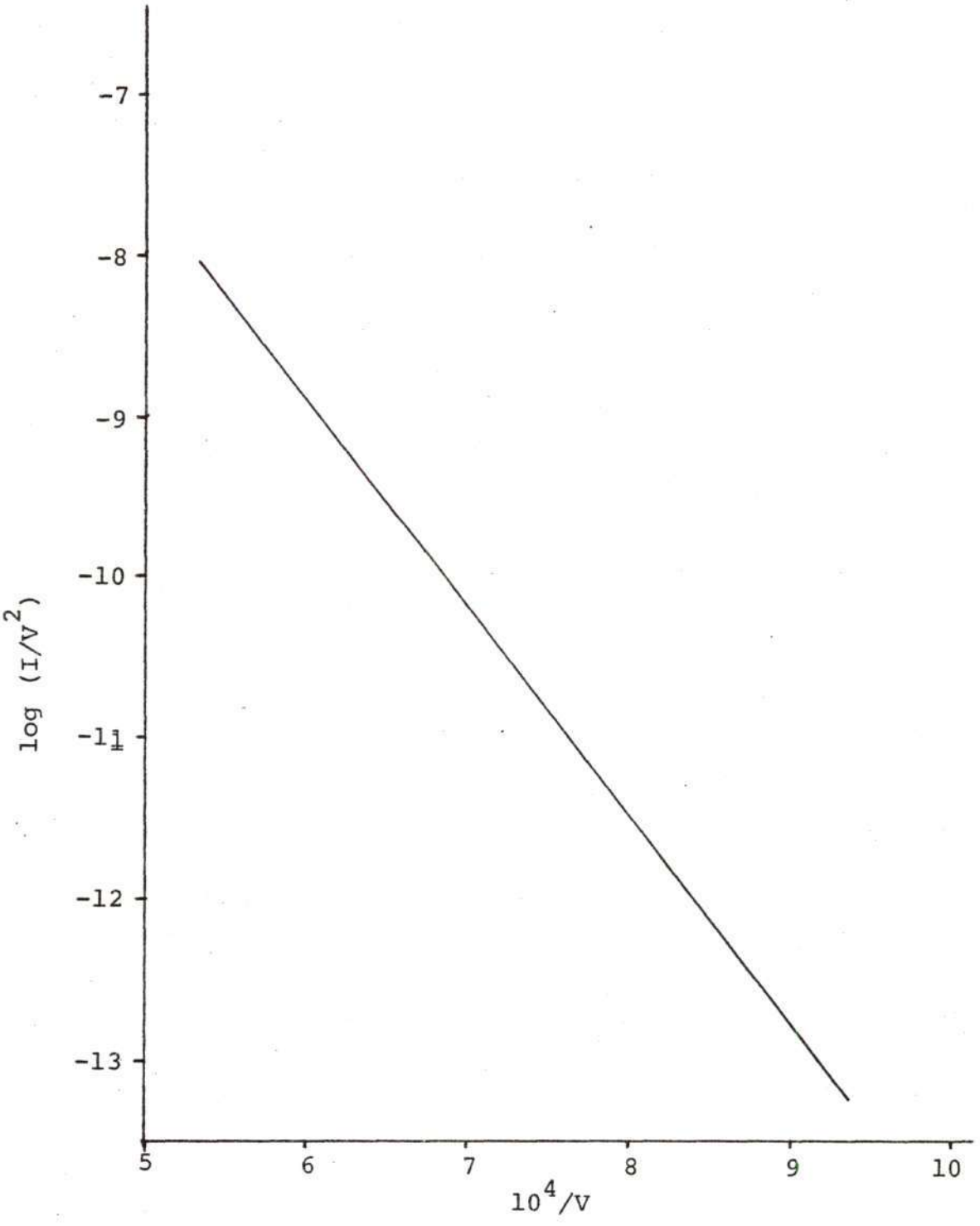

Figure 1. Example of a Typical Fowler-Nordheim Plot.

$$s(y) = f(y) - y/2 \left[\frac{df(y)}{dy}\right] . \qquad (20a)$$

The function s(y) is tabulated in Table 1 as previously noted. This equation allows the determination of ϕ or β if the other is known utilizing only the experimentally determined slope of the F-N plot.

Single Pin Geometries

From the Fowler-Nordheim model it is apparent that the performance of the field emitter is critically dependent upon two parameters, the work function ϕ and the electric field E. Considerations such as strength, high melting point, and availability in suitable form have lead most investigators to choose tungsten as the best suited material choice for field emitters. The work function is fixed by this selection at a fortuitously low value assuming a clean surface as stipulated for the Fowler-Nordheim model. It is then apparent that the remaining parameter under the experimenter's control is the value of the applied electric field. The field was defined previously (17a) as a function of the applied voltage and a parameter, β, which is dependent on the geometry of the emitter tip and the anode.

Several investigators, in attempting to verify the Fowler-Nordheim model, have devised methods of approximating the value and distribution of the field over the tip of an emitter. Müller[28] and Haefer[29] used a hyperboloid of revolution

and Becker[30] used a paraboloid of revolution arriving at the following expressions,

$$\beta = \frac{2}{r \ \ell n(2\ell/r)} \quad \text{for the paraboloid} \tag{21}$$

$$\beta = \frac{2}{r \ \ell n(4\ell/r)} \quad \text{for the hyperboloid,} \tag{22}$$

where ℓ = tip to anode distance

r = radius of curvature at apex.

Drechsler and Henkel[31] superimposed the potential gradient at the surface of a sphere onto that of a hyperboloid utilizing a form factor, α, defining the relative contribution of the sphere as a fraction of one and $1-\alpha$ defining the contribution of the hyperboloid. Their expression for β is then,

$$\beta = (\frac{\alpha}{r} + \frac{2(1-\alpha)}{r \ \ell n(4\ell/r)} \tag{23}$$

where $0 \leq \alpha \leq 1$

Dyke and co-workers[32] have utilized a model in which one of the equipotential surfaces surrounding a core formed by a sphere on an orthogonal cone can be made to fit the emitter profile as determined by electron microscopy. The field at this surface due to a potential applied between it and an anode described by another equipotential in the same system can be quite accurately calculated. Use of an anode essentially paraboloidal in shape is required to closely approach the calculated condition in an experimental set-up. This model has been utilized to give proof of the correctness of the Fowler-Nordheim theory to within 15% of the field, however,

fitting of an equipotential to an emitter profile using this method required considerable experimentation with three parameters.

Each of the methods mentioned above can be considered to be a modification of the equation for the field at the surface of a free sphere of radius, r, at potential, V, which is,

$$E = V/r. \tag{24}$$

In this case β then is equal to r^{-1}. At the apex of an actual tip the field is reduced from the value for the sphere due to the presence of a conical or cylindrical shank for which a general expression can be written as,

$$E = \frac{V}{kr} \tag{25}$$

and

$$\beta = \frac{1}{kr} . \tag{26}$$

k therefore is a factor which defines the degree of field strength reduction due to the shank of the pin and its influence on the field. It is expressed in the previous approximations by the following,

$$k = \frac{1}{2} \ell n(2\ell/r) \quad \text{for the paraboloid,} \tag{27}$$

$$k = \frac{1}{2} \ell n(4\ell/r) \quad \text{for the hyperboloid,} \tag{27a}$$

$$k = \frac{1}{\alpha} + \frac{\ell n(4\ell/r)}{2(1-\alpha)} \quad \text{for the spheroid-hyperboloid,} \tag{27b}$$

and has been reported by Charbonnier[33] and Swanson and Martin[27], all of Dykes' group, to follow the empirically derived relationship,

$$k = 0.59\ \varepsilon^{0.33}\ (\ell/r)^{0.13} \qquad (28)$$

where, ε = emitter cone half angle in degrees.

For accurate field calculations, such as those required for verification of the Fowler-Nordheim equation, it is necessary to utilize an experimental anode approximating an equipotential of the system used to match the emitter profile. However, the above equations do provide a reasonable estimate of k and β for a point at the apex of the assumed shape even under a flat anode. It is therefore possible to approximate the maximum value of β, i.e., that found at the apex of the pin, but considerably more difficult to accurately define the field distribution over the remainder of the tip.

Multi-Pin Cathode Arrays

The maximum currents obtained from single pin emitters are of the order of 0.5 A corresponding to operation at a current density approaching 10^8 A/cm^2. This performance is achieved only under pulse operating conditions utilizing duty cycles of 0.1%, and a reduction in current by a factor of 100 is necessary to assure reasonable lifetimes under 100% duty factor conditions. Thus for any applications involving operation under dc conditions requiring emission currents greater than a few mA the single pin emitter becomes impractical.

This limitation was noted quite some time ago and out of it grew the concept of multiple-pin field emitter arrays. Ideally the construction of an array of n pins should result in an increase in the maximum available field emission current by a factor of n for identical conditions of voltage and inter-electrode spacing; however, this is not realized in practice for the reasons discussed below.

It is apparent from the Fowler-Nordheim equation that the value of β must be matched from pin-to-pin within 1% if a variation in current density of no more than 10% is to be achieved. Since the value of β is directly dependent upon the tip radius (23) we see that a variation in r of less than 1% must be achieved on tips of $r < 0.1\ \mu m$. Inability to achieve this uniformity would have a drastic effect upon performance of the array. The pins of smallest tip radius would begin to emit at a lower applied voltage than their larger radiused neighbors, and could then exceed the maximum operating current density of approximately $10^6\ A/cm^2$ before other (larger radiused) pins began to emit significantly.

In addition to the potential problem of non-uniform emission, a significant increase in the voltage required to establish the needed field strength even at the tips of pins of comparable size would be expected. This results from the packing of the pins into an array. The packing effect is thoroughly described in the following discussion.

The theoretical treatment of the potential distribution

over an array of conducting pins in an insulating matrix is extremely complex and does not yeild an exact analytical solution for the electric field in terms of the geometrical parameters of the array. The related problem of the potential surrounding a square array of charged surface states on an insulating dielectric substrate has been considered by Levine[34]. The potential was determined by imaging the surface states through a grounded conducting planar anode and by solving the appropriate Poisson equation by using a harmonic mode expansion of the potential distribution in each cell, which consisted of a surface state and its image. The resulting undetermined coefficients in the series expansion were computed by applying the Neuman boundary conditions at every common cell interface. The resulting form of the solution for the potential distribution was a double Fourier series. These results have been applied to the pin array problem by Levine[35] and Norgard[36]. By utilizing the methods of reference 34 and making several simplifying assumptions, Levine has derived an expression for the value of β at the tip of an individual pin in an array as a function of the geometrical parameters of the pin and array. It is expressed as follows,

$$\beta = \frac{1}{r(1 + \alpha)} , \qquad (29)$$

where $\alpha = \frac{4\pi dr}{a^2}$

and d = interelectrode spacing,

r = pin tip radius,

a = pin tip separation distance.

In this analysis, the effect of pin height was not considered, thus the value of β calculated for given values of d, r, and a probably represents the upper limit value of β, corresponding to a pin height sufficient to assure that all electric flux lines are gathered to the pin tips and none reach the pin shank or the matrix surface.

Norgard[36] has implemented the solution to the Laplace equation on a high speed computer and obtained a numerical solution for the potential distribution in the interelectrode space. Testing of this technique using simple geometries for which the exact, analytical solution is available show good convergence. The numerical technique has been utilized to solve the case for a single pin located on a flat substrate under a flat anode, and studies have been made of the effect on β of varying the tip shape from that of a prolate spheriod to that of a hemisphere. Limitations in computer capacity made it impossible to extend the grid size to that required to define a multiple-pin array with the necessary precision. As a result of this limitation, it proved impossible to apply this technique directly to a study of the effects of packing pins into an array. Instead, a simple consideration identical to the concepts used by Pfleiderer and Rehme[12] was applied and field enhancement factors reported as a function of pin height and pin radius for packing densities of 1×10^6 and 2×10^6

pins/cm^2 assuming a prolate spheroidal tip.

The only other investigation of this type found in the literature was that of Pfleiderer and Rehme[12] reported in conjunction with their work on eutectic composites which was noted previously. They assumed ellipsoidal spikes and calculated the potential distribution around an isolated spike. Rather than calculating the potential distribution over a spike array, they then added an approximate consideration for the packing effect based essentially on the mean environmental anode area attributable to each spike and the cross-sectional area of the spike. As opposed to Levine's treatment, the authors were able to obtain an expression describing the effect of pin height but neglecting the interelectrode spacing. It should be noted that the field enhancement factor as defined by Pfleiderer and Rehme and Norgard differs from the usual definition which was reported in Equation 14a. The field enhancement factor, ξ, as defined by these authors is a dimensionless parameter which is multiplied by the flat-plate field, F= V/d, to define the field strength at the tip of a spike as given by the following equation,

$$E = \xi \, V/d \tag{30}$$

where V = applied potential,

d = interelectrode spacing.

Experimental works attempting to determine the applicability of the available theoretical treatments described above

are extremely limited in numbers and depth. Pfleiderer and Rehme[12] have calculated the values of ξ for their InSb-NiSb and InSb-CrSb arrays and have attempted to show that the macroscopic flat-plate field, i.e., $F = V/d$, required for the onset of field emission can be predicted. They assume that field emission will occur at a field, $E = \xi V/d$, of 1×10^7 V/cm and on this basis predict a macroscopic field of 1.7×10^5 V/cm should be required.

Their experiments with InSb-CrSb, however, showed that a field of 1.4×10^5 V/cm was sufficient to give an array current density of 2 mA/cm^2. No information or consideration was given concerning the work functions of the materials studied, and this factor in itself could make the assumed field required of 1×10^7 V/cm open to question. One observation of these authors which should be noted, however, is that only a small number of pins, five percent or less, contributed to the emission current.

Garber, et al.[7], showed the effect of packing on performance of arrays formed from 0.1 mm and 0.2 mm diameter W wires by assessing the increase in voltage necessary to achieve comparable operation of each individual needle in an array versus that required for an identical single pin. Their results are shown in Figure 2 where the dependence of β, defined as the ratio of the working voltage for the array to the working voltage of an isolated needle, on linear packing density of the needles is illustrated. It is important to remember that

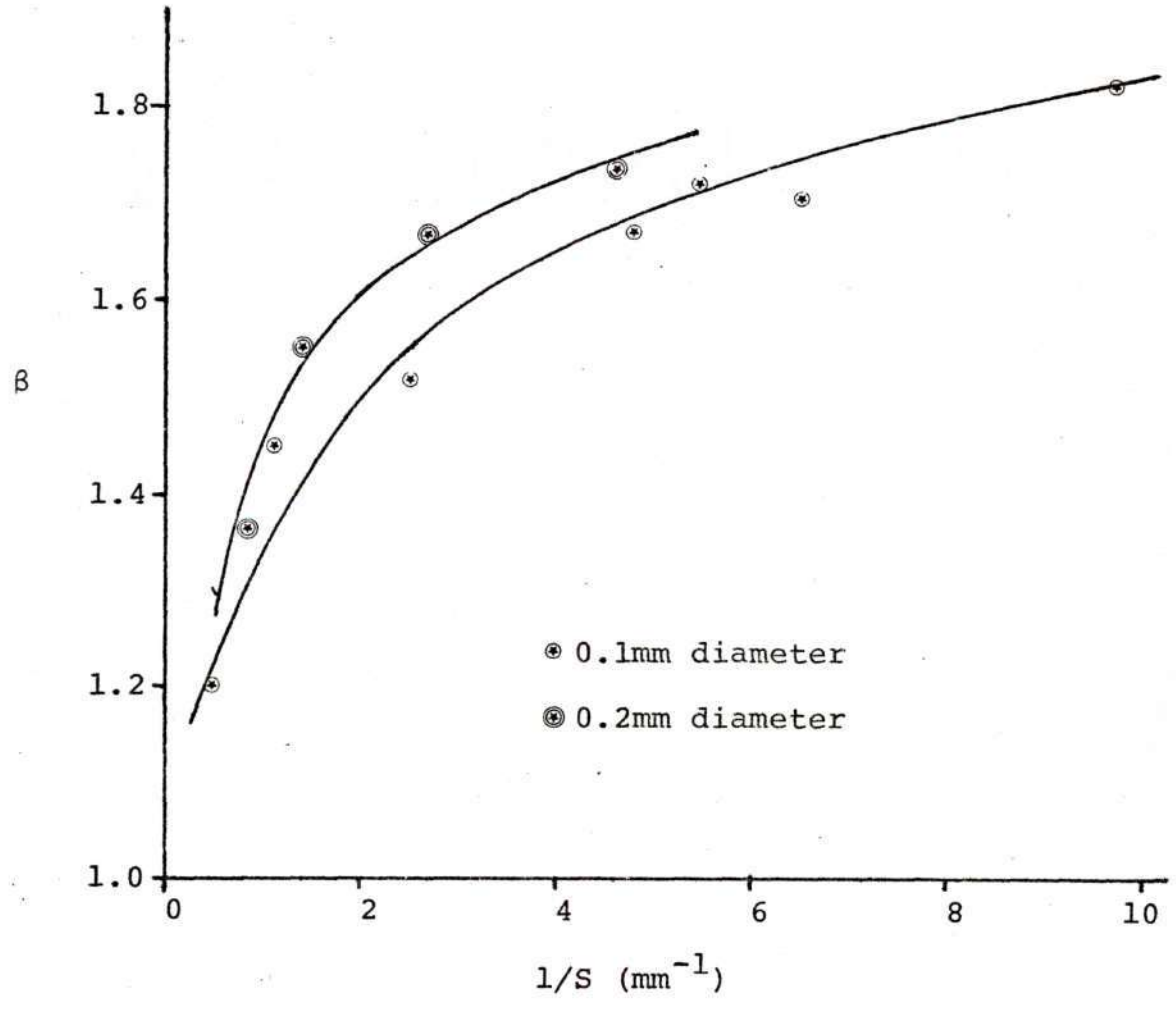

Figure 2. Packing Effect for Arrays of 0.1 and 0.2mm Diameter Wires. S is the distance between emitter points. (After Garber, et al.[7])

the maximum packing density achieved in these mechanically constructed arrays is 1×10^4 pins/cm^2, and that this is approximately 5×10^2 times lower than the minimum density available in the UO_2-W system.

Bugaev, et al.[9], have used the method of conformal mapping to obtain a simple, analytical expression for the field amplification factor at emitters formed from blades and then add a secondary factor for the effect of addition of rounded tips to the blade edges. This expression is applicable only to this peculiar serrated blade geometry and for extremely low tip packing densities of about four tips/cm^2. The expression for μ_1, or the amplification factor of the blade is as follows (in the author's notation),

$$\mu_1 = \frac{\sqrt{b/\pi r} + 1/\sqrt{b/\pi r}}{\frac{1 - H}{d} + bd^{-1}\pi^{-1}\ell nr} , \qquad (31)$$

where d = interelectrode spacing,

b = blade separation distance,

r = radius of blade edge,

H = blade height,

and under the conditions of $H/d \leq 1/3$, $b/d \leq 1$, $r/H << 1$, $r/d << 1$ and $H/b \geq 1/2$. The amplification factor for the tips on the blade edges, μ_2, is found from equation (28) by substitution of R, the tip radius, for r and l, the distance between tips, for b. The overall field enhancement factor, μ, is then defined as the product, $\mu_1 \mu_2$. Utilizing this expression to

calculate the total expected emission current for a given set of operating conditions, it was found that the expected result was a factor of two greater than that experimentally observed. This was assumed to be the result of considerably less than 100% of the pins actually producing emission current.

The studies mentioned above constitute the only theoretical and experimental treatments of the effects of packing of field emission tips to form arrays which are readily available in the literature. Several other authors have reported on field emission from arrays in less specific terms and the reports of these follow.

Dyke and Dolan[4,5,37] have reported the results of dc and pulse operation of pocket-comb structures consisting of up to 40 tips arrayed in line along a support wire. The largest arrays tested gave up to 30A at 100 kV under pulse operating conditions. In order to realize the highest reported currents, it was necessary to operate with pulse durations of no more than one microsecond.

Shirokov[6] also reported on field emission from pocket-comb structures very similar to those of Dyke and Dolan consisting of ten and 23 points. Operation of the ten pin comb under dc conditions yielded approximately 3 mA and pulse operation (pulse duration of 1-2 μsec) of the 23 point sample yielded nearly 1.5 A.

Several Russian investigators since Shirokov have reported extremely high emission currents from arrays. It

should be noted that the process whereby these current levels are achieved is not a pure field emission process, but is referred to as explosive electron emission. It consists, in essence, of creating a positive plasma in the neighborhood of the emitting tips by ionization of material evaporated from the emitter. This plasma serves to enhance the local electric field, greatly increasing the emission current density. Operation at these current densities for extended periods is, of course, impossible and extremely short pulse durations of about ten ns must be utilized. A slight loss of material from each tip is incurred with each pulse and this factor ultimately limits the lifetime and performance due to tip rounding and loss of complete tips.

Although performance of these emitters is not comparable to those of this study, a few of the reported results will be given for general information on emission from arrays. Garber, et al.[7], in the reference previously cited for study of the packing effect has reported currents of up to 500 A at 200 kV from an array of 1200 needles. It is of interest to note that field evaporation of material from the tungsten needles was utilized to improve the pin-to-pin geometrical uniformity with apparent success. It is unclear whether explosive emission was the actual process utilized in this study, but in any event the use of 200 ns wide pulses certainly contributed to the high performance levels achieved.

Other investigators including Fursei, et al.[38]; Gleizer

and Okulov[39]; and Okulov, et al.[8], have used a variety of multi-pin arrays to obtain emission currents of 200 to 630 A at voltages of 50 to 200 kV. All of these devices have utilized mechanically constructed arrays of relatively low density and have been operated under pulse conditions in the explosive emission mode.

One other brief report of utilization of a eutectic composite structure has appeared in the literature. Cline[11] studied field emission from a Ni-W structure of approximately 10^7 pins/cm^2 packing density. The Fowler-Nordheim characteristic of the device is given before and after arcing, and a maximum emission current of two mA is reported. No details of the spacing used in the test diode are given, but applied voltages of one to four kV yielded currents of 2×10^{-9} to 2×10^{-3} A. A cathode area of approximately two cm^2 can be inferred from the stated values of maximum current and current density and a maximum applied macroscopic field of 1×10^5 V/cm is reported. It appears that a macroscopic field of 3.5×10^4 V/cm was required to establish a field emission current of 2×10^{-9} A. Effects of variation of any array or diode geometrical parameters were not studied.

Feeney, Chapman and co-workers[13,14,36,40] studied field emission from a number of unidirectionally solidified eutectic materials, including ZrO_2-W, Gd_2O_3-Mo and UO_2-W. Good theoretical treatments of the effects of pin tip radius, pin tip separation, and interelectrode spacing based on the approach

given by Levine[34,35] were presented[40]. This analysis very adequately demonstrated the importance of these parameters in determining the macroscopic current density (current per unit area of array surface) which these arrays are theoretically capable of producing. Extensive experimental work was also reported showing an inability to realize the potential of these materials, but no comparison of experimental results with the predictions of the theory, in a qualitative or quantitative fashion, was reported. Samples tested in simple diode geometries have demonstrated the ability to operate for several thousand hours at macroscopic current densities up to 500 mA/cm^2.[41] Recent analysis of the data presented in reference 14 indicates that macroscopic current densities of 20 A/cm^2 may have been obtained under pulse operating conditions, and recent work has led to achievement of 10 A/cm^2 under dc conditions utilizing extremely small area arrays.[42]

Two other multi-pin field emitters bear mentioning although their operation is equivalent to simultaneous, parallel operation of multiple single pin emitters. The first of these is the thin-film sandwich structure produced by vapor deposition of an insulating dielectric layer, a conducting anode layer, and an emitter tip onto a conducting substrate developed by Spindt and co-workers[10]. Macroscopic current densities of up to ten A/cm^2 and lifetimes of up to 7000 hours at three A/cm^2 have been reported. This technology has been used to produce arrays of up to 5000 cathodes at packing

densities of 6.4×10^5 tips/cm^2. Recent work by Cochran and co-workers[43] has produced a similar structure utilizing the same UO_2-W material as studied by Chapman, et al.[14,36,40,42] A vapor deposition process is used to apply an insulating layer and an anode layer to this material using the <1 μm diameter tungsten pins of the compoiste as the emitting tips. Work on this emitter structure has just begun and no electrical performance data has been reported. Emission levels similar to those reported by Chapman, et al., are expected at substantially reduced operating voltages. It is largely the ability to achieve adequate emission currents at applied potentials of <200 V, as compared to one to 25 kV for other field emitters, which makes these two schemes attractive.

It is apparent from the foregoing discussion of multi-pin field emitter arrays that they theoretically promise and have to some extent experimentally shown enormous capability for utilization in a variety of applications and devices. The following section will outline a few of the present and proposed applications.

Applications of Multi-Pin Emitters

Use of tungsten brush or comb structures in production of high intensity x-ray beams was reported by Dyke[5,37] and Shackelford.[44] This technique was especially applicable in flash radiography. Dyke[37] also reported the application of similar structures in triodes and tetrodes in the rf and microwave ranges.

Cason, Dezenberg, and Huff[45] used blade-type cold cathodes in an electron-beam controlled CO_2 laser and have proposed and investigated the use of a multi-tip field emission array[14] for the same application. The previously described serrated blade geometry of Bugaev, et al.[9], was used for the same purpose.

Much of the Russian work related to production of high-perveance, relativistic charged-particle beams was summarized by Hendricks and Cassel,[46] and the success of this work has been evidenced in a recent review article.[47]

Bowden, et al.[48], described the possibility of using the eutectic composite arrays utilized in the present investigation for initiation of a thermonuclear reaction. It is not specified that a field emitter was used, but in a recent article[49] the electron beam initiated release of thermonuclear energy is reported.

A somewhat less esoteric, but nonetheless interesting, potential application has been reported by Levine.[50] This involves the application of a field emitter array in a flat plate television display, with the major advantages being tremendous size reduction of the display assembly and the ability to retain the instant-on characteristics of modern television designs without the need for continuous power consumption.

Replacement of the oxide or dispenser type cathodes presently used in microwave power tubes probably represents

the potential application for field emission arrays with the greatest commercial significance. Several investigators[51,52,53] are presently testing the Georgia Tech type composite arrays with microwave tube applications in mind. Improvement of previously reported current density values[41] by less than a factor of ten would make these materials competitive. An additional advantage of the field emitter arrays may be the narrowness of the total energy distribution, but this facet of their performance requires experimental verification. Thorough life testing at high current densities has not been performed, but studies reported to date have been encouraging.[41]

Although these are by no means all of the possible applications of these novel materials, the reader should realize from this brief summary the tremendous potential and numerous applications which cannot now be anticipated.

CHAPTER II

PROCEDURE

This chapter describes the equipment and the procedures used for obtaining and processing data. Before presenting this information, however, it is appropriate to provide a description of the composite materials studied and the process by which they are fabricated. This information is included for completeness and detailed descriptions of the growth process can be found elsewhere.[40,54,55,56]

Composite Growth

The composites; consisting of a UO_2 matrix containg from 2×10^6 to 20×10^6 less than one μm diameter W fibers per cm^2, were grown from near eutectic compositions using a direct rf-heating internal floating zone technique. The usual containment and contamination problems were eliminated, since the molten material is self-contained by its unmelted outer surface. Very uniform composites were produced because of the well-defined liquid-solid interface associated with the inherent steep temperature gradient.

The samples, from which emitter structures were formed, were fabricated by first dry mixing the desired proportions of high-purity UO_2 and W powders. The mixture was pressed into a cylindrical rod 19 mm in diameter by about 38 mm in length,

and sintered inside an inductively heated Mo preheat tube using rf heating at 3.5 MHz. A dynamic atmosphere of N_2 and/or CO/CO_2 flowed through the quartz containment tube to provide the low oxygen potential environment necessary to prevent the oxidation of the metal powder in the rod and the Mo preheat tube. Preheat temperatures of 1500°C were required to sinter the sample rods and to increase their electrical conductivity sufficiently for direct rf heating when the Mo preheater tube was lowered out of the rf field. Direct heating further increased the temperature until the interior of the rod melted. The high radiant heat loss from the surface of the rod and the relatively low thermal conductivity of the oxide-metal mixture produced a steep thermal gradient across the skin of the rod and maintained a surface temperature well below the melting point of the oxide-metal eutectic.

Unidirectional solidification was achieved by moving the molten zone upward through the rod at 0.5-4 cm/hr. A cavity formed over the molten zone because of the difference in density between the porous sintered rod and the nearly void-free solidified composite.

During the lowering of the rod, the oxide-metal mixture melted from the roof of the cavity, ran down the interior walls of the pellet into the molten pool, and was unidirectionally solidified at the base of the molten zone. To prevent thermal cracking, the rod was lowered into the Mo preheat tube which was repositioned in the lower turns of the induction coil to

act as a postheater operating at 1500°C. After the rod was lowered several cm, the Mo tube was raised to heat the entire length of the rod and control its rate of cooling.

Suitable selection of growth conditions formed structures containing between 2×10^6 and 20×10^6 fibers/cm^2 with fiber diameters between 0.2 and 0.8 μm.

Emitter Fabrication

Slices of material approximately 0.5 to 1.0 mm in thickness were cut from the cylindrical unidirectionally solidified UO_2-W rods using a Buehler Isomet Low Speed Saw (Model 11-1180) with a diamond blade. Grinding on successively finer grades of silicon carbide paper (240, 320, and 600 grit) followed by final polishing with one μm diamond paste prepared the samples for inspection by optical microscopy and assessment of growth characteristics. Once a sample of suitable uniformity had been selected a photomicrograph was taken at 945X to determine the fiber density by counting the fibers in a measured area.

To provide electrical contact to the composites and convenient mounting in the test diode all samples were brazed with copper to mulybdenum support pins, generally of 1/4 inch diameter. This procedure involved an initial etching (2-5 minutes in etchant A, composition of which is given below) to remove 2-3 μm of the UO_2 matrix, and subsequent brazing performed by rf induction heating in a H_2 atmosphere. A sketch of the sample and support structure is shown in Figure 3 (a). After brazing

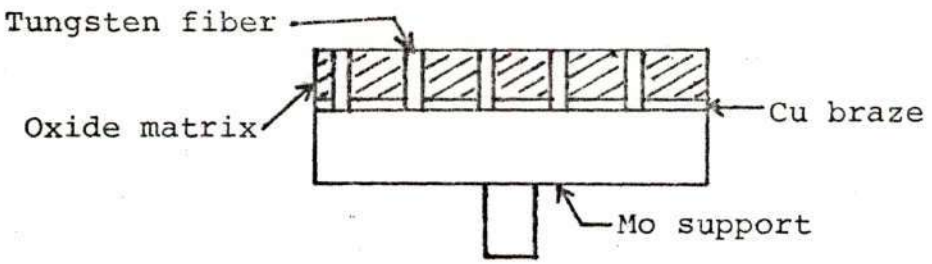

a) The Brazed Structure

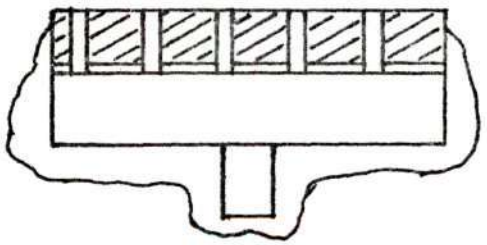

b) With the Insulative Pariffin Coating

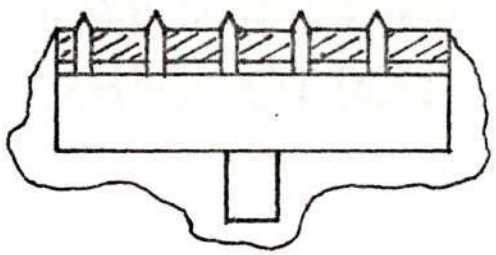

c) After Application of Etchant A

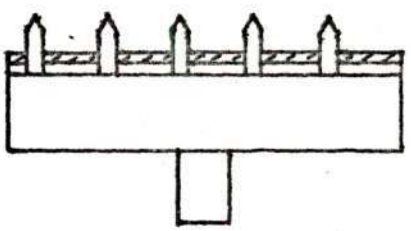

d) After Application of Etchant B and Removal of Paraffin

Figure 3. Schematic Drawing of the Procedure for Producing an Emitter Array with Conically Pointed Pins.

the sample was repolished on one μm diamond paste in preparation for chemical etching.

The etching procedure utilized etchants based on compositions by Bassi and Camona[57] and Manley[58]. Details of the etching procedure have been published elsewhere[36] but the technique is described here briefly.

Proper etching of the brazed samples required application of an insulative coating to all parts of the structure except the surface intended to be etched. This was accomplished by dipping into molten paraffin.

Two types of pin geometries were created by chemical etching, one consisting of blunt cylindrical pins and the other of conically pointed pins. The former were the result of a single step etching procedure using the following etchant (composition A),

40 ml chromic acid (saturated aqueous solution of CrO_3)
20 ml glacial acetic acid
6 ml concentrated nitric acid
4 ml 48% hydrofluoric acid.

Etching was performed by mounting the sample in a pair of tweezers affixed to the shaft of a suitably geared electric motor, and rotating the sample in the beaker containing the etchant at 20 rpm. The rate of removal of the matrix was approximately 8 μm in 30 minutes. All samples were etched for 30 minutes or longer yielding fiber heights of 8-12 μm.

Conically pointed fibers were produced by a two step etching procedure, which is shown schematically in Figure 3. Starting with the brazed structure, 3(a), the sample was first paraffin coated as previously described, 3(b). The first etching accomplished in the following etchant (composition B) for 30 to 40 minutes yielded short (2-4 μm) conical tips as shown schematically in 3(c).

30 ml chromic acid (saturated aqueous solution of CrO_3)
20 ml glacial acetic acid
14 ml concentrated nitric acid
11.5 ml 48% hydrofluoric acid

Following a brief rinse in deionized water and drying with methanol, the sample was etched for an additional 30 minutes in etchant A, yielding conically pointed pins 10-12 μm in height, 3(d).

After either etching process the sample was thoroughly rinsed in deionized water by rotation for 10-20 minutes. This was followed by several hours of immersion in benzene to remove the paraffin coating, and a final thorough rinse in methanol.

The support sturcture was designed to be compatible with the stage of a scanning electron microscope, and either a Cambridge Steroscan or a Coates and Welter Cwikscan Model 100-4 was used to inspect the sample before installation in the emission test diode.

Experimental Apparatus

Three types of experimental test diode structures were used in the course of this research mounted on two distinctly different vacuum systems. In general the same electronic apparatus was used for all dc testing regardless of the diode geometry, and the pulse testing electronics were used in conjunction with a diode specifically designed for this high voltage testing.

Vacuum Systems

For pulse emission testing and tests related to study of the effect of interelectrode spacing on the field enhancement factor a Veeco Mag Ion (Model MI-150) pump of 150 ℓ/s capacity was used to maintain a pressure of 5×10^{-9} torr or lower. The system pressure was monitored by means of the ion pump current and its relationship to pressure according to the manufacturer's published data. This system was rough pumped by a Varian VacSorb (Model 941-6001) pump cooled by liquid nitrogen. Isolation of the system from the roughing pump was provided by a Granville-Phillips gold-seal ultra-high vacuum valve (Series 204). A stainless steel cross with 2.75 inch Conflat flanges was mounted on top of the ion pump, and the remaining branches were utilized for the roughing pump, an electrical current feedthrough and the glass enclosure tube containing the diode structure. The enclosure tubes used were of two sizes, but otherwise were similar. For the pulse emission testing a 2.5 inch o.d. pyrex glass tube approximately

20 inches in length with glass-to-Conflat-flange transitions at each end was used. A smaller 1.5 inch o.d. tube about two inches in length and of similar construction was used for the dc tests with this vacuum system. This system with the smaller of the two enclosure tubes in place is pictured in Figure 4. The entire system was constructed of glass and stainless steel, and all seals were of the copper-gasketed Conflat type. The ion pump was baked by internal heaters, while the vacuum plumbing and glass tube were baked by electric heating tapes. Normal bakeout temperature was about 150°C.

The second vacuum system, utilized for the tests concerning effects of pin tip radius and pin packing density, as well as general testing for maximum emission current density, was pumped by a Consolidated Vacuum Company type PCMU-4B four inch oil diffusion pump. This was backed by a Sargent-Welch mechanical vacuum pump (Model 1402). A CVC type BCRU-40 water-cooled chevron baffle and a type TSMU-40 zeolite molecular sieve trap were used between the diffusion pump and the experiment chamber. The chamber was a stainless steel cross mounted on a table as shown in Figure 5. All vacuum system components were below the table. The chamber was closed by nine-inch ASA type flanges, one of which was used as the mounting and support for the diode structure. All vacuum chamber seals were of the aluminum o-ring or Conflat type. Bakeout was by electric heating tapes at temperatures of 150°-180°C, and pressures of 5×10^{-9} to 3×10^{-8} torr (monitored by a Bayard-Alpert type

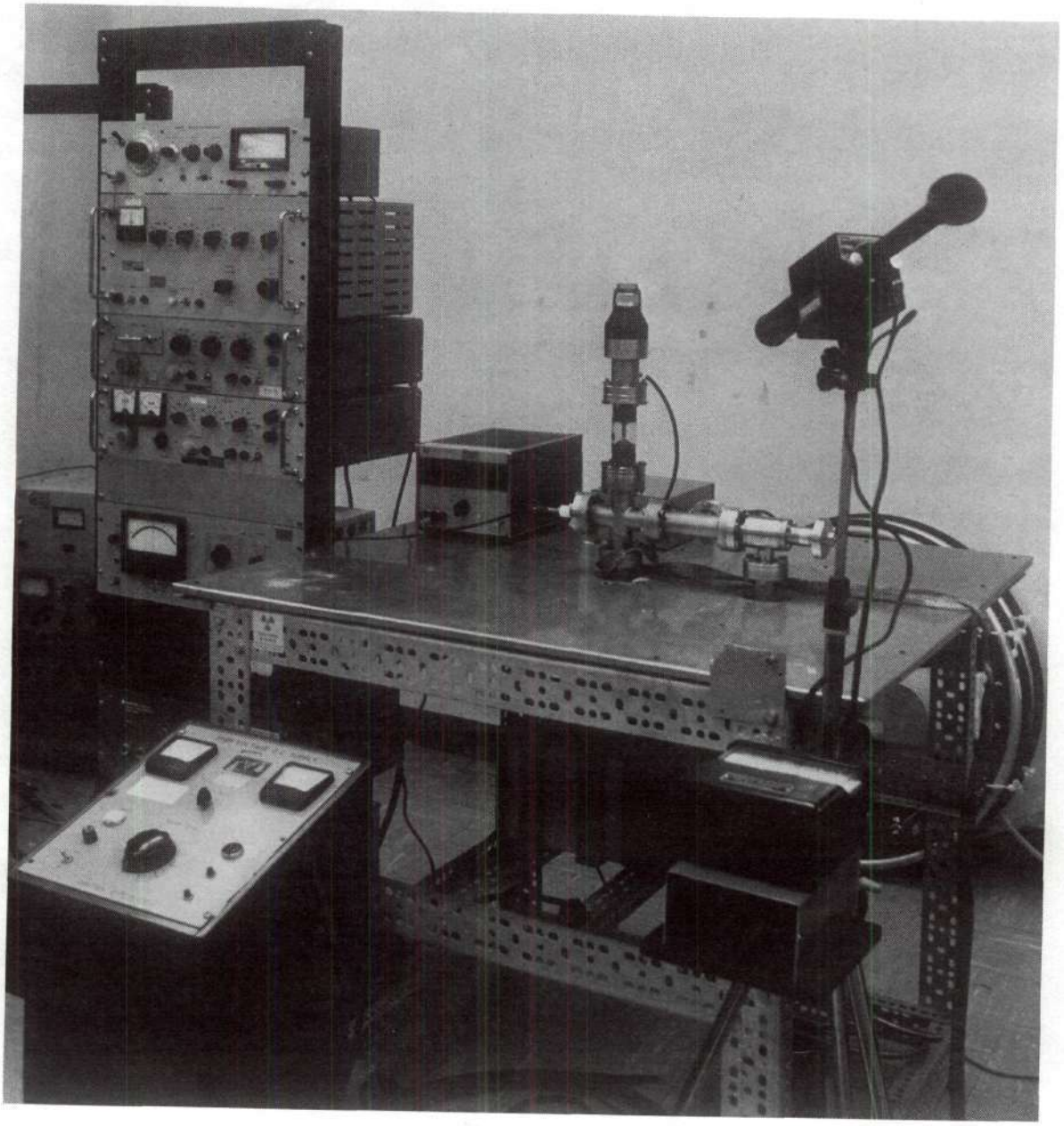

Figure 4. Overall View of the Ion-Pumped Vacuum System with the Small Variable-Spacing Diode in Place.

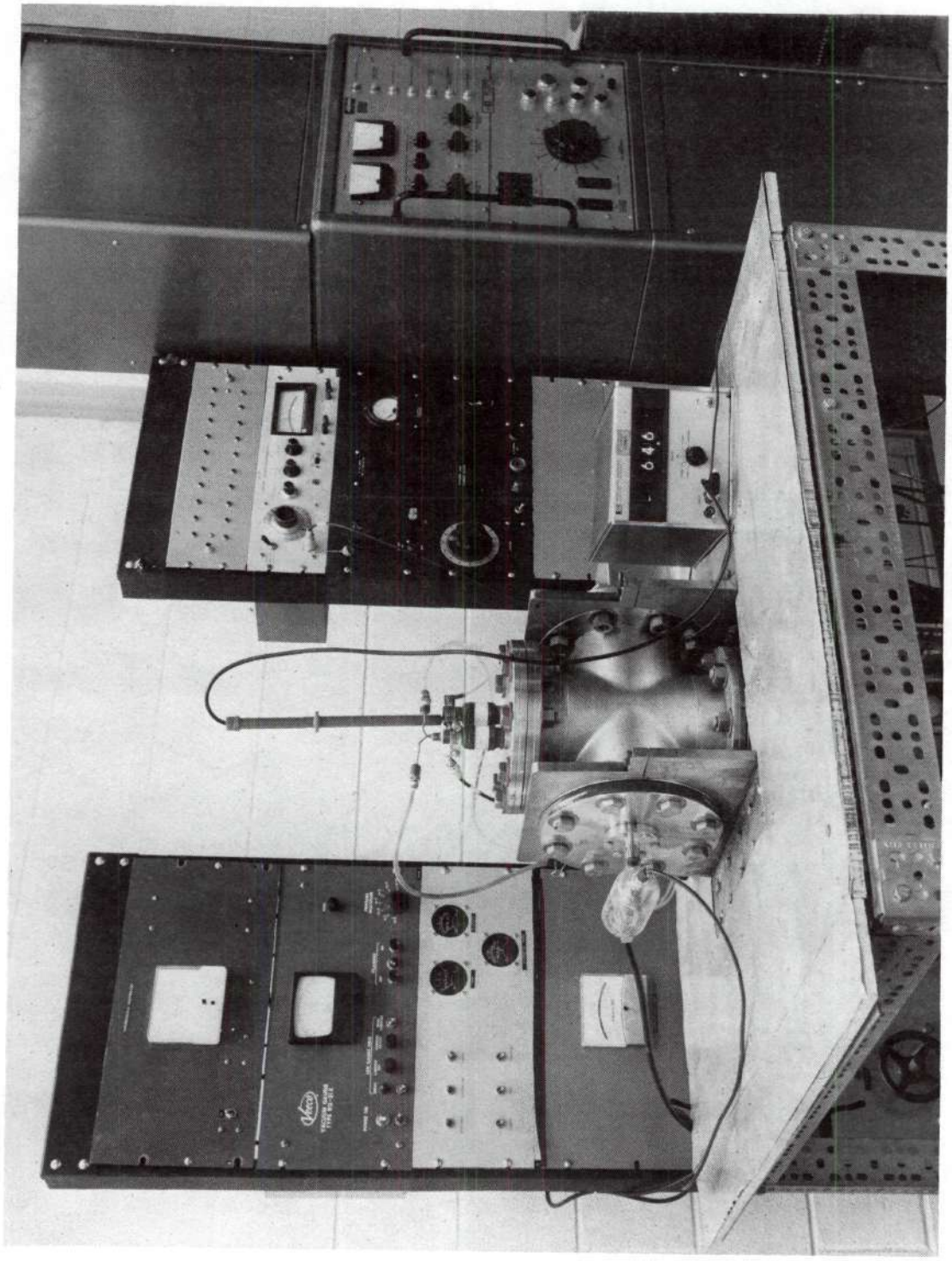

Figure 5. Overall View of the Diffusion-Pumped Vacuum System with the Water-Cooled Diode in Place.

ionization gauge) were routinely achieved.

Diodes

Two variable spacing diodes were used in conjunction with the ion-pumped vacuum system previously described. They were similar in construction and differed primarily in size.

For pulse testing purposes the larger of the two glass tubes previously described was used to contain the diode structure as shown in Figure 6. The cathode support structure was mounted to a stainless steel plate, intervening between the experiment tube and the cross, with porcelain insulators. This resulted in its electrical isolation from the vacuum chamber and prevented the inclusion of any leakage current in the measured emission current. Emission currents were measured via the insulated feedthrough mounted on the remaining branch of the cross. At the upper end of the tube a Varian linear motion feedthrough (Model 954-5049) was affixed. This supported the anode by means of a support rod, and allowed a 2.5 cm range of motion for the anode. Provision was made for easily changing the anode so that various sizes and types could be used. All anodes were constructed of molybdenum, and all other internal parts were of molybdenum or stainless steel. High voltage was applied by connection to the feedthrough mounting flange.

The smaller tube, as pictured in Figure 4, was identical in most respects to the larger one just described. The major difference was that the anodes were constructed of approximately

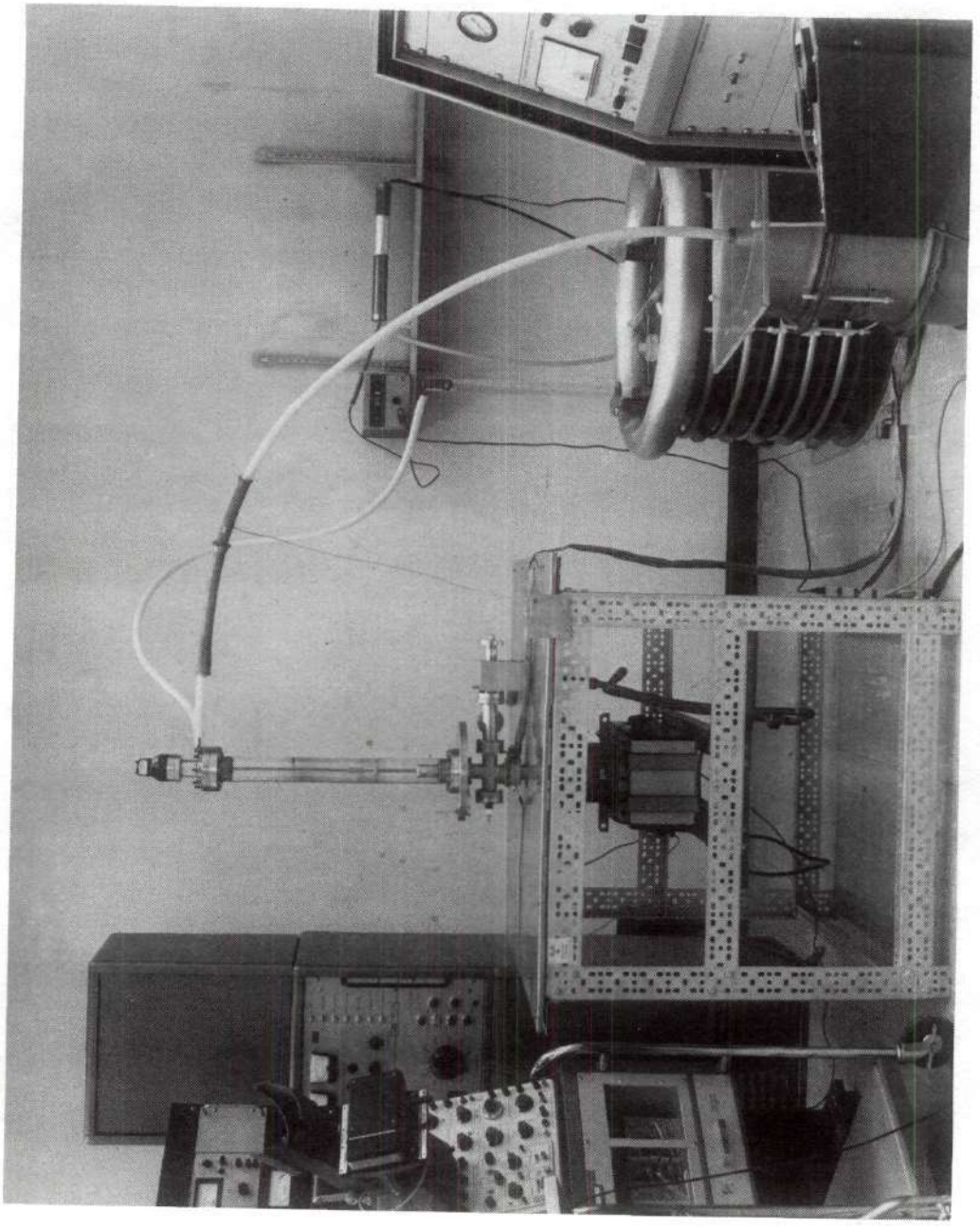

Figure 6. Overall View of the Experimental Equipment Used for Pulse Testing with the Large Variable-Spacing Diode in Place.

three inch lengths of 1/2 inch diameter molybdenum rod and were attached directly to the feedthrough dispensing with the support rod. This diode was used for study of the effects of interelectrode spacing.

The fixed-spacing diode used in the diffusion-pumped vacuum system is shown in Figure 7. Two high-current insulated feedthroughs were mounted in a nine inch ASA type flange and machined so that the anode and cathode mountings are parallel to within 0.001 inch. Water cooling was provided by drilling of the electrodes to a depth of six inches allowing the circulation of water in the anode support during operation. Thermal expansion of the anode proved to be negligible up to power levels of ten watts (usually about five mA emission current) making it possible to obtain voltage-current data up to this power level with minimal interelectrode spacing variation. This diode was used for the tests studying the effects of pin tip radius and pin packing density, and general tests to determine maximum macroscopic current densitites. Anodes for this diode were also constructed of molybdenum, and cathode supports were of molybdenum and stainless steel. Electrical connections for high voltage application and current measurement were made directly to the copper electrodes of the feedthroughs.

Electronics

Dc Tests. All of the electronics used for dc testing operations in all diodes are shown in Figures 4 and 5.

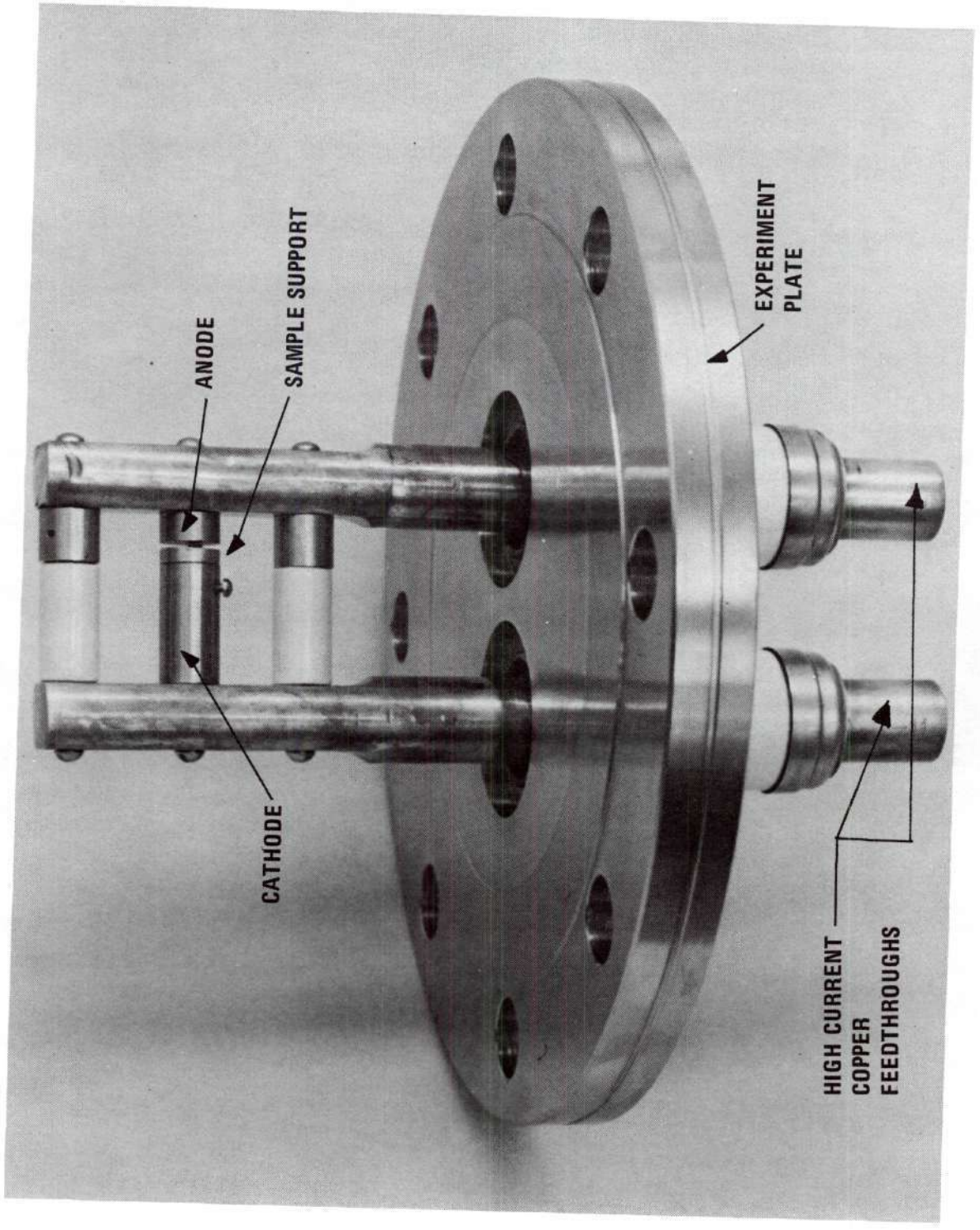

Figure 7. Photograph of the Water-Cooled Diode.

Depending upon the voltage and current requirements of a particular test one of the high voltage dc power supplies listed in Table 2 was used. Also noted are the voltage and current capabilities of each of these supplies. A Keithley 610 R or 610 CR electrometer was used for all emission current measurements. This allowed accurate current measurement ($\pm$ one percent) over the range from one nA to 100 mA.

Applied voltages were measured to $\pm$ ten volts by an Hewlet-Packard 3430A digital voltmeter in conjunction with either a 1000 MΩ Simpson high voltage probe or a 10000 MΩ Fluke high voltage probe.

Pulse Tests. An overall view of the pulse emission testing set-up is shown in Figure 6, and in Figure 8 a schematic of the circuitry is given.

The Marx Generator (Maxwell Model 50030) charging voltage and number of stages of the generator used could be adjusted to give a very wide range of output voltages. Measurement of the applied voltage was accomplished by use of a 2000:1 capacitive voltage divider whose output was displayed via a storage oscilloscope (Hewlett-Packard 141A) for reference purposes or photographed by an oscilloscope camera mounted on a Tektronix 545B oscilloscope for permanent recording. Current waveforms were permanently recorded by photographing the trace displayed on the Tektronix 545B oscilloscope.

A significant difficulty encountered in the pulsed emission current measurement was that introduced by the presence

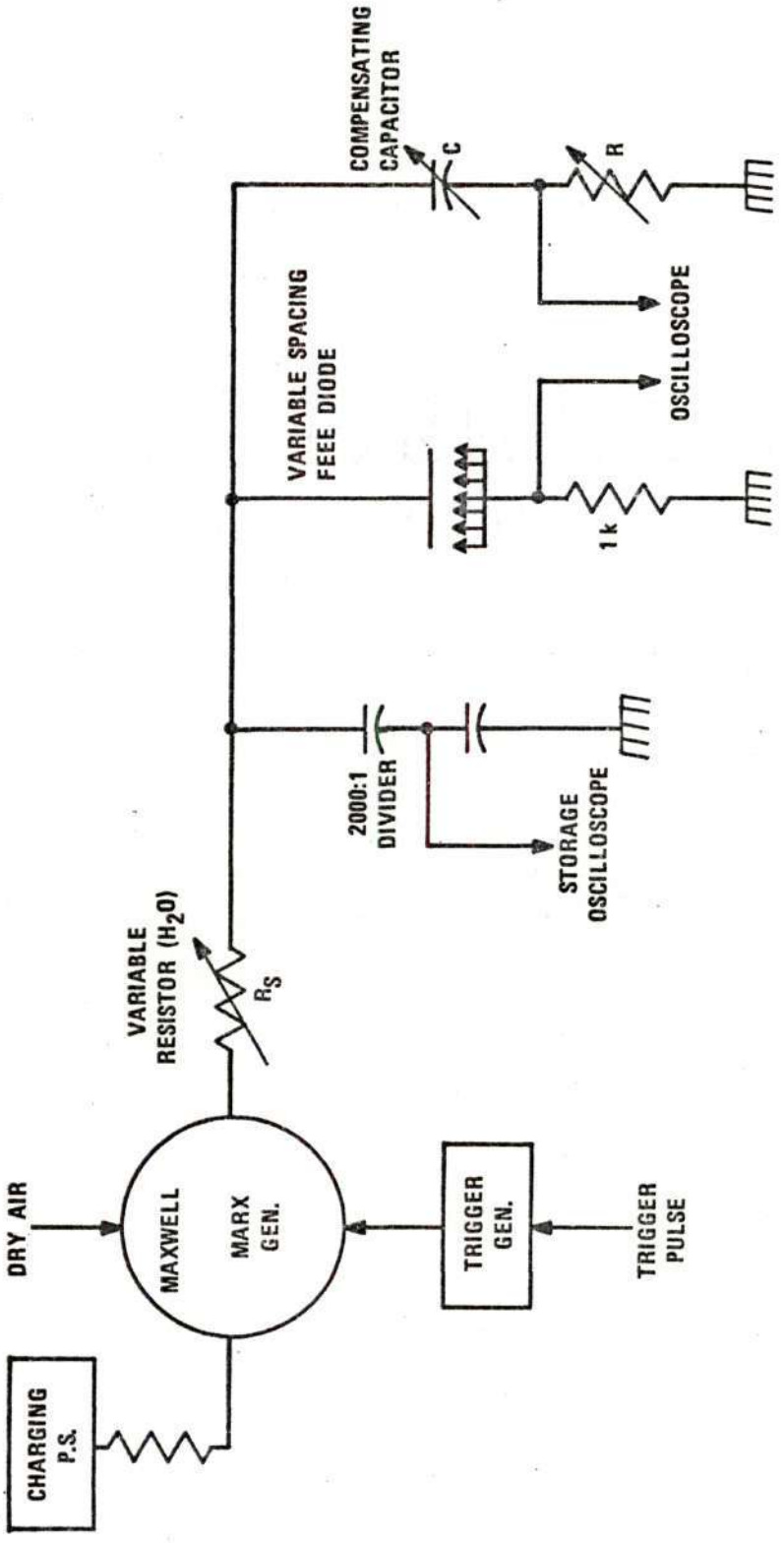

Figure 8. Schematic Diagram of the Experimental Apparatus used for Pulse Testing.

Table 2. High Voltage dc Power Supplies Used.

Manufacturer	Model No.	Max. Voltage (kV)	Max. Current (mA)
Fluke	412B	2.1	30
Fluke	413D	3.1	20
Fluke	410B	10	10
Sorensen	2012-250	12	250
Del Electronics	50TC-5-1	50	5

of capacitive transients, Figure 9. The anode-cathode capacitance of the test diode was measured to be approximately 13.6 pF. This capacitance was determined primarily by the long support rods and the cathode, and consequently was relatively insensitive to spacing. This value of capacitance was sufficient to support a transient current many times the expected emission currents. The transient current could be reduced by increasing the size of R_s; however, this also reduced the magnitude of the voltage pulse, as well as delaying the occurrence of the voltage maximum. In order to make valid pulsed measurements, it was necessary to use a nulling technique to remove the capacitive transient current. This was accomplished by using an adjustable coaxial capacitor to sample the voltage pulse. The compensating signal, taken from the junction of R and C (Figure 8), was applied to one channel of a differential amplifier oscilloscope. The values of R and C were then adjusted to cancel, as nearly as possible, the capacitive transient from the test diode. This adjustment was very critical because of the extremely high values of dV/dt at the high voltages. Since the anode-cathode capacitance was relatively independent of interelectrode spacing, minor changes in spacing could be made without readjusting the compensating capacitor.

Photos of various typical current wave forms are shown in Figure 9-13. Included are: the uncompensated capacitive diode current (no emission current), Figure 9; the compensating

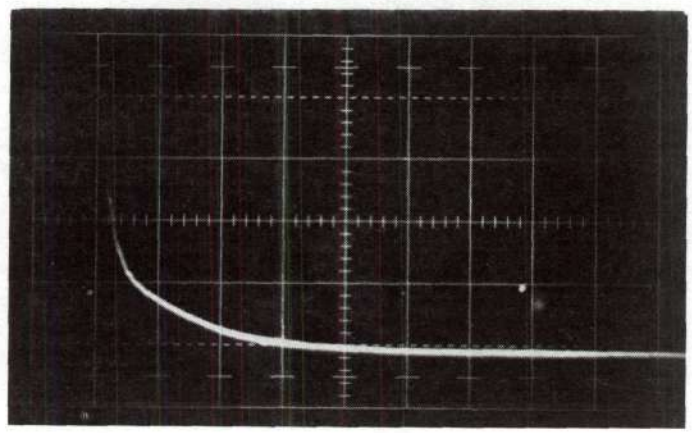

Figure 9. Typical Uncompensated Diode Current: Vertical 2mA/div; Horizontal, 10μsec/div. Origin is one div up and one div right.

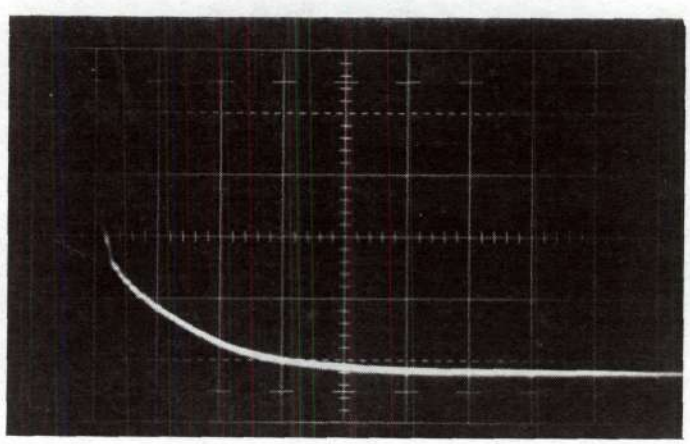

Figure 10. Typical Output from Compensating Capacitor. Vertical, 1mA/div; Horizontal, 10μsec/div. Origin is one div up and one div right.

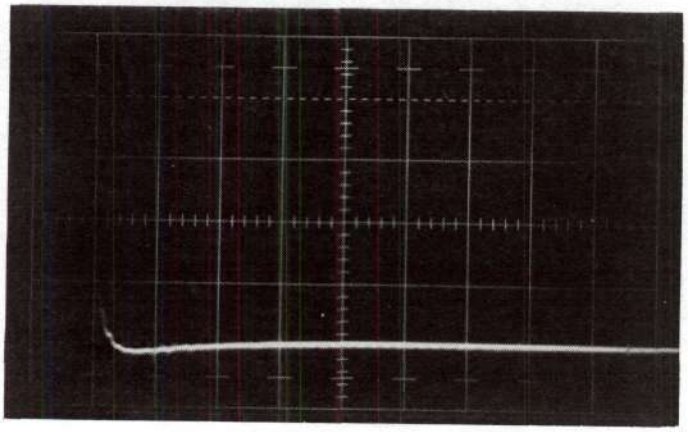

Figure 11. Typical Baseline Obtained by Subtraction of Signal Shown in Figure 10 from that Shown in Figure 9. Vertical, 2mA/div; Horizontal, 10μsec/div. Origin is one div up and one div right.

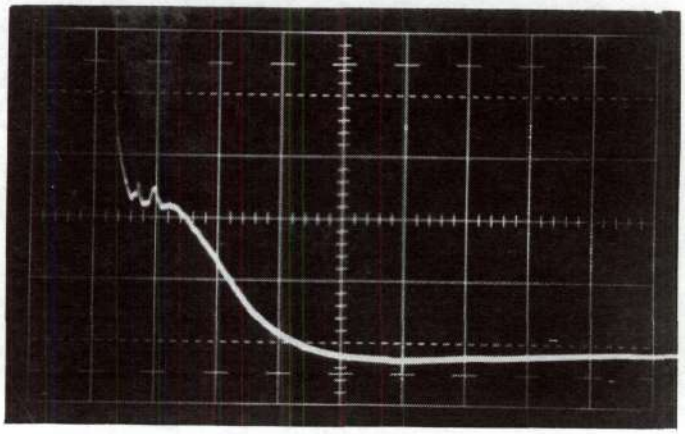

Figure 12. Typical Emission Current Waveform as Observed without Capacitive Current Compensation. Vertical, 1mA/div; Horizontal, 20μsec/div. Origin is one div up and one div right.

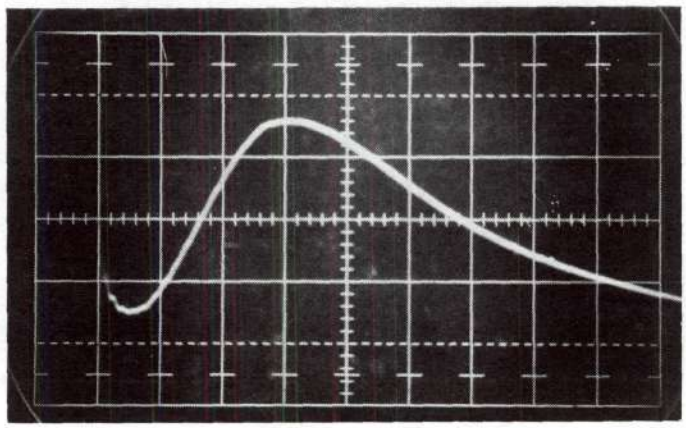

Figure 13. Typical Emission Current Waveform Using the Compensating Capacitor. Vertical, 2mA/div; Horizontal, 10μsec/div. Origin is one div up and one div right.

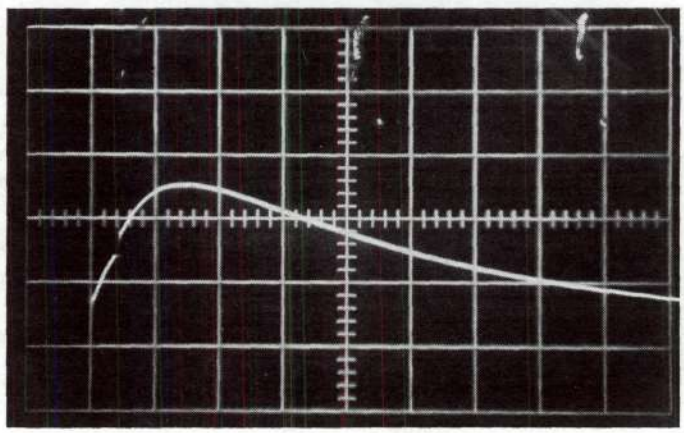

Figure 14. Typical Waveform of the Applied Voltage. Vertical, 10kV/div; Horizontal, 20μsec/div. Origin is one div up and one div right.

capacitor output current, Figure 10; the base line obtained by adding the waveform of Figure 9 and the inverted waveform of Figure 10, Figure 11; the emission current observed without capacitive current compensation, Figure 12; and a typical emission current trace as observed using the nulling capacitor, Figure 13. Figure 14 shows a typical voltage trace.

Emitter Installation and Pumpdown Procedures

The essential points of operation of the two vacuum systems were identical, involving rough pumping, pumpdown and bakeout, cooldown and base pressure attainment, and emitter activation. Details of operation differ considerably however, and each will be described separately.

As noted previously the cathode support structure was compatible with the stage of a scanning electron microscope. Samples for use in either system were routinely inspected prior to installation in the test diode. Assessments were made of array parameters such as pin height, pin diameter, pin tip radius, and pin packing density (if not determined optically as previously described).

Diffusion Pumped System-Water Cooled Diode

After obtaining the required scanning electron micrographs, the emitter sample and the anode were attached to their respective electrodes in the diode structure. The interelectrode spacing was set by viewing the structure in a binocular microscope (about 30X) and comparing the interelectrode space

with a piece of shim stock of known thickness. Spacings of 2.5×10^{-3} cm to 2.0×10^{-2} cm (0.001 inch to 0.008 inch) were used. All surfaces of the vacuum chamber and diode were then thoroughly cleaned with methanol, and the diode structure was secured in the vacuum chamber.

Once the chamber was sealed the system was evacuated by the mechanical pump to a pressure of less than ten mTorr, usually in less than five minutes. At this time the chamber heating tapes and the heating mantle on the zeolite trap were activated and brought up to temperatures of 150°C-180°C and about 375°C respectively. The pressure (monitored in the foreline by a thermocouple gauge) rose of a maximum to 500 mTorr after initiation of heating, and fell to less than 20 mTorr within two hours. At this point the diffusion pump was activated. Bakeout was continued for 24-48 hours, then terminated and the system allowed to cool. The base pressure of 5×10^{-9} to 3×10^{-8} torr was generally reached within 12 hours after termination of heating.

Ion Pumped System-Variable Spacing Diode

As noted previously scanning electron micrographs of the emitters were obtained prior to installation. Once the sample was installed and the vacuum system was sealed, the zeolite sorption pump was vented and baked for one to three hours by means of a heating mantle. Upon sealing and cooling to near room temperature the sorption pump was activated by immersion in liquid nitrogen, and within ten minutes a pressure of less

than 10 mTorr was achieved. At this time the ion pump heaters were used to bake the pump for a minimum of one hour. Upon completion of bakeout, the ion pump was allowed to cool, and was activated when the system pressure dropped to five mTorr or lower. The sorption pump was then isolated from the ultra-high vacuum by closure of the gold-seal valve, and bakeout of the glass and stainless steel parts of the system was initiated. Bakeout continued for 48-72 hours, and upon cooling and pumping another 12-24 hours a pressure of 1×10^{-10} to 5×10^{-9} torr was realized.

Once the base pressure was attained in either system the details of emitter activation were similar since samples intended for pulse operation were first operated in the dc mode for purposes of conditioning.

Emitter Activation

Emission testing was initiated by application of a voltage across the diode and a series resistor. Initially a series resistance of 1090 MΩ was normally used, and sufficient voltage was applied to the diode to produce an emission current of 0.01 to 1.0 μA. Since this initial emission was very erratic and sometimes resulted in vacuum arcs it was important to limit the total current available in the event of an arc by using the large value series resistance noted. Normally voltages applied to the diode of one to eight kV were sufficient to initiate emission, and power supply voltages of two to ten kV were required.

Within one to twelve hours the emission-current stability usually improved to ± five percent, and the total current often increased to as much as ten μA at similar diode voltages. Once this condition was achieved periodic increases in emission current of ten to 50% could be made with little danger of initiation of arcing. Decreasing values of series resistance were utilized as the total current was increased to avoid too large a voltage requirement from the power supply or alternatively the current limiting responsibility was turned over to a temperature limited diode (TLD). This device replaced the series resistance and by means of an 833A diode provided current control to approximately ± ten percent of the set value even in the event of shorting.

When the emitter had achieved stable operation the emission current was normally increased at a rate of ten to 100% every 24 hours. The level to which it was ultimately raised depended upon the objectives of a particular experiment. In the course of all tests, however, voltage-current (V-I) measurements were an integral part of monitoring the performance. Use of this information to produce a Fowler-Nordheim plot and interpretation of changes in the plot characteristics allowed assessment of the emitter performance. Consequently before detailing the procedures used for data acquisition in each individual type of test the method of taking V-I data will be described.

V-I Data Collection

Except in instances where the emitter was known to be operating at a power level sufficient to promote anode heating and consequently a decrease of the interelectrode spacing, the steady-state voltage and current were taken as the first data point. The voltage applied to the diode was then decreased in steps sufficient in size to reduce the emission current by 50 to 75%. Thus two data points were normally obtained in each current decade. V-I points were usually taken over a minimum of three orders of magnitude change in emission current, and currents were measured down to the 10^{-8} A decade if necessary.

When a set of data was completed using the decreasing voltage technique described, another set of data was often taken in a similar fashion by increasing the voltage step-wise to the original value. Alternatively the voltage was increased in a single step to its original value. Either technique provided a means of checking the reproducibility of the data set.

This general description of the data collection procedure applies to all tests performed, but individual experiments varied in detail. These points will be covered in the following sections, along with specific comments on vacuum systems and electronics used in each case.

Interelectrode Spacing Test

For the interelectrode spacing test the ion-pumped vacuum system with the small enclosure tube (Figure 4) was used. Voltage and current measurement methods were as described

previously, and the Del Electronics 50kV power supply was used with a series resistance of 27 MΩ. Before taking the V-I data for this experiment the sample was operated for a total of 620 hours at emission currents up to 2.75×10^{-4} A. Data sets were taken over a range of emission currents from 3.0×10^{-4} to 0.3×10^{-8} A.

Multiple V-I data sets were taken at spacings of 5.1×10^{-3}, 1.3×10^{-2} and 2.5×10^{-2} cm in order to ascertain the degree of reproducibility of the slope values of the Fowler-Nordheim plots. At all but the minimum spacing reproducibility was within $\pm$ five percent. At a spacing of 5.1×10^{-3} cm (0.002 inches) a significant error was introduced by the lack of ability to establish the spacing with better than 0.0002 inches reproducibility. Thus an error of up to $\pm$ ten percent could be incurred. A variation of $\pm$13 percent was obtained in the slope values at this spacing, a large part of which was due to the problem of establishing the spacing with adequate precision.

At each of the other four spacings a single data set was taken and checked as described previously. Reproducibility of individual data points was $\pm$ five percent.

Typical sets of data are given for reference in Appendix B. The reduction of data to yield the required slope values of the resultant Fowler-Nordheim plots will be described in a later section.

Pin Tip Radius Tests

In this set of experiments the diffusion-pumped vacuum system with the water-cooled diode (Figure 5) was used for each of the runs performed. The interelectrode spacing was set at 1.3×10^{-5} cm (0.005 inches) in all cases, and the same sample was used to maintain constant pin packing density. The pin tip radius was varied over a range estimated to be 400 Å to 2000 Å.

Each sample was operated for a period of 48 to 144 hours at emission currents up to 2.1×10^{-4} A before the required data were taken. The Sorenson 12 kV power supply was used with a series resistance of either 27 MΩ or 13.5 MΩ. Data sets were taken over a range of emission currents from 2.1×10^{-4} to 1.5×10^{-6} A. Reproducibility of individual data points was $\pm$ five percent. V-I data sets are given for reference in Appendix C.

Pin Packing Density Tests

Two samples with densities of 7.5×10^{6} and 16.6×10^{6} pins/cm^2 were used in this test. They were operated in the water-cooled diode mounted in the diffusion-pumped vacuum system. As nearly identical as possible tip radii were used, estimated to be about 2000 Å. An interelectrode spacing of 2.4×10^{-3} cm (0.001 inches) was used.

Sample D-1 (7.5×10^{6} pins/cm^2) was operated for 120 hours at up to 1.4×10^{-3} A emission current before the V-I data were taken. A current range of 1.4×10^{-3} to 7.9×10^{-7} A

was utilized in taking the data. The second sample, D-2 (16.6 x 10^6 pins/cm^2), ran at up to 1.25 x 10^{-3} A emission current for 280 hours prior to data acquisition, and a range of current from 1.25 x 10^{-3} to 1.75 x 10^{-6} A was used for the Fowler-Nordheim plot.

The Sorenson 12 kV power supply was used in conjunction with the TLD in both of these experiments. Voltage and current measurement were identical to those specified previously. Typical V-I data from this test are given in Appendix D.

This completes the specific descriptions of experimental procedures. A large number of additional samples were run (about 30) in experiments designed to determine the upper limit of the macroscopic current density (current per unit array area) available from the composite emitter arrays. A brief description of the features of these experiments follows.

Gross Emission Tests

The overall objective of these experiments was to ascertain the maximum macroscopic current density which the emitter arrays were capable of producing, and to determine what factors were responsible for limiting their performance. Both dc and pulsed operation were utilized over a broad range of interelectrode spacings and applied voltages. All of the previously described vacuum systems, diodes, and electronics were used. Monitoring of performance was accomplished by simple measurement of the total emission current, as well as by

periodic collection of V-I data. An attempt was made to apply assessment of changes in Fowler-Nordheim characteristics as a diagnostic tool.

Emission samples were inspected by optical and scanning electron microscopy prior to testing, and were subsequently installed in the test diodes as described previously. Vacuum system operation and emitter activation were identical in all respects to the earlier descriptions. Once the sample achieved stable emission the voltage was gradually increased such that the emission current increased by ten to 100% every 24 hours. The larger percentage increases were usually used at low gross currents, i.e., less than 100 μA. When the current was one mA or greater changes of ten to 25% were routine.

V-I data were normally taken once in each 24 hour period, but were occasionally taken twice in this time period. Data were taken in the fashion previously described except in instances where the power input to the anode was sufficient to promote anode heating and a consequent change in the inter-electrode spacing. In this case the emitter was shut down for a period of ten to 20 minutes to allow the anode to cool. The V-I data were obtained by step-wise increases in the applied voltage until it became apparent that heating was promoting a change in the spacing. This was evidenced by a decreasing voltage requirement to maintain a constant emission current, and usually became important at power levels above about ten watts.

The foregoing comments apply to all samples run in the dc mode and to the conditioning operation for all samples which were also tested in the pulsed mode. The conditioning operation normally entailed dc operation at gross emission currents up to one to ten mA, under which conditions significant anode heating occurred. This promoted desirable outgassing of the rather massive anodes usually involved, and conditioning was regarded as complete when thorough outgassing was indicated by system pressure stability.

Pulse testing was normally initiated after the anode and anode support had cooled to room temperature and the interelectrode spacing was stable. For initial operation the spacing was generally in the range of 0.3 to 0.7 cm and applied potentials of to 20 to 40 kV were commonly used.

Before the initial emission currents, usually 200 to 500 μA, could be unambiguously observed, it was necessary to adjust the nulling circuit. This was accomplished by operating the diode at a voltage below the threshold for sensible emission and changing the values of C and R (see Figure 8) to produce a flat baseline trace on the oscilloscope. Alternatively, since the interelectrode capacitance varied slowly with spacing, the spacing was increased sufficiently to preclude emission and the nulling time constant adjusted. This adjustment was very critical at the higher voltages.

Once a measureable pulse emission current was observed by increasing the voltage or decreasing the spacing gradually,

an effort was made to determine the maximum current obtainable without breakdown. When it was felt that the maximum performance of a particular sample had been realized or the sample performance degraded due to breakdown damage, the sample was removed and inspected once again with the optical microscope and/or scanning electron microscope.

V-I data were obtained from the pulse emission tests by measurement of emission current and applied voltage from the decaying portions of simultaneously obtained oscillographs of the voltage and current traces. The decreasing voltage portion of the V and I traces was utilized for this purpose since the capacitive current nulling was virtually perfect over this time period. Especially at high applied voltages (80-110 kV) the extremely large values of dV/dt experienced during the voltage rise made perfect nulling impossible.

Typical current and voltage oscillographs were given in Figures 13 and 14, and several representative sets of V-I data are given in Appendix F.

All quantitative assessments of emitter characteristics were dependent upon determination of the slope of the Fowler-Nordheim plot. Thus from the V-I data, collected as described here, a Fowler-Nordheim plot was constructed and the slope determined. Procedures for this are described in the final section of this chapter.

V-I Data Reduction

From the raw V-I data the values of the parameters required for plotting the Fowler-Nordheim curve were calculated. These were typically values of $10^4/V$ and I/V^2, where V is the voltage applied to the diode and I is the corresponding value of the emission current. Occasionally for samples operating at exceptionally low or high applied voltages values of $10^3/V$ or $10^5/V$, respectively, were used. The values of $10^4/V$ and I/V^2 thus calculated were then used to plot the Fowler-Nordheim curve on semi-logrithimic paper with $10^4/V$ on the abscissa and I/V^2 on the ordinate. A typical plot of this type was shown in Figure 1. Before calculation of the value of the slope the plot was inspected for data points deviating widely from an approximately linear relationship or which did not fit a smooth curve. These were normally only found at or near the maximum or minimum measured currents. Deviation at large currents was usually due to interelectrode spacing variation due to anode heating, and low current points were generally deviate due to externally induced noise. When these types of errors were observed and accounted for the questionable data points were disregarded in the slope calculations. All other points were considered and another criterion applied as to the acceptability of the calculated value of the slope.

The method of least-squares linear regression was used to fit the data to the following generalized expression of equation (16),

$$\log (I/V^2) = A + B/V. \tag{32}$$

The slope, m, of the fitted line was then taken as the slope of the Fowler-Nordheim curve, and utilized in all calculations involving the expression for the slope as given by equation (20).

To determine the accuracy of the fit of the derived relationship the correlation coefficient was calculated according to the following expressing,

$$n = \frac{m\sigma_x}{\sigma_y} \tag{33}$$

where m is as defined above and σ_x and σ_y are the square roots of the variances of the values of 1/V and log (I/V^2), respectively. The general expression for the variance is as follows,

$$\sigma_x^2 = \frac{\sum_{i=1}^{N} x_i^2}{N} - x^{-2}. \tag{34}$$

For the specific tests in which the slope, m, of the Fowler-Nordheim curve was used as a parameter for the calculation of field enhancement factor, no data were considered valid if the value of the correlation coefficient was lower than 0.985. For all but one calculation the value of n was in the range 0.991 to 0.999.

All raw V-I data and results of the above described calculations are given in Appendices B, C and D for the test

involving the relationships between interelectrode spacing, pin tip radius, and pin packing density and the field enhancement factor, β.

This chapter has presented all procedural details related to the gathering of data and sample preparation. In the following chapter the experimental findings are presented and discussed in view of available theories where possible.

CHAPTER III

RESULTS AND DISCUSSION

The results of this investigation have been divided into three sections. In the first section the effects of anode and cathode geometry on emitter performance are reported. This discussion will be somewhat qualitative in nature, since the bulk of the information presented does not lend itself to concise theoretical description. The second part is considerably more quantitative and presents results describing the effects on the field enhancement factor caused by variation of diode and array parameters (interelectrode spacing, pin tip radius, and pin packing density). The final section deals with the limitations on the field emission performance of the arrays used in this study, and describes the problem areas which prevent realization of the tremendous current densities promised theoretically.

Effects of Anode-Cathode Geometry

As has been pointed out in the previous sections, establishment of an electric field of 10^7 to 10^8 V/cm is a necessity for field emission from a material such as W. In order to attain fields of this strength at reasonable voltages sharply pointed tips are utilized, resulting in enhancement of the macroscopic applied field at the individual tips. The

process of field emission is extremely sensitive to the value of the field at the emitter surface. In order to obtain uniform emission from each tip in an array, it is mandatory that every pin of an array have the same field enhancement factor and the same value of macroscopic applied field. Early in the experimental work of this study it became apparent that the latter of the two conditions stated was not being fulfilled as a result of the diode geometry being used. An important part of the research became a study of the macroscopic field effects caused by diode design. Initially a large area planar anode was used in conjunction with a cathode of considerably smaller size (see Figure 15(a)). In this diode the emission current was non-uniformly distributed across the array surface, and post-emission observation of emission samples consistently showed that most emission damaged pins were located within five to ten pen separation distances (one pin separation distance is approximately 3.5 μm at a packing density of 10^7 pin/cm^2) from the sample edge. The evidence for the non-uniformity of the emission is also based on visual observation of several diodes during operation at voltages in excess of 10 kV and emission currents of more than one mA.
Under these conditions in a darkened room the blue glow associated with high energy electron impact on metals was clearly seen to be restricted to a circular ring on the anode corresponding approximately to the circumference of the cathode. This result is contrasted with an earlier report on the emission

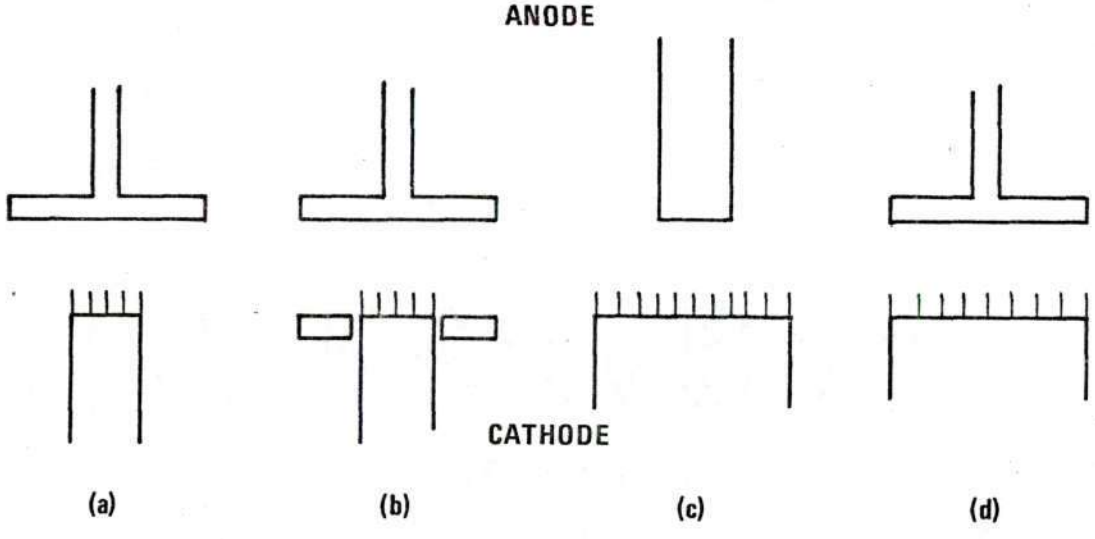

Figure 15. Schematic Diagrams of the Diode Geometries Studied by the Resistance Paper Analog Method.

current distribution given by Chapman, et al.[59], for a similar diode geometry, but using a segmented anode in an attempt to determine the spatial distribtuion of the current.

As a result of these observations, three alternative diode designs were contemplated as shown in Figures 15(b), (c), and (d). Rather than constructing each of these and attempting to design an experimental setup in which the actual current distribtuion could be measured, it was decided that simple two dimensional cases could be studied using a resistance paper analog. The cathode arrays were drawn to an approximate scale of 10^4:1. A typical array is shown in Figure 16. The cathode pattern and an anode of suitable size for the desired goemetry were painted with a conducting silver paint. For the case of the cathode with guard ring, the ring was also added, making electrical contact with the cathode array. A regulated power supply was used to establish a potential of five volts between the anode and cathode, and a digital voltmeter was used to plot the equipotential lines at 0.2 volt intervals in the interelectrode space. An arbitrary distance unit was selected and the potential differential across this distance was determined in order to obtain a relative field measurement. The results of these measurements are shown in Figures 17, 18, 19, and 20. In the figures, the potential variation above a center pin and an edge pin along the axis of the particular pin is shown. The slope of the curves is a measure of the electric field above each pin along

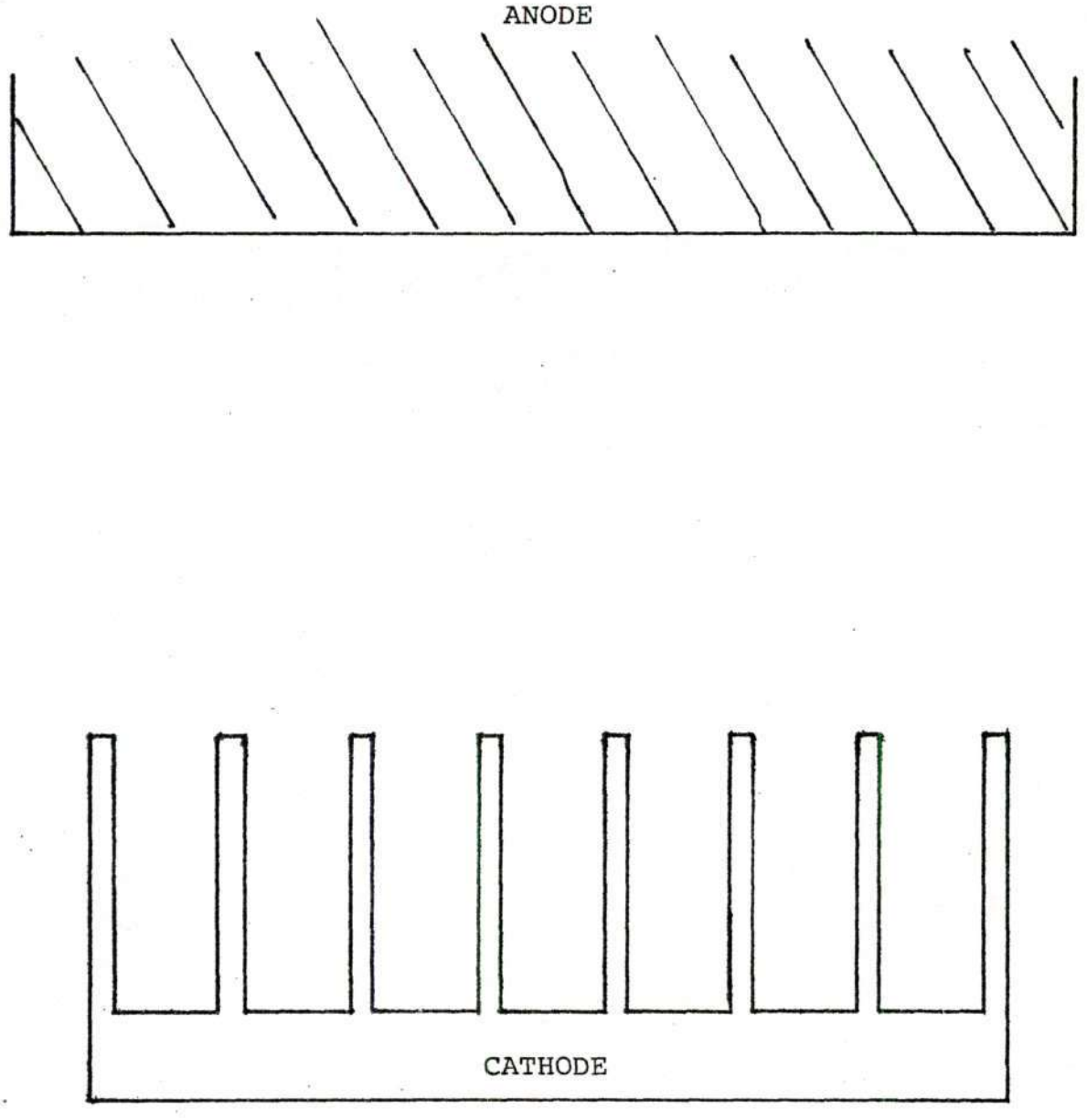

Figure 16. Drawing of Typical Array Studied with Resistance Paper Analog Method. (one-half size)

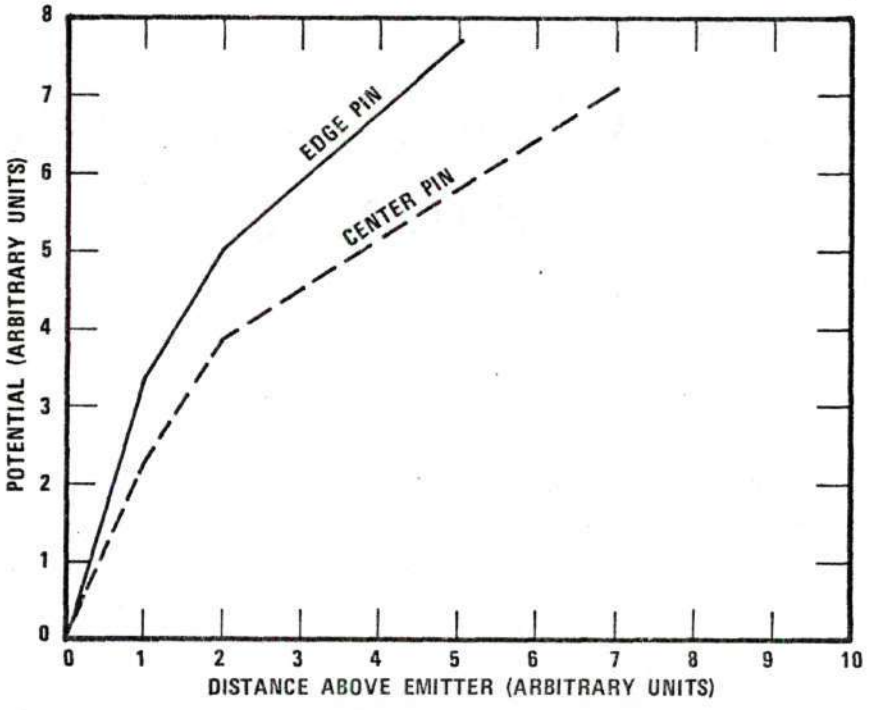

Figure 17. Potential Variation Above Edge Pin and Center Pin for Small Cathode-Large Anode. See Figure 15(a).

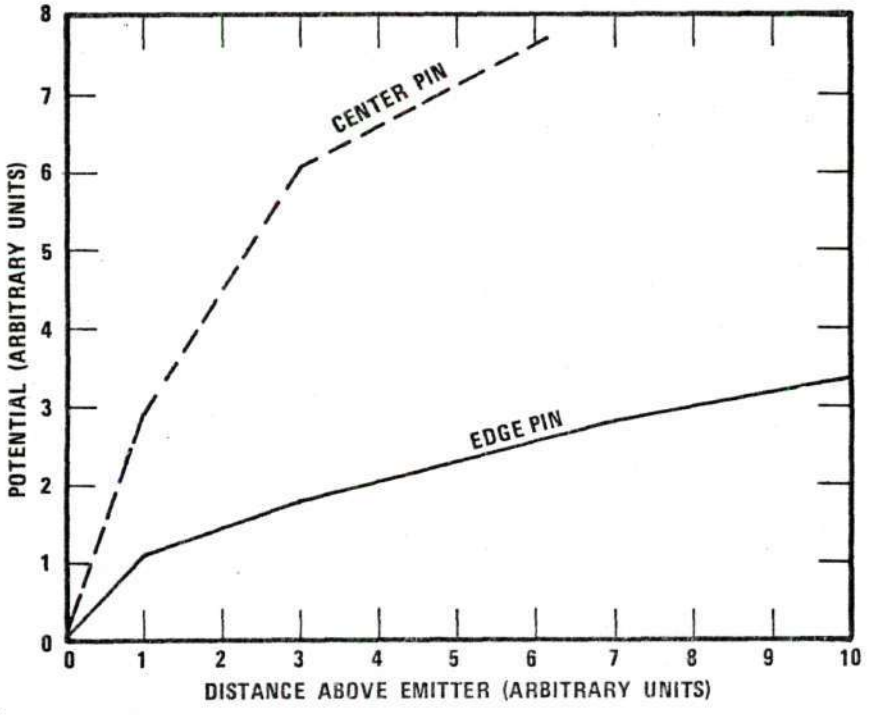

Figure 18. Potential Variation Above Edge Pin and Center Pin for Large Cathode-Small Anode. See Figure 15(c).

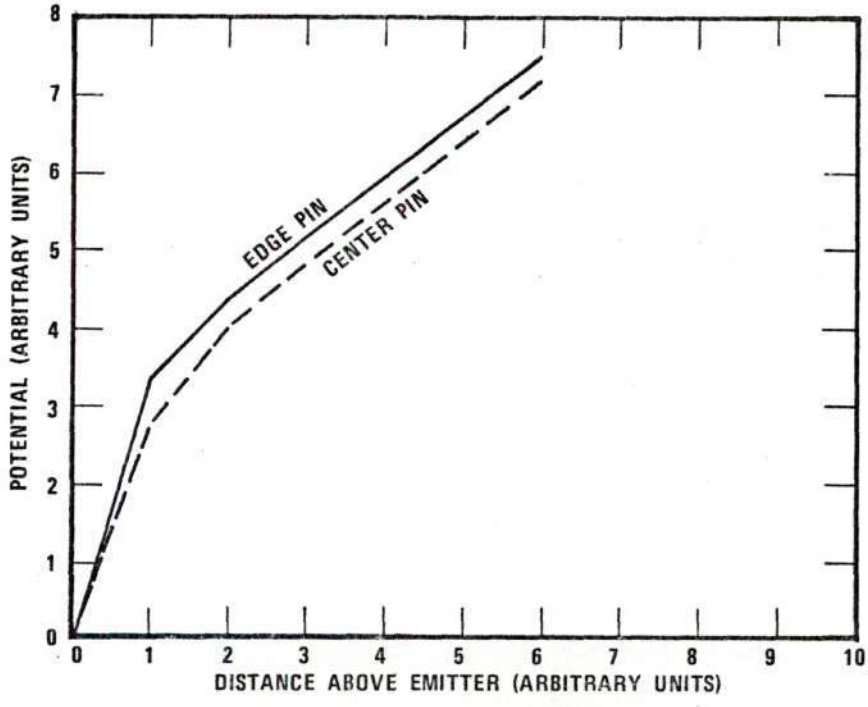

Figure 19. Potential Variation Above Edge Pin and Center Pin for Same size Anode and Cathode. See Figure 15(d).

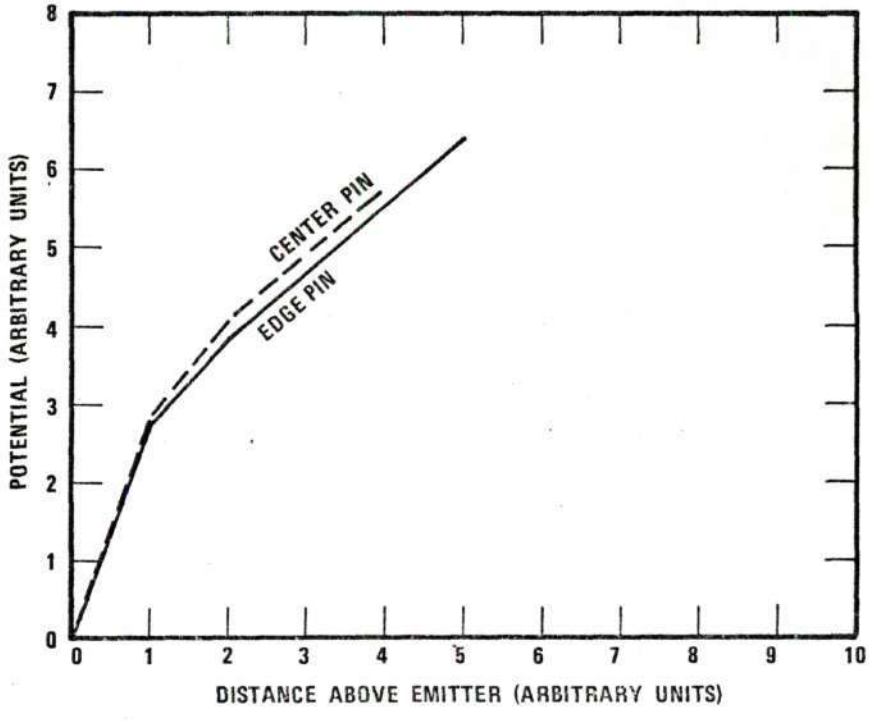

Figure 20. Potential Variation Above Edge Pin and Center Pin for Guarded Cathode. See Figure 15(b).

the pin axis. The field values near the edge and center pin tips of a given geometry provide a comparison of the degree of the edge effects for that case. In Table 3, the field strengths in arbitrary units of potential per unit distance are compared for edge and center pins in each of the four geometries shown in Figure 15.

It is quite apparent that the field enhancement is much higher at an edge pin than at a center pin for the large anode-small cathode geometry of Figure 15(a). A relative field strength value approximately 1.5 times as large is determined for the edge pin, and from the Fowler-Nordheim equation it can be calculated that a field increase of this magnitude is sufficient to produce a greater than one hundred fold increase in current density.

The opposite situation is observed in Figure 18 for the case of the small anode-large cathode geometry as shown in Figure 15(c). A center pin in this design experiences a field nearly three times as large as that which exists at an edge pin. This would be just as undesirable as the opposite condition if only pins near the center of the array experienced the high field. However further work with this geometry demonstrated that the field is quite uniform over the majority of the area under the anode, decreasing sharply in value only near the anode edge. A computer simulation of this geometry using a flat anode and cathode, i.e., no pins on the cathode surface, showed that the macroscopic field at the cathode

Table 3. Field Values from Resistance Paper Analog.

Anode-Cathode Geometry	Field Strength (Arbitrary Units)	
	Edge Pin	Center Pin
Large Anode-Small Cathode	3.4	2.3
Small Anode-Large Cathode	1.1	2.9
Anode-Cathode, Equal Diameter	3.3	2.7
Large Anode-Small Cathode w/Guard Ring	2.7	2.8

surface was constant within 1% over approximately 95% of the anode diameter. The field then dropped off rapidly in strength moving radially outward from beneath the circular anode. Thus the small anode-large cathode geometry appeared to be extremely attractive.

From Figure 19 it is apparent that the geometry using equal diameters for the anode and cathode (see Figure 15 (d)) would be better than the first case considered. However, Table 3 shows that the differential in current density between edge and center pins is still considerable, and an additional problem of critical alignment of anode and cathode was foreseen. Thus this design was not considered satisfactory for experimental use.

The curves for the guarded cathode with large anode (Figure 15 (b)) as shown in Figure 20 appear to be nearly ideal. The field strength at the surface of the two pins considered is essentially identical. Based on these results this design was considered to be the most desirable of the four described here. In actual usage however, it became evident that the vertical location of the emitter surface relative to the guard structure was extremely critical; probably requiring reliable mounting of the sample to within $\pm$ five μm to assure that the tips of the typically 10 μm tall pins were very nearly in or protruding only very slightly above the plane of the upper surface of the guard structure. Location of the cathode within the guard ring constrained by these accuracy requirements posed a difficult problem.

Furthermore, an analysis of a substantially different problem shed further light on the situation. The analysis of the packing effect by Levine[35] mentioned previously can be extended to predict the macroscopic current density (emission current per unit area of array), J_m, as a function of the diode array parameters. In this approximation the array was considered to be two dimensional with emitter pins spaced on a grid of dimension a and each having a hemispherical tip of radius r. The other parameters considered were the interelectrode spacing d and the applied voltage V. The Fowler-Nordheim equation as written in equation (10) expresses the microscopic current density, J. Assuming an emitting area per pin of πr^2 and noting that the pin density for a square array as considered here is a^{-2}, the following expression is obtained for macroscopic current density, J_m,

$$J_m = \left(\frac{\pi r^2}{a^2}\right) \frac{1.54 \times 10^{-6} \beta^2 V^2}{\phi} \exp\left[\frac{-6.83 \times 10^7 \phi^{3/2}}{\beta V}\right] . \qquad (35)$$

Note that for this simple approximation the image correction functions f(y) and t(y) have been assumed to each equal one and $\phi = 4.5$ as for clean W. Utilizing Levine's approximation for β allows rewriting this equation into the following form and allows calculation of J_m for any set of the variables r, d, a, and V as described above,

$$J_m = 3.42\times10^{-7}\left[\frac{V}{r\left(1+\frac{4\pi dr}{a^2}\right)}\right]^2\left\{10^{\frac{-2.84\times10^{8}\left[r\left(1+\frac{4\pi dr}{a^2}\right)\right]}{V}}\right\}\left(\frac{\pi r^2}{a^2}\right). \quad (36)$$

This expression has been used to calculate values of J_m as a function of the pin packing density, ρ. Three cases were considered for interelectrode spacings, d, of 1×10^{-1}, 1×10^{-2} and 1×10^{-3} cm. At these spacings voltages of 2×10^{3}, 2×10^{2} and 20 V were used, respectively, giving a constant macroscopic field, $F = v/d$. A pin tip radius of 0.1 μm (1×10^{-5} cm) was used for all cases. The data are plotted as the logarithm (base 10) of the ratio of J_m for a given packing density (ρ) to the maximum J_m for the particular spacing at the optimum ρ (Figure 21).

The overall shape of all curves in Figure 21 is similar. The important feature of the behavior of J_m is the tremendous loss incurred when a packing density of about 3×10^{5} pins per cm^2 is exceeded. The same data plotted on a finer scale in Figure 22 demonstrates another important point. As the spacing is increased, the packing density for optimum J_m decreases noticeably. This behavior is even more pronounced for spacings of one cm and larger. This effect is obviously of great significance when considering the theoretically desireable values of ρ which would maximize J_m, and furthermore sheds some light on the problem of interest in this discussion.

Since all emitter samples tested were of 5×10^{6} pins/cm^2

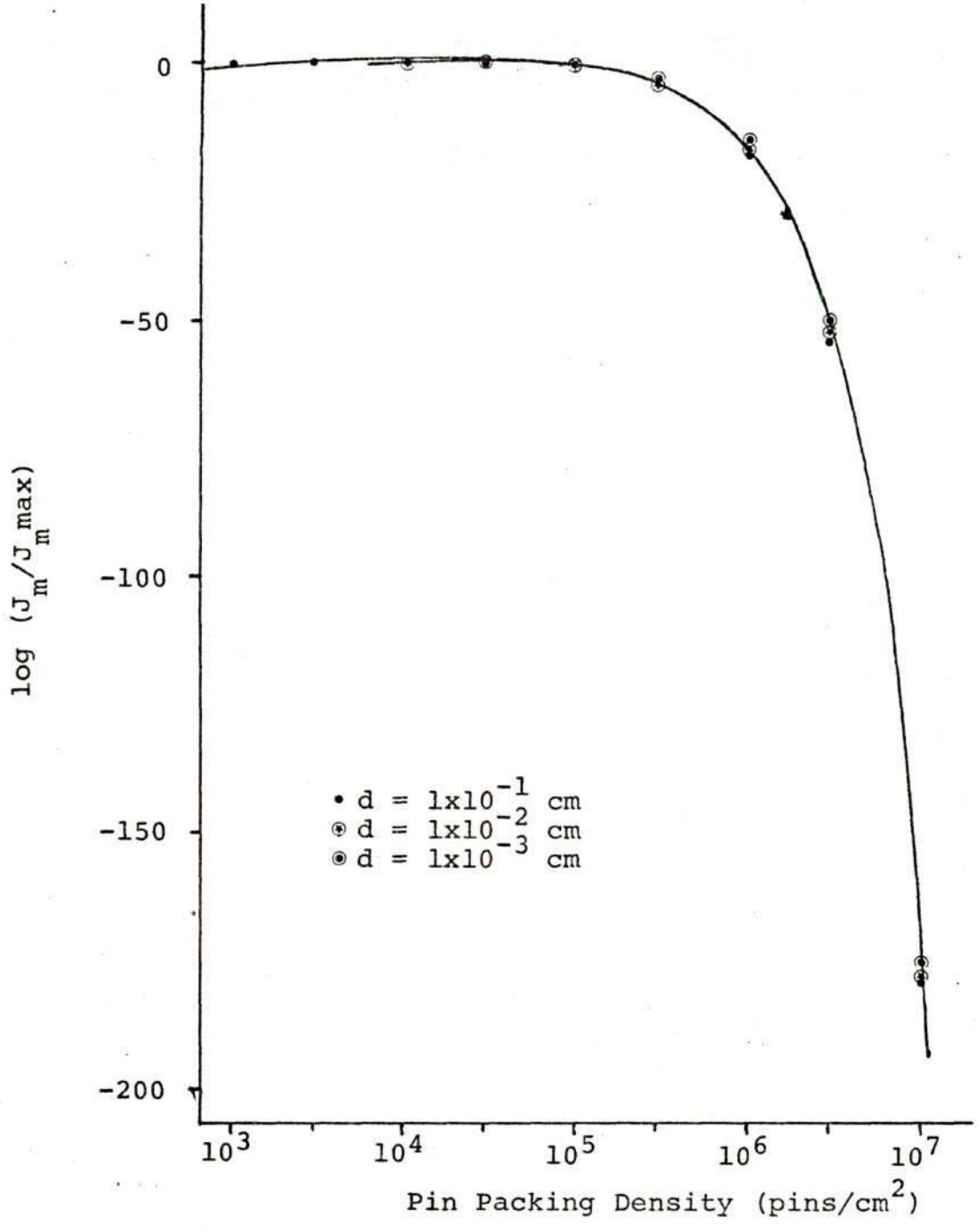

Figure 21. Logarithm of the Normalized Macroscopic Current Density as a Function of Pin Packing Density.

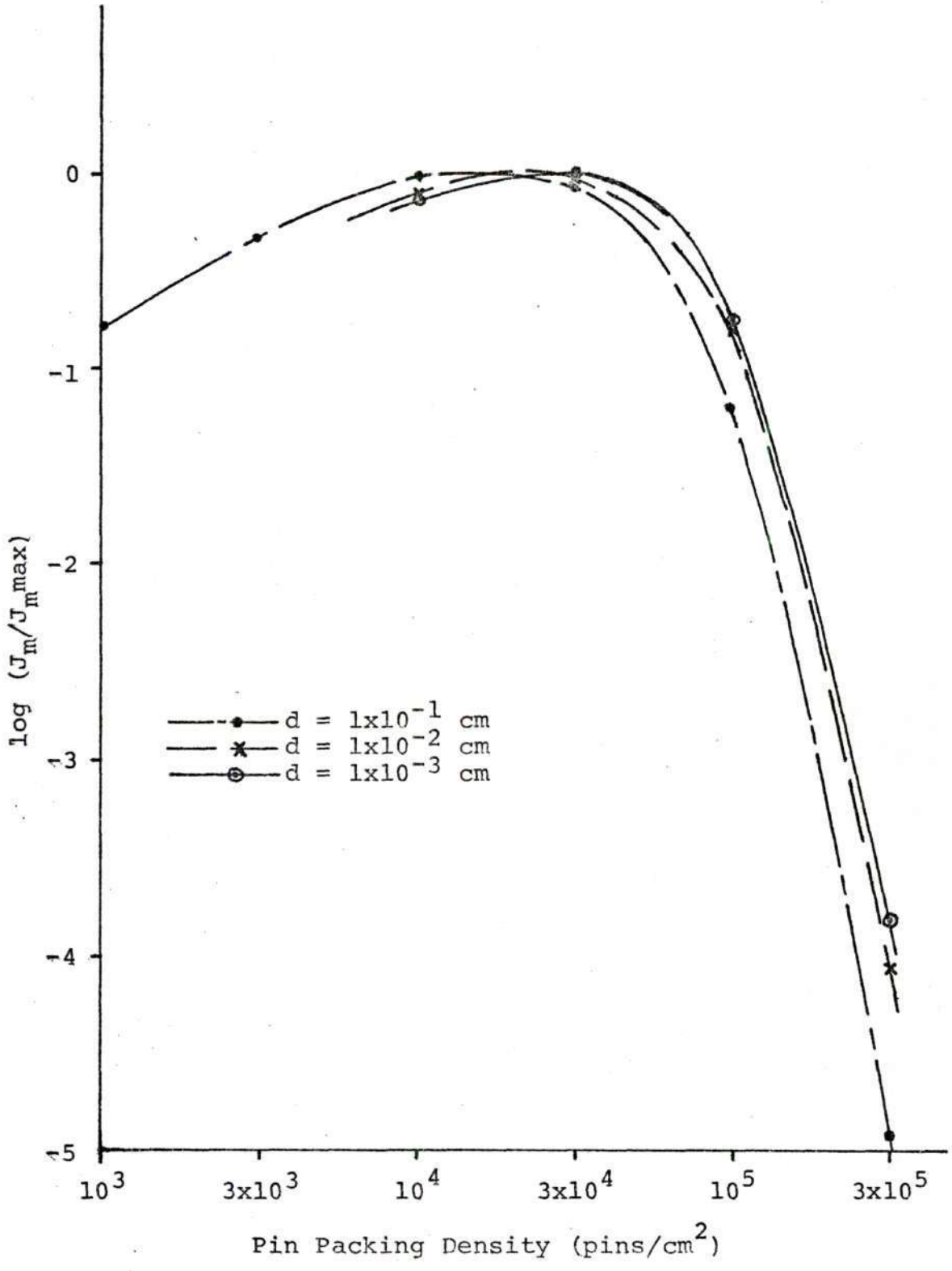

Figure 22. Logarithm of the Normalized Macroscopic Current Density as a Function of Pin Packing Density

density or greater it is obvious that regardless of the inter-electrode spacing used the packing density of the pins was always substantially greater than the optimum. If a parameter such as an effective packing density for the edge pins of an array is considered, it is obvious that this density would be lower than the bulk packing density, and would according to the data presented lead to a substantial increase in J_m at the array edge.

Thus, a two-fold effect leads to the enhanced edge emission of the large anode-small cathode geometry; the first due to enhancement of the macroscopic field at the edge pins and the second due to packing density considerations. Quantitative description of these effects is extremely difficult, thus this essentially qualitative approach must suffice, but it is apparent that the strongly enhanced edge emission observed experimentally has been explained.

The results described above led to utilization of the small anode-large cathode geometry for the experiments described in the following section. It is felt that this geometry allowed observation of the field enhancement due to the pins of the array only, with no spurious influence from edge effects.

Effects of Interelectrode Spacing, Pin Tip Radius and Packing Density

A number of samples were utilized for the studies described in this section. The preparation of these samples has been previously described in general terms, but the exact characteristics

and supporting photomicrographs will be given in the course of this discussion.

Interelectrode Spacing

A scanning electron micrograph of the sample utilized for determination of the effect of interelectrode spacing on the field enhancement factor is given in Figure 23. The sample had a packing density of 4.1×10^6 pins per cm^2, pin diameters of approximately 0.8 μm, and pin heights of 25 μm. The interelectrode spacing was varied from 5.1×10^{-3} cm (0.002 inches) to 1.0×10^{-1} cm (0.040 inches). The data related to this study are given in Table 4, where the slopes, m, of the Fowler-Nordheim plots obtained at seven spacings within the stated range of interelectrode spacings are presented.

Utilizing equation (20), given again here for convenience,

$$m = \frac{-2.97 \times 10^7 \ \phi^{3/2} \ s(y)}{\beta},$$

values of β were calculated for each of the interelectrode spacings. In order to make this calculation a value of the work function, $\phi = 6.6$, was assumed. This is not an unreasonable assumption in view of the following discussion.

Since no information was obtainable as to the actual surface condition of the pins vis-a-vis, extent of oxidation or composition and extent of adsorbed gas layers, a literature search was undertaken to determine the likely state of the W surface. The pins as grown were assumed to be pure W. This is reasonable in light of the results of Lin[60] showing that the

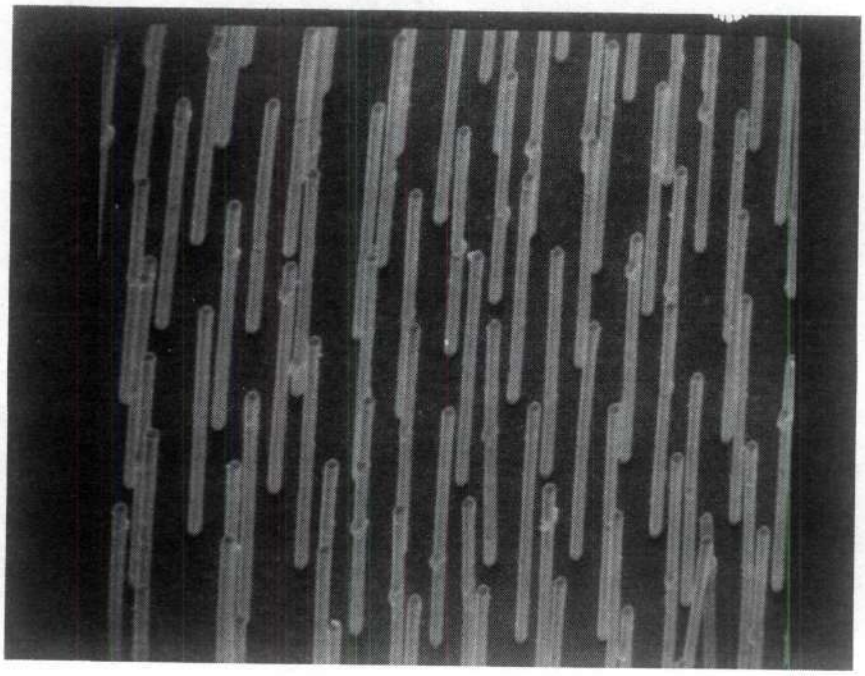

Figure 23. Scanning Electron Micrograph of the Sample Used in the Interelectrode Spacing Test. x2550

Table 4. Experimental Fowler-Nordheim Plot Slopes with Experimental and Theoretical β Values for Interelectrode Spacing Test.

Interelectrode Spacing (cm)	m	β_{exp}	β_1	β_2
5.1×10^{-3}	-4.05×10^{3}	1.18×10^{5}	1.08×10^{5}	1.10×10^{5}
"	-5.23×10^{3}	9.14×10^{4}		
7.6×10^{-3}	-7.03×10^{3}	6.80×10^{4}	9.69×10^{4}	8.81×10^{4}
1.3×10^{-2}	-1.10×10^{4}	4.34×10^{4}		
"	-1.08×10^{4}	4.42×10^{4}	7.88×10^{4}	6.16×10^{4}
"	-1.19×10^{4}	4.02×10^{4}		
2.5×10^{-2}	-1.85×10^{4}	2.58×10^{4}	5.58×10^{4}	3.70×10^{4}
"	-1.97×10^{4}	2.43×10^{4}		
5.1×10^{-2}	-4.10×10^{4}	1.16×10^{4}	3.41×10^{4}	1.98×10^{4}
7.6×10^{-2}	-6.83×10^{4}	7.00×10^{3}	2.49×10^{4}	1.37×10^{4}
1.0×10^{-1}	-9.51×10^{4}	5.03×10^{3}	1.94×10^{4}	1.05×10^{4}

lattice constant observed for W in the unidirectionally solidified UO_2-W eutectic is in close agreement with the ASTM value. It is known, however, that etchant mixtures containing a combination of nitric acid and hydrofluoric acid, such as the one used to produce the emitter arrays of this study as described previously, attack W by first oxidizing the metal and then removing the oxide by dissolution in HF.[61] This process undoubtedly leaves the surface to some extent oxygen contaminated. Furthermore, Bondarenko[62] has summarized various works showing the predominance of adsorption of oxygen on the surface of tungsten from residual gas atmospheres containing N_2, H_2, CO, and O_2. Thus it seems most unlikely that any adsorbate other than oxygen will occur to any significant degree on the pin surfaces used in this study.

A review of the work function values reported for oxygen contaminated and oxidized tungsten surfaces reveals that a value of $\phi = 6.6$ is quite reasonable. The reported data are tabulated in Table 5.

Another consideration in calculating the value of β from equation (20) is the value of the function s(y) which arises from the differentiation of the image correction function in the exponential portion of the Fowler-Nordheim equation. As stated in equation (11) y is a function of the work function ϕ, assumed to be 6.6 here, and the applied field E. A value of the applied field which falls within the range of fields used for each of the experimental curves, $E = 9 \times 10^7$ V/cm,

Table 5. Reported Overall Work Function Values for Oxygen-Contaminated Tungsten.

Author(s)	Reference No.	ϕ(eV)
Müller	63	6.6
Becker and Brandes	64	6.6-6.8
Müller	65	6.6
Gomer and Hulm	66	6.4
George and Stier	67	6.8
Menzel and Gomer	68	6.4

was chosen for the purpose of calculating β. From equation (11) a value of $y = 0.54$ was obtained and a value of $s(y) = 0.95$ was calculated from the following equation,

$$s(y) = -0.167y^{1.9047} + 1. \qquad (37)$$

This equation was obtained by trial and error fitting to the data of Burgess, et al.[17], and is plotted in Figure 24. The maximum error in values calculated from this relationship compared to those given by Burgess, et al., is approximately 0.06%, and values of $s(y)$ are considerably more readily obtained by using equation (37) than by interpolation from the published data.

The values of ϕ and $s(y)$, determined as described, used in conjunction with the slope values for the Fowler-Nordheim plots allow calculation of experimentally determined values of the field enhancement factor, β_{exp}. These are reported in Table 4 and plotted in Figure 25.

The Levine model for determination of the field enhancement factor[35] is the only reasonable theoretical model which can be used for comparison with these experimental results since it is the only multi-pin model which considers the interelectrode spacing. However, one modification should be made. In his development Levine assumes the field at the tip of an isolated pin to be that at the surface of an isolated sphere, $E = V/r$, but as has been pointed out in a previous section the effect of the pin shank and the pin tip shape must be considered. This is

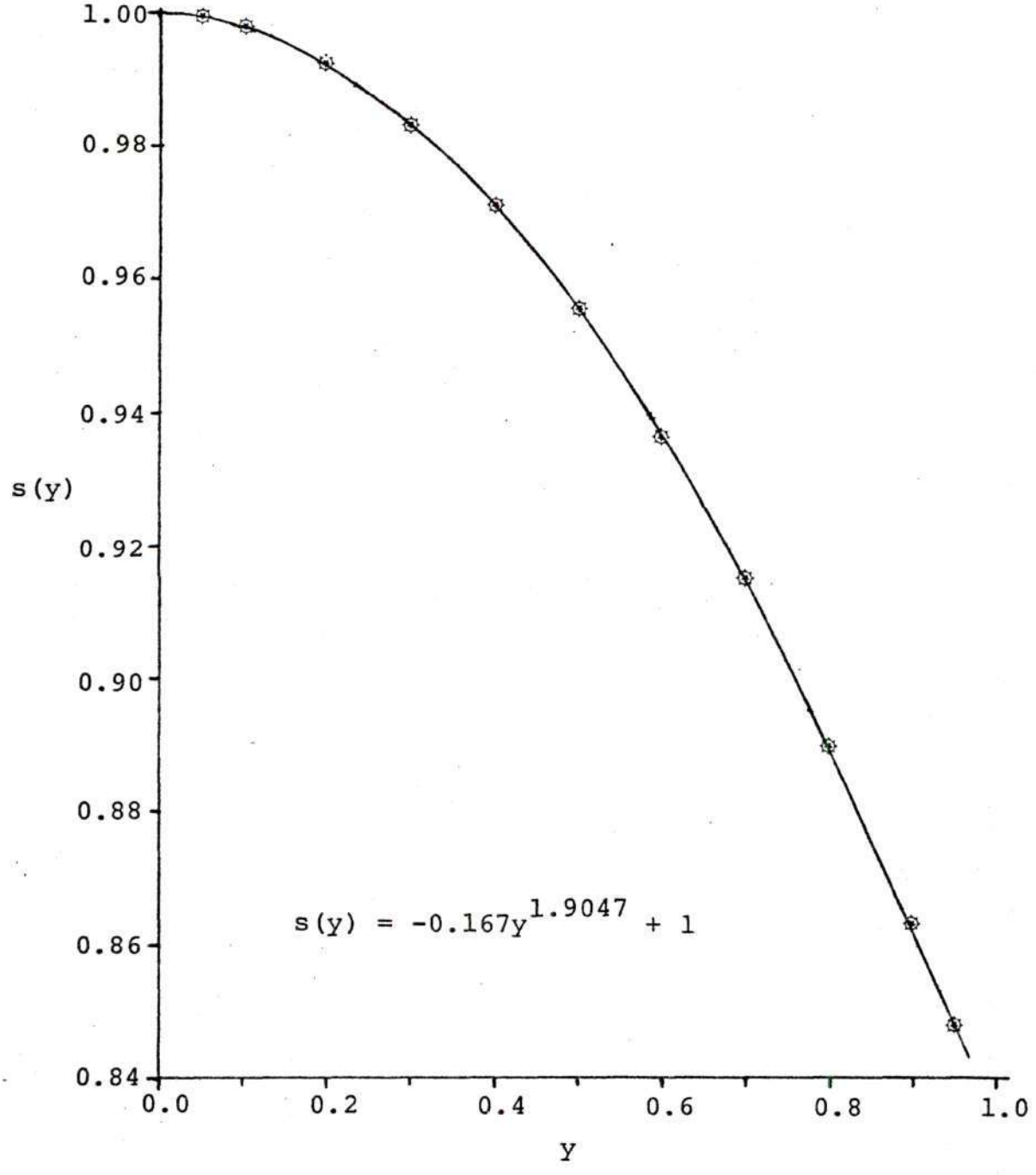

Figure 24. The Function s(y) as a Function of y.

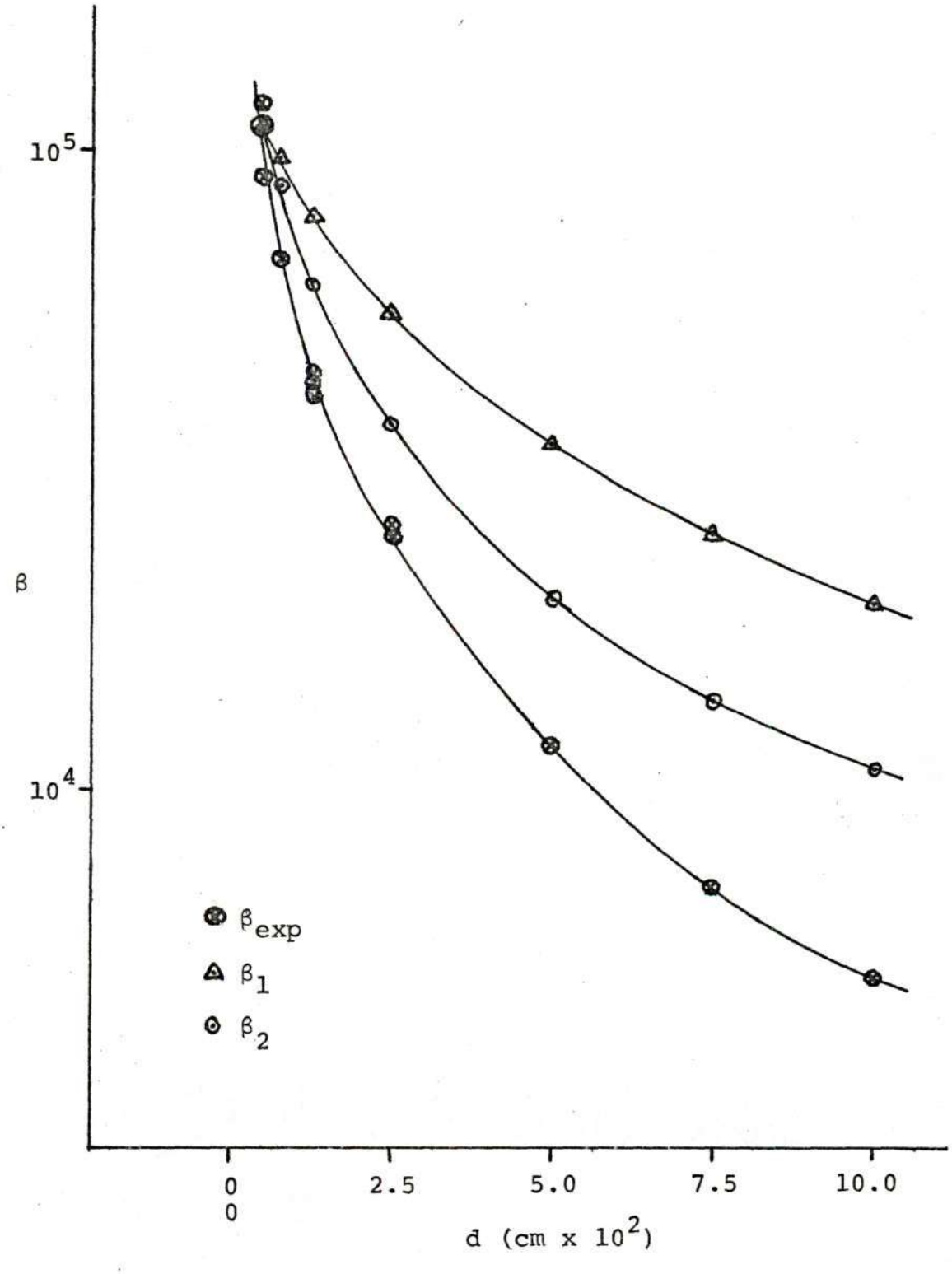

Figure 25. Experimental and Theoretical Values of β as a Function of Interelectrode Spacing.

done by adding a factor, k, as shown in Equation (22) taking into account the reduction of the field at the tip due to the effects noted above. Models yielding values for k were discussed previously on the basis of a number of assumed pin tip shapes none of which, however, remotely approximate the blunt, cylindrical pins utilized in this set of experiments. Gomer[69] has pointed out that all of the various models yield values of $k \cong 5$, and that assumption of this value is often adequate.

Using a value of $k = 5$, a value for r was determined which gave good agreement between the experimentally determined value of β and the theoretically calculated value at a spacing of 5.1×10^{-3} cm. The theoretical values of β were then calculated for all other interelectrode spacings used experimentally using the assumed value of $r = 1.4 \times 10^{-6}$ cm and are presented in Table 4. The following equation was used to calculate theoretical β_1 values,

$$\beta_1 = \frac{1}{5r\ (1 + \frac{4\pi dr}{a^2})} \quad . \tag{38}$$

It should also be noted that the value of a used for these calculations was determined from the following expression relating packing density and pin spacing distance for an hexagonal array,

$$a = 1.075\ \sqrt{\rho}\ , \tag{39}$$

rather than the previously noted relationship for a square array. This has a minimal effect on the calculated values, and is

intentional variation of the macroscopic pin tip radius.

Pin Tip Radius

The results reported in this section describe a series of experiments in which an attempt was made to study the change in the field enhancement factor of a pin array as a function of the pin tip radius. Three tip geometries were tested utilizing a single UO_2-W sample in order to maintain the packing density and pin diameter as nearly constant as possible. Each sample geometry was sequentially produced from the composite using a minimum of grinding and polishing so as to utilize the immediately adjacent portion of the sample for each successive test. Inspection of the sample showed that each time the packing density was 8.7×10^6 pins/cm^2, with no more than 0.1×10^6 pins per cm^2 variation, and that the pin diameter was a consistent 0.40 - 0.45 μm.

Sample number R-1 was prepared with conically pointed fibers using the procedure described previously. The pins on this sample were 10 μm ± one μm in height. A scanning electron micrograph of this sample is presented in Figure 26 (a) giving a detailed view of the tip geometry. It is readily apparent from this micrograph that the tip radius is not resolvable by the SEM, but is certainly not more than 20% of the pin radius. The tip radius is estimated to be no more than 400 Å.

Sample number R-2 was prepared with approximately hemispherical tips by an ion milling process. After exposure of blunt, cylindrical pins by the etching process previously

(a)

(b)

(c)

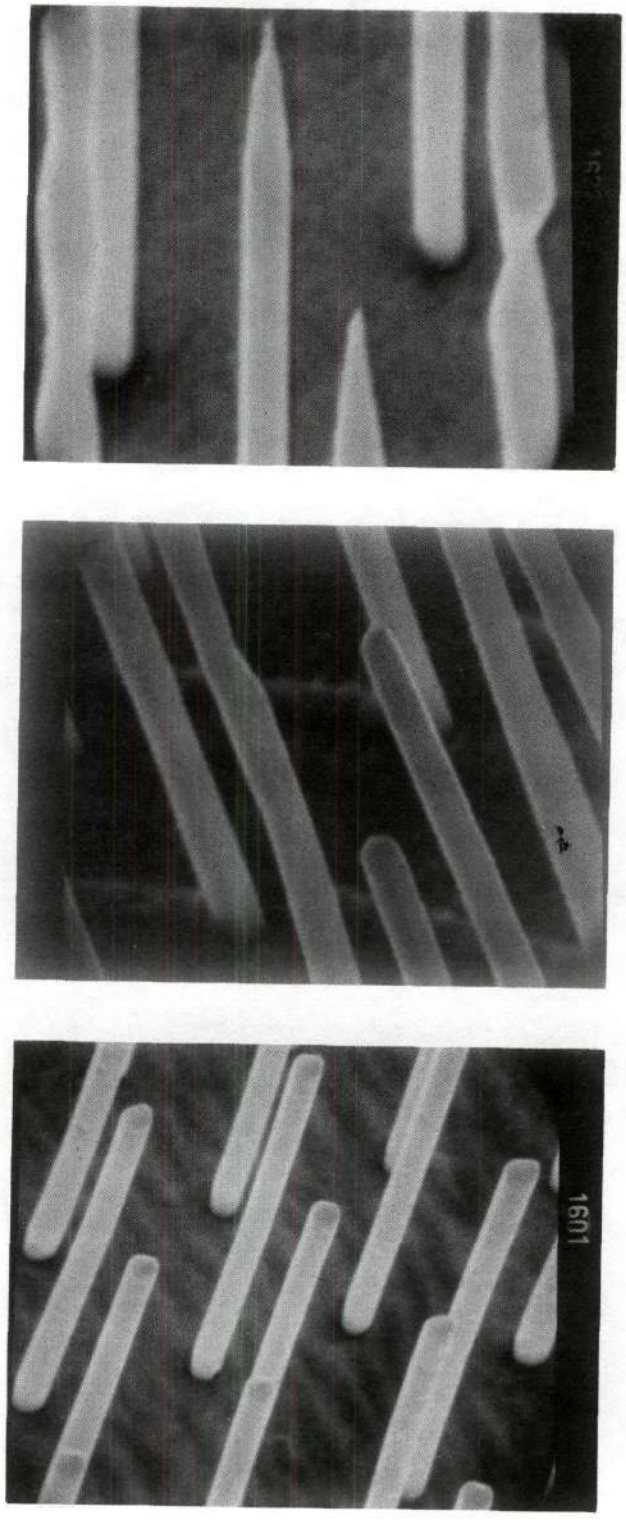

Figure 26. Scanning Electron Micrographs of the Samples Used in the Pin Tip Radius Test. (a) x15050, (b) x15750, (c) x8190

described, the array was ion-milled for 230 μA-minutes in an 8 kV argon ion beam in order to produce the tip geometry shown in Figure 26 (b). The tip radius in this instance is equal to the pin radius of about 0.2 μm or 2000 Å. Once again the pin height was 10 μm ± one μm. The two samples, R-1 and R-2, provide the largest variation in readily definable tip radii.

A third sample R-3 was simply etched to expose blunt cylindrical pins of 12 μm ± one μm height. Figure 26 (c) presents a scanning electron micrograph of this tip geometry. There is no definable measure of tip radius for this sample, but the sharp corners of the cylindrical tip obviously produce significant local field enhancement.

Once again analysis of the experimental results is dependent upon the value of the slope of the Fowler-Nordheim plot for each sample. β_{exp} values were calculated using equation (20) as described in the previous discussion section, except that an iteration process was used to determine a value for s(y). An initial calculation was made with an assumed s(y) value giving an approximate value for β. This β value was then used along with the largest applied voltage utilized in obtaining the Fowler-Nordheim data to calculate an applied field, E_1. E_1 was then used in equation (7) to calculate a value for y, using the assumed ϕ of 6.6 as per the discussion presented previously. A new s(y) value was obtained from equation (34), and in turn used to calculate a new β value. Successive applications of this technique quickly yielded the required values for β_{exp}.

All data related to these calculations are presented in Table 6.

Comparison of the experimental results with theory again uses the model for field enhancement developed by Levine.[35] Values of field enhancement factors were calculated using the two models described in the earlier discussion of the effect of interelectrode spacing, and values for β_1 and β_2 are presented in Table 7 for comparison with the β_{exp} values. Since the r value for sample R-3 is not definable, no β values have been calculated for this sample. It is apparent that the values of β_{exp} are considerably larger than the values calculated from Levine's equation or from the modified form; and it should also be noted that although the value of r as determined from the micrographs was varied over a range sufficient to change the theoretical β values by more than a factor of twenty, the values for β_{exp} are essentially identical.

If the extreme values of the experimentally determined field enhancement factor, $\beta = 7.99 \times 10^4$ and $\beta = 1.35 \times 10^5$, are used to calculate the corresponding r values with both the Levine equation (1/r model) and the modified equation (1/5r model) values of r as shown in Table 8 are obtained. The consistency of these estimated values for r with the range of 140 to 450 Å found in the previous section is noteworthy.

The conclusion that the radii of the emission sites on arrays of this type are on the order of 100 to 200 Å would appear entirely reasonable. Later in the discussion the effect of this finding on overall performance estimates will be

Table 6. Experimental Fowler-Nordheim Plot Slopes and Experimental β Values for Pin Tip Radius Test.

Sample No.	Tip Shape	m	V_{max}	s(y)	β_{exp}
R-1	Pointed	-5.48×10^3	2.82×10^3	0.87	7.99×10^4
R-2	Hemispherical	-5.03×10^3	2.75×10^3	0.87	8.72×10^4
R-3	Blunt	-3.24×10^3	1.71×10^3	0.87	1.35×10^5

Table 7. Comparison of Experimental and Theoretical β Values for Pin Tip Radius Test.

Sample No.	Tip Shape	β_{exp}	β_1	β_2
R-1	Pointed	7.99×10^4	8.59×10^3	4.30×10^4
R-2	Hemispherical	8.72×10^4	3.98×10^2	1.99×10^3
R-3	Blunt	1.35×10^5	--	--

Table 8. Experimentally Determined Emitting Area Radii.

Sample No.	β_{exp}	Model Type	r(Å)
R-3	1.35×10^5	1/5r	75
R-3	1.35×10^5	1/r	210
R-1	7.99×10^4	1/5r	105
R-1	7.99×10^4	1/r	285

reasonable in view of the nearly hexagonal array structure occurring in the UO_2-W composite materials.

The calculated values of β_1 are also plotted in Figure 25 for comparison to the experimentally determined ones. It is apparent that the discrepancy between the experimental values and the β_1 values is significant. As an alternative the Levine model without modification, i.e., k = 1, was also used to calculate values of the field enhancement factor. These are designated β_2 and are tabulated in Table 4 and plotted in Figure 25 for comparison. The agreement between these values and the experimental results is better than for the β_1 values. A similar method was used for calculation of these values, and $r = 4.5 \times 10^{-6}$ cm was found necessary to provide agreement between the experimental and β_2 values at an interelectrode spacing of 5.1×10^{-3} cm.

The predicted decrease in β as interelectrode spacing is increased is observed experimentally, but the manner in which this decrease relates to interelectrode spacing differs from that predicted by Levine's derivation. The same general shape is observed for the experimental and theoretical curves in Figure 25, but as a result of the inability to precisely define r and k on the basis of tip geometry, quantitative agreement is out of the question.

One important point for consideration, however, is the fact that r values of at least an order of magnitude less than the pin radius are indicated. This same feature will be considered in the following discussion, related to the effect of

considered, but first this section will be concluded with a short consideration of the effects of pin packing density on array performance.

Packing Density

Extreme difficulty was encountered in obtaining suitable emission samples for this part of the research. An excellent sample of 7.5×10^6 pins per cm^2 density was obtained with rounded, approximately hemispherical tips. This tip morphology was obtained by heating conically pointed tips to 1400°C for 15 minutes in an induction heating unit using an H_2 atmosphere. As can be seen from Figure 27 (a), this technique produced a good quality sample. Unfortunately results of this quality were not obtained with a sample of higher density (16.6×10^6 pins/cm^2) and a less perfect tip structure had to be utilized. A scanning electron micrograph of this structure is given in Figure 27 (b). It proved impossible to point fibers in samples of the minimum density available ($2\text{-}5 \times 10^6$ pins/cm^2) apparently as a result of a difference in the pin surface composition. Thus only two samples were tested for this portion of the research, one of 7.5×10^6 pins/cm^2 density and the other of 16.6×10^6 pins/cm^2 density; they are designated D-1 and D-2, respectively.

Other parameters were essentially identical with pin heights for both samples of eight to nine μm and pin diameters of 0.4 μm. The test diodes were operated at a spacing of 5.1×10^{-3} cm.

The slopes of the Fowler-Nordheim plots for these two

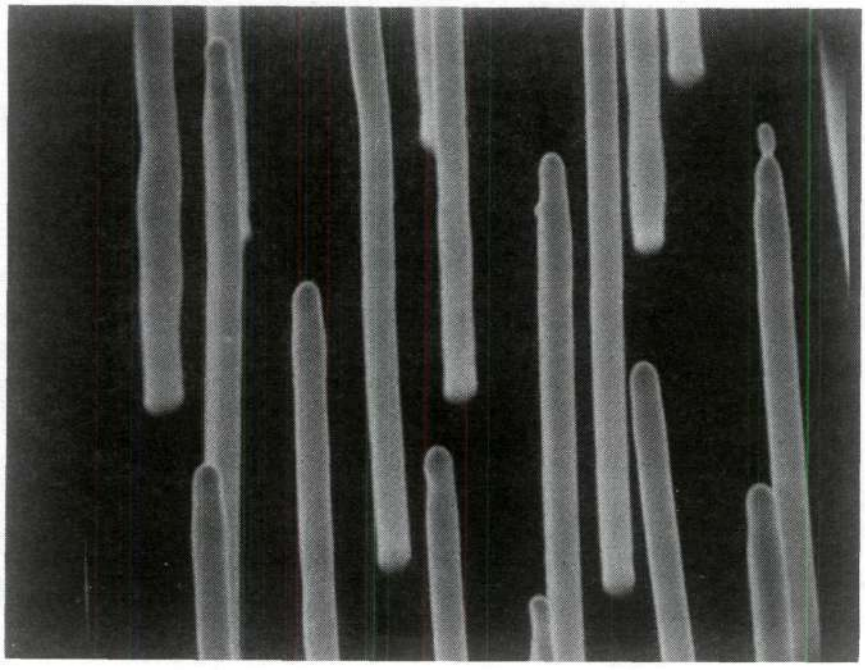

(a)

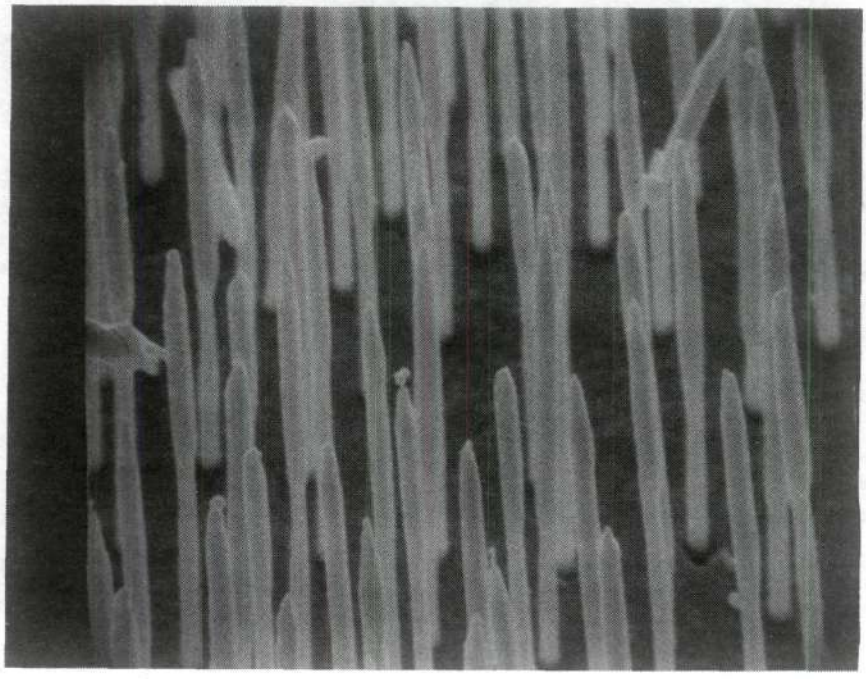

(b)

Figure 27. Scanning Electron Micrographs of the Samples Used in the Pin Packing Density Test. (a) x12000, (b) x7900

samples (Table 9) were very nearly identical, differing by less than 10%. The procedure described in the previous section of this discussion was used to calculate the β_{exp} values, and as before these results are compared with the theoretical values of the two models also described previously. The theoretical β values are compared with the experimental results in Table 10; an r values of 1.4×10^{-6} cm or 140 Å was used to calculate the β_1 and β_2 values. It is evident that the experimental β value for sample D-2 does not follow the predicted pattern. It is probable that the poor tip morphology of this sample compared to that of D-1 is the cause of the discrepancy, and that further investigation with more adequately controlled geometries would provide more conclusive results.

Throughout the course of the research it was observed that repeatability of uniform tip geometries under the same preparation conditions was somewhat less than assured, and there is evidence that a significant distribution in tip radii exists in any given sample. This point will be considered further in the remainder of the discussion.

This completes the discussion of the effects of the geometrical diode and array parameters. The following section will be a qualitative discussion of a number of factors influencing and limiting emitter performance, but which do not lend themselves to quantitative evaluation in this study.

Table 9. Experimental Fowler-Nordheim Plot Slopes and Experimental β Values for Pin Packing Density Test.

Sample No.	Packing Denstiy (pins/cm^2)	m	s(y)	β_{exp}
D-1	7.5×10^6	-1.05×10^3	0.84	4.03×10^5
D-2	16.6×10^6	-9.60×10^2	0.86	4.51×10^5

Table 10. Comparison of Experimental and Theoretical β Values for Pin Packing Density Test.

Sample No.	β_{exp}	β_1	β_2
D-1	4.03×10^5	4.51×10^5	9.02×10^4
D-2	4.51×10^5	2.86×10^5	5.73×10^4

Performance Limitations

A major theoretical advantage of the multiple-pin field emitter is its ability to produce large emission currents. However, in order to be considered a viable alternative to thermionic cathodes, the field emission cathode arrays must match the three to eight A/cm^2 current density capability available with such devices. One of the major interests in this research was to determine the current density performance limits of the oxide-metal composite arrays studied here, and to delineate the factors which limit the available current density. The foregoing discussion has shown the effects of the diode and array geometry upon the field enhancement factor of the arrays. Experimentally determined values of the field enhancement factor and emitting area radius are used in this section to define the theoretical capabilities of an array and the theoretical model is compared with the experimental information.

The experimental cathode array (sample W-6) on which the theoretical model will be based is shown in Figure 28. The experimental results obtained from this array will be used for comparison. From a Fowler-Nordheim plot of field emission data derived from this sample β was calculated to be 3.5×10^5 using the technique described earlier in this discussion. Based on this value of β, the tip radius r of the active emission areas was calculated using the diode and array parameters shown below,

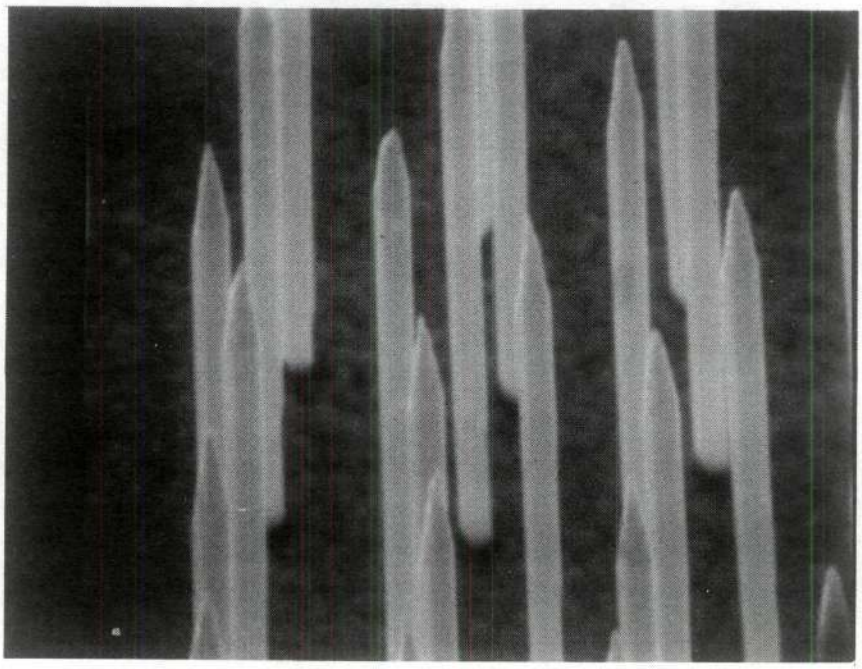

Figure 28. Scanning Electron Micrograph of Sample W-6. x14000

$$\rho = 16.6 \times 10^{6} \text{ pins/cm}^2 ,$$

$$d = 2.5 \times 10^{-3} \text{ cm.}$$

Assuming a square array the interpin spacing a was calculated to be 2.45×10^{-4} cm, and equation (29) yielded a value of 1.57×10^{-6} cm for r. Since experimental data were available over a voltage range of 240 to 510 volts, corresponding to field values of 8.4×10^{7} to 1.8×10^{8} V/cm, a corresponding range of field strengths was considered in development of the theoretical Fowler-Nordheim plot. The current densities for a clean surface, J, were calculated for numerous field strengths within the stated range and are tabulated in Table 11. A work function of 6.6 eV was assumed. Based on information from Gomer and Hulm[66] the calculated J values were reduced by a factor of 5×10^{2} to account for effect of the adsorbed gas layer on the pre-exponential part of the field emission equation. This yielded the values of J' given in Table 11. Also calculated were the macroscopic current density J_m (current per unit array area) as given by equation (35) and the actual emission current I based on an active array area of 1.76×10^{-2} cm^2. This corresponds to the area of the anode used experimentally which was of the type shown in Figure 15 (c).

In order to facilitate calculation of the data necessary for the Fowler-Nordheim plot empirical equations were derived for the image-force correction functions, f(y) and t(y). The equations are as follows:

Table 11. Calculated Current Densities and Gross Emission Currents for the Theoretical Array as a Function of Applied Field.

E(V/cm)	J(A/cm^2)	J'(A/cm^2)	J_m(A/cm^2)	I(A)
8×10^7	7.12×10^4	1.42×10^2	1.83×10^{-2}	3.22×10^{-4}
9×10^7	4.49×10^5	8.98×10^2	1.16×10^{-1}	2.04×10^{-3}
1.0×10^8	1.78×10^6	3.56×10^3	4.59×10^{-1}	8.08×10^{-3}
1.1×10^8	5.59×10^6	1.12×10^4	1.44	2.53×10^{-2}
1.2×10^8	1.62×10^7	3.24×10^4	4.18	7.36×10^{-2}
1.3×10^8	3.68×10^7	7.36×10^4	9.49	1.67×10^{-1}
1.4×10^8	7.54×10^7	1.51×10^5	1.95×10^1	3.43×10^{-1}
1.5×10^8	1.42×10^8	2.84×10^5	3.66×10^1	6.44×10^{-1}
1.6×10^8	2.47×10^8	4.94×10^5	6.37×10^1	1.12
1.7×10^8	4.08×10^8	8.16×10^5	1.05×10^2	1.85
1.8×10^8	6.40×10^8	1.28×10^6	1.65×10^2	2.90

$$f(y) = -y^{1.7} + 1, \tag{40}$$

$$t(y) = 0.1107y^{1.4305} + 1. \tag{41}$$

These equations are plotted in Figures 29 and 30, respectively, along with the values reported by Burgess, et al.[17], and Good and Müller[18] (see Table 1). An error no greater than 0.3% is incurred by use of these expressions.

Voltage values corresponding to the field values used to generate the data displayed in Table 11 were calculated, and in conjunction with the emission current values were used to complete the calculations of the Fowler-Nordheim data as shown in Table 12.

The data of Table 12 were used to produce a theoretical Fowler-Nordheim plot as given in Figure 31 (upper curve). Also shown in this figure is a typical experimental result for the actual sample. A difference of more than a factor of 10^2 exists between the actual and predicted performance. Reduction of the theoretical emission current values by a factor of 3.26×10^2 yields the third curve of Figure 31, which is seen to correspond closely to the experimental curve for values of $10^4/V$ greater than 31. This voltage corresponds to a current density J' of about 1.1×10^4 amps/cm^2.

The need to reduce the theoretical current values by a factor of 3.26×10^2 in order to obtain agreement with the experimental results can be interpreted to mean that only a

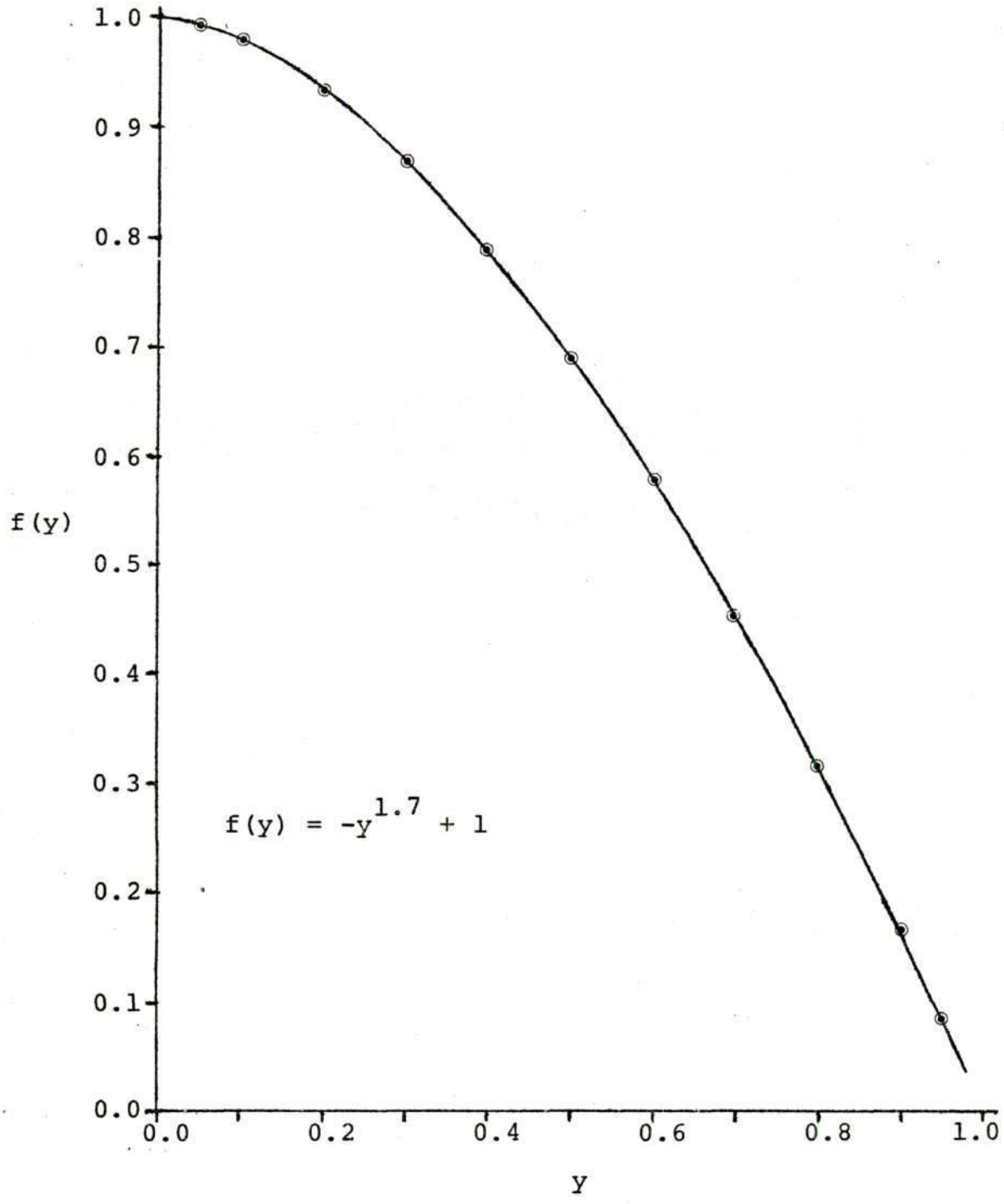

Figure 29. The Image Correction Function f(y) as a Function of y.

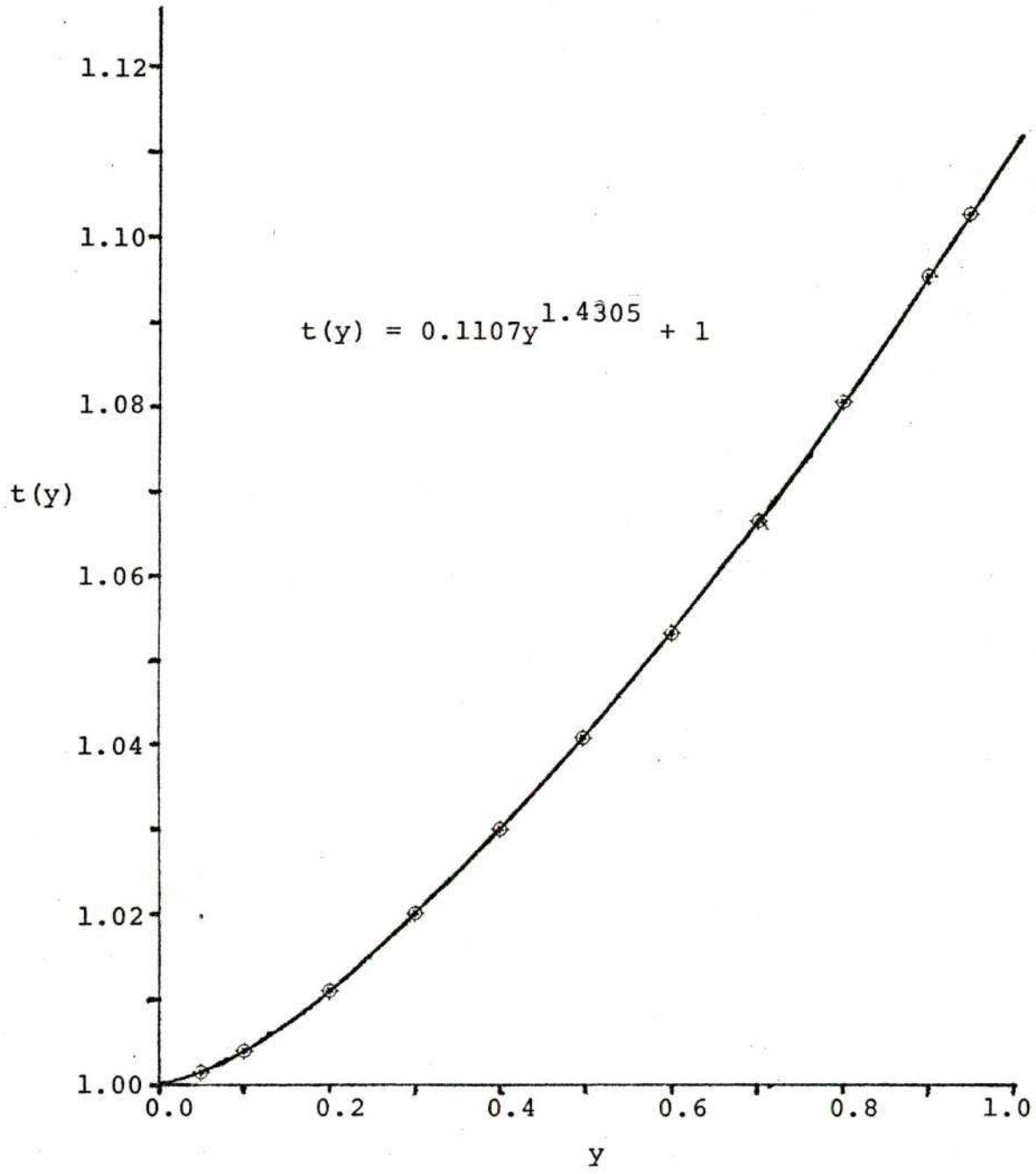

Figure 30. The Image Correction Function t(y) as a Function of y.

Table 12. Data for Fowler-Nordheim Plot for Theoretical Array.

V(in V)	I(A)	$10^4/V$	I/V^2
2.28×10^2	3.22×10^{-4}	43.86	6.19×10^{-9}
2.57×10^2	2.04×10^{-3}	38.91	3.09×10^{-8}
2.86×10^2	8.08×10^{-3}	34.96	9.88×10^{-8}
3.41×10^2	2.53×10^{-2}	31.85	2.57×10^{-7}
3.43×10^2	7.36×10^{-2}	29.15	6.26×10^{-7}
3.71×10^2	1.67×10^{-1}	26.95	1.21×10^{-6}
4.00×10^2	3.43×10^{-1}	25.00	2.14×10^{-6}
4.28×10^2	6.44×10^{-1}	23.36	3.52×10^{-6}
4.57×10^2	1.12	21.88	5.36×10^{-6}
4.86×10^2	1.85	20.58	7.83×10^{-6}
5.14×10^2	2.90	19.46	1.10×10^{-5}

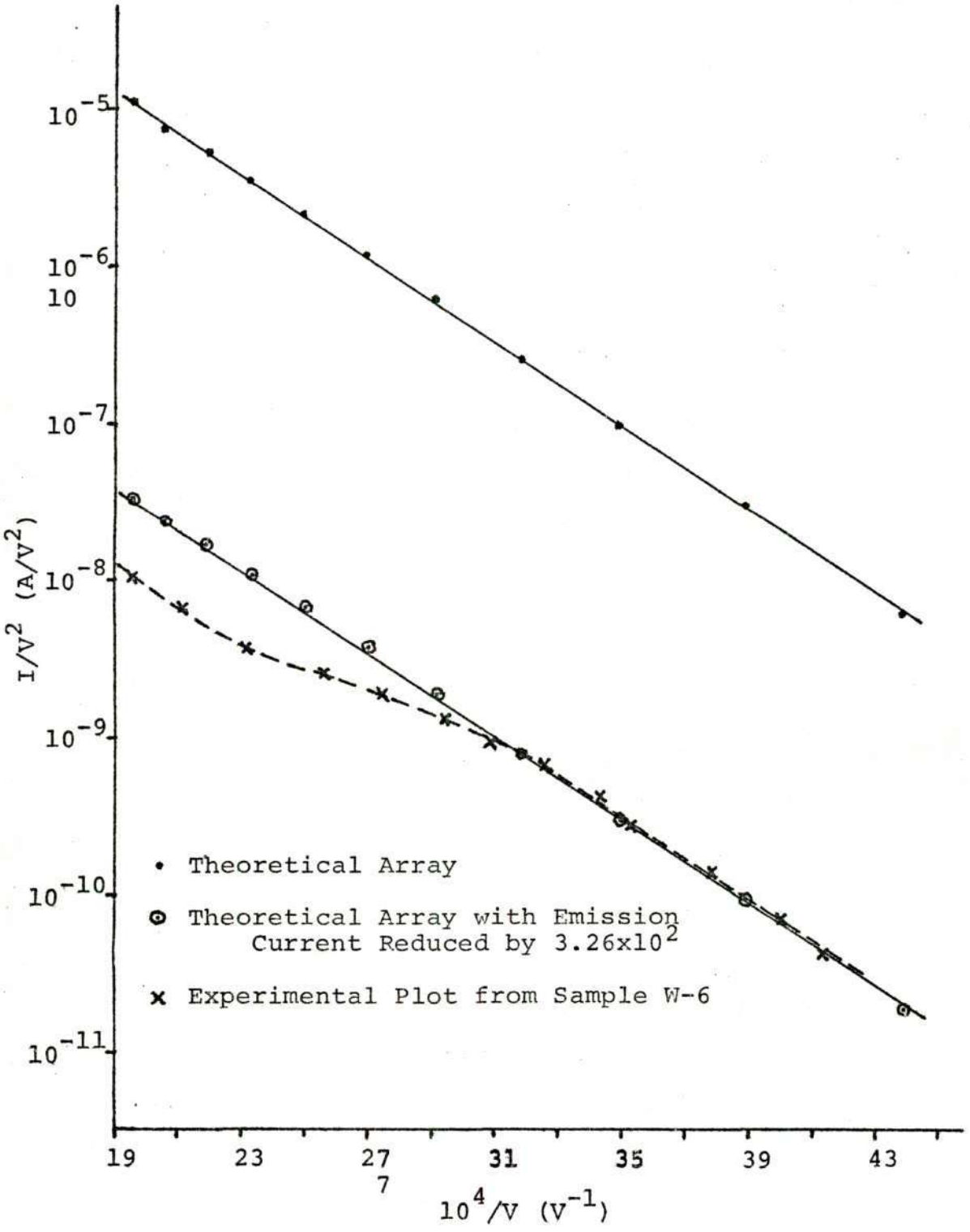

Figure 31. Fowler-Nordheim Plots for Sample W-6 and the Theoretical Arrays.

small fraction, less than 1% and possibly as little as 0.3%, of the available pins are contributing to the total emission current. It is felt that this is primarily the result of the existance of non-uniform tip geometries. Further evidence for this will be presented, but the shape of the Fowler-Nordheim curve at values of $10^4/V$ less than 31 must first be considered.

A concave downward curvature of the Fowler-Nordheim plot is to be expected as a result of the image-force correction. It can in fact be observed to a small degree in the theoretical plots of Figure 31. The extent of curvature observed experimentally, however, is substantially greater than would be expected from the image-force correction and does not appear to be entirely a result of this correction.

The general shape of the experimental Fowler-Nordheim curve is similar to that reported by Barbour, et al.[70], for the case of space charge limited field emission. Space charge effects are reported to be unobservable below current densities of 6×10^6 A/cm^2. The theory and experimental results of Barbour, however, are applicable only to the case of plane electrodes or to the case where the radius of curvature of the cathode surface is much greater than the distance above the cathode surface within which the space charge is sufficient to alter the cathode field. For Barbour's case the critical current density of 6×10^6 A/cm^2 was enough to establish sufficient space charge within a distance of 2×10^{-6} cm from the surface over a

cathode of approximately 2×10^{-5} cm radius. In the case of the array studied here the curvature of the emission areas has been estimated to be 1.6×10^{-6} cm. As noted by Barbour an exact solution for this geometry is not possible, and it is difficult to establish the critical current density for the case of emitters of such small radius.

Another consideration is the fact that Barbour's study involved clean W surfaces or surfaces with adsorbed Ba. In the present case the surface is contaminated by oxygen. No report of the effects of adsorbed gases on critical current densities for space charge could be found in the literature.

The foregoing discussion of space charge effects presents a possible explanation for the shape of the experimentally determined Fowler-Nordheim curve. Space charge effects are in fact the only reasonable explanation for a downward inflection of the observed magnitude. Consideration of the effects of the existence of a distribution of tip radii, however, can help to explain the subsequent upturn of the experimental curve which can perhaps be only partially attributed to space charge.

If the theoretical Fowler-Nordheim curve of Figure 31 is replotted with the emission currents reduced by a factor of 1×10^{2}, the lower of the two curves shown in Figure 32 results. This is the curve which would be expected of the theoretical array previously developed if one percent of the pins were contributing to the emission and each of them had a tip radius of 1.57×10^{-6} cm. Using the same set of assumptions

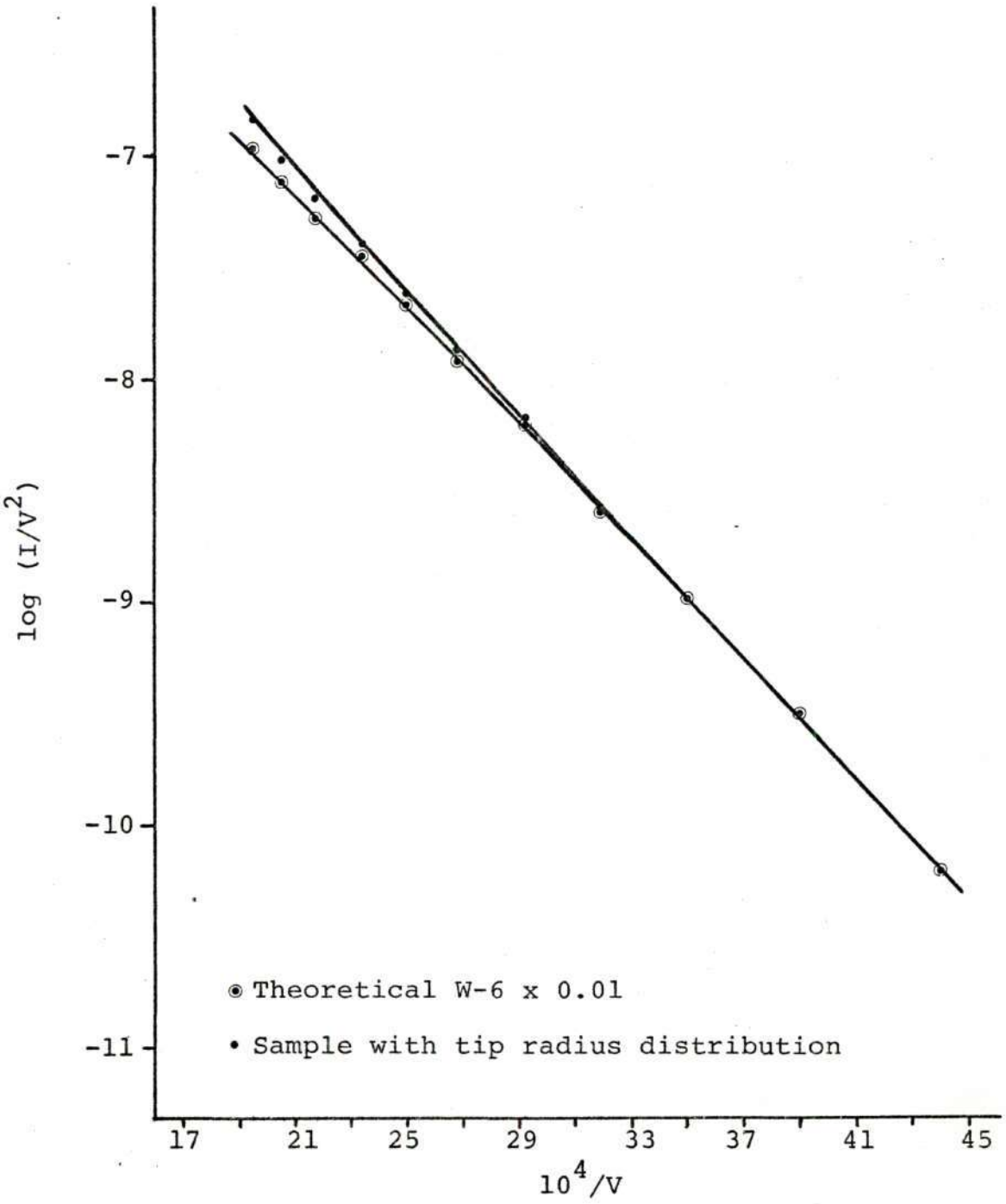

Figure 32. Fowler-Nordheim Plots Showing the Effect of a Distribution of Tip Radii.

as previously described an approximate calculation of the effect of the tip radius distribution shown in Figure 33 was made. As illustrated the distribution was approximated by groups of pins of a single given size each representing a percentage of the total pins present. The distribution is given in tabular form in Table 13. Calculation of the total emission current was accomplished by summation of the current contributions from each of the pin size groups, yielding the data tabulated in Table 14. These data were then used to obtain the Fowler-Nordheim data also given, which yield the curve represented by the upper one in Figure 32. Thus such a distribution of tip radii would result in a 30% increase in emission current at the highest applied field considered and would enhance the upward curvature of the Fowler-Nordheim plot.

The information presented in this discussion provides some insight into the reasons for not meeting the theoretical performance expectations. Further discussion of the experimentally determined current density limits is warranted. The data presented thus far have not represented the maximum emission currents obtained, but have been chosen as representative of typical emission results taken for the purpose of studying geometrical parameters by means of Fowler-Nordheim data. Since emission currents of more than five mA led to heating of the anode and subsequent interelectrode spacing variations even in the water-cooled diode. This behavior precluded use of this data for the foregoing discussion. In Figure 34 the emission

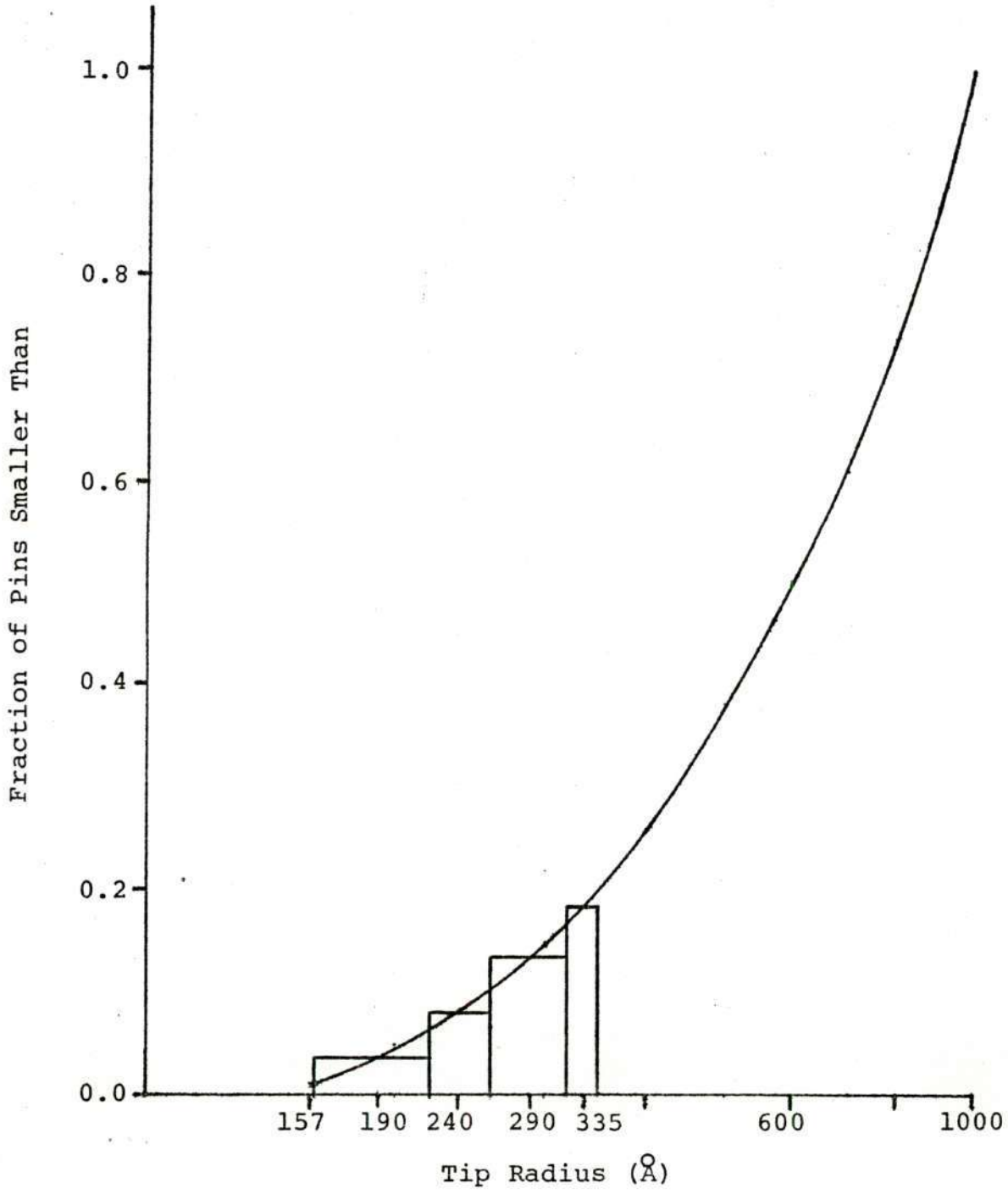

Figure 33. Assumed Distribution of Tip Radii

Table 13. Assumed Distribution of Pin Tip Radii.

Tip r ($cm \times 10^6$)	% of Pins w/Radii <r	r Interval ($cm \times 10^6$)	% of Pins in Interval
1.57	1	<1.60	1
1.90	4	1.60-2.20	3
2.40	9	2.20-2.60	5
2.90	14	2.60-3.20	5
3.35	19	3.20-3.50	5
4.00	26	Not considered, emission	--
5.00	38	current	--
7.00	61	insufficient	--
8.50	80	"	--
10.00	100	"	--

Table 14. Fowler-Nordheim Data for Array with Assumed Distribution of Pin Tip Radii.

V(in V)	I(A)	$10^4/V$	I/V^2
2.28×10^2	3.28×10^{-6}	43.86	6.31×10^{-11}
2.57×10^2	2.10×10^{-5}	38.91	3.18×10^{-10}
2.86×10^2	8.49×10^{-5}	34.96	1.04×10^{-9}
3.14×10^2	2.70×10^{-4}	31.85	2.74×10^{-9}
3.43×10^2	8.02×10^{-4}	29.15	6.82×10^{-9}
3.71×10^2	1.85×10^{-3}	26.95	1.34×10^{-8}
4.00×10^2	3.84×10^{-3}	25.00	2.40×10^{-8}
4.28×10^2	7.40×10^{-3}	23.36	4.04×10^{-8}
4.57×10^2	1.36×10^{-2}	21.88	6.51×10^{-8}
4.86×10^2	2.31×10^{-2}	20.58	9.78×10^{-8}
5.14×10^2	3.78×10^{-2}	19.46	1.43×10^{-7}

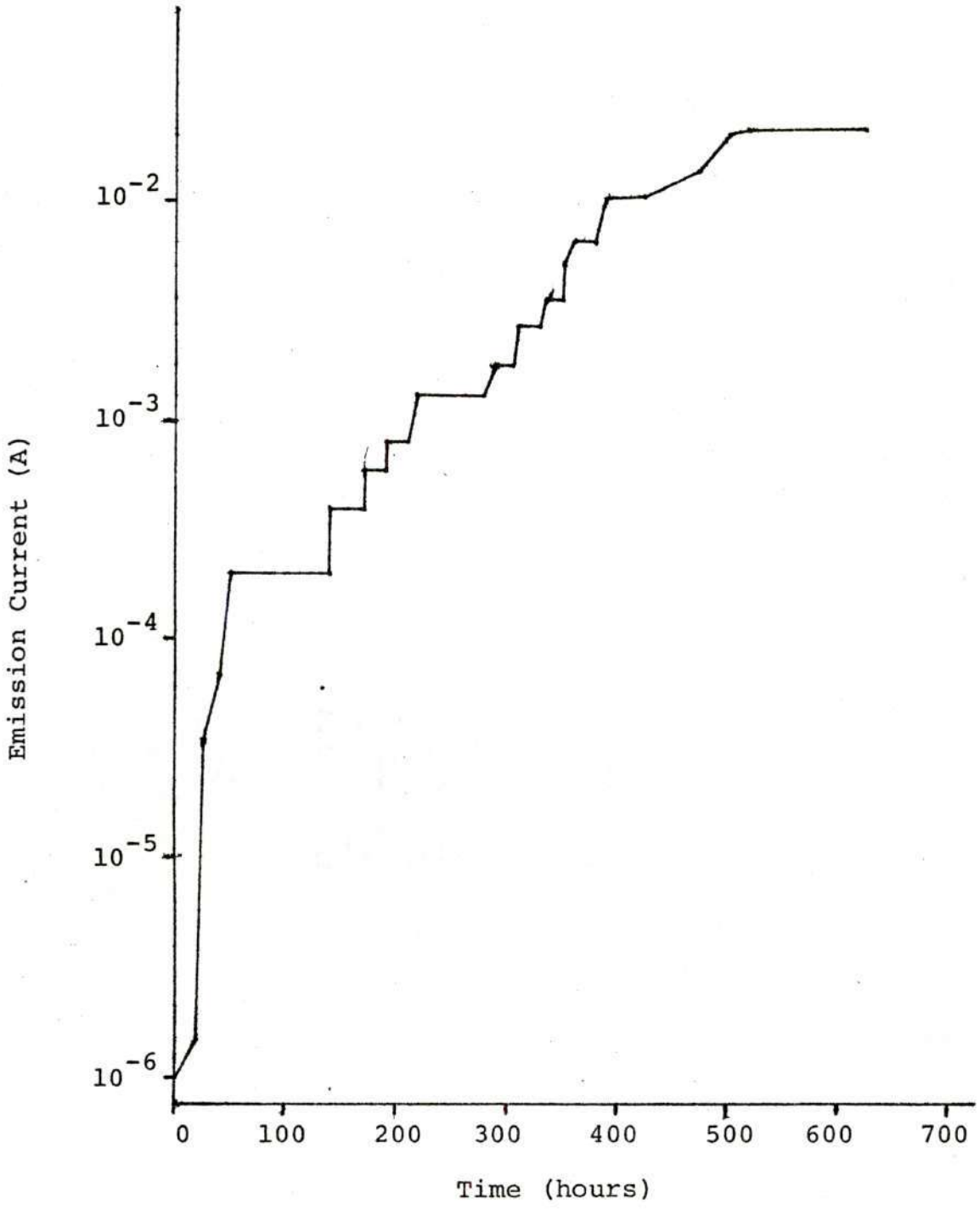

Figure 34. Emission Current versus Time for Sample W-6.

current versus time for the sample considered in the preceding discussion, number W-6, is plotted. This sample achieved a maximum current of 21 mA and maintained this emission for over 100 hours. At the end of this time the experiment was voluntarily terminated. This emission current represents a macroscopic current density of 1.22 A/cm^2. After operation at this level the sample was inspected for emission related damage in the scanning electron microscope. Figure 35 portrays an area displaying the most serious emitter damage observed. Pin destruction of this degree was found over roughly ten percent of the total emission area. It is of interest to note that having experienced this degree of damage the emission performance was essentially unaltered. It is assumed that when some pins are destroyed by excessive emission current, other pins begin to emit.

The macroscopic current density for sample W-6 is noted in Table 15 along with the results for several other samples operated in the water cooled diode. These tests utilized the small anode-large cathode goemetry with the advantage of uniform macroscopic field in the interelectrode space resulting from it as pointed out earlier in this chapter. Only some very general trends can be perceived in these data. In all cases the highest current densities were obtained with samples operated at small interelectrode spacings. The only experimental results in opposition are those of W-8, and it should be noted that this test was terminated by a failure unrelated to the

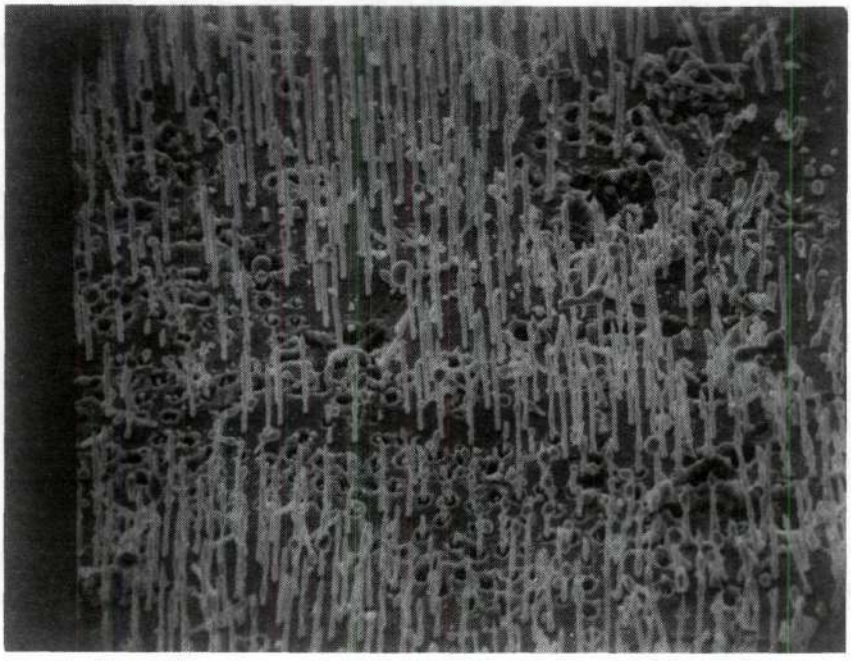

Figure 35. Scanning Electron Micrograph of Emission Damaged Area on Sample W-6 Showing Typical Appearance of Damaged Pins. x1580

Table 15. Summary of Conditions and Results for Several Gross Emission Current Tests Under dc Conditions.

Experiment No.	ρ (pins/cm^2 x 10^{-6})	h(μm)	Tip Shape	d(inches)	Max I(mA) @ V(kV)	J_m(A/cm^2)
W-2	8.7	8	Hemispherical (ion-milled)	0.006	1.5 @ 3.5	0.08
W-6	16.6	8	Pointed	0.001	21.5 @ 0.38	1.22
W-8	7.8	9	Hemispherical (heated)	0.001	2.5 @ 0.80	0.14
W-9	4.4	15	Pointed	0.004	5.4 @ 1.5	0.31
W-10	4.4	10	Pointed	0.001	20.2 @ 0.75	1.15
W-19	1.6	10	Blunt	0.002	10.0 @ 0.85	0.57

emitter.

It was initially felt that the hemispherical pin tips of samples W-2 and W-8 would provide larger emission areas per tip and consequently lower microscopic current densities for given gross emissions. This, however, is not always the case since failure of sample W-2 occurred at an extremely low value. This discrepancy can be understood if the results of the pin tip radius tests are recalled. It was clearly demonstrated that the tip radius observed and measured in micrographs is not the tip radius of the emission areas. In fact all types of tip geometries appear to have the same emission area radii, and failures would be expected at similar macroscopic current densities.

No relationship appears to exist between pin packing density and maximum J_m as opposed to what one would expect from the theoretical descriptions given earlier. However, this result is consistent with the results of the field enhancement factor versus pin packing density study. The only possible support for improved performance from low density samples are the results from W-19.

Sample W-19 was operated as shown in Table 15 without emission related damage, and the test was terminated voluntarily. Results are inconclusive, however, due to the difference in tip goemetry. It is possible that the large pin diameter (~one μm) of this exceptionally low-density sample offers an advantage and further work with samples of this type is warranted. Work

with this sample was limited because this material was available only at the very end of this research. Additionally, this material proved difficult to etch and resisted all efforts to produce suitable pointed pin tip geometries.

Samples W-9 and W-10 deserve special comment. Their unique morphology resulting from growth from a melt whose composition was on the oxide-rich side of the eutectic composition is portrayed in Figure 36. The reasoning leading to the use of this "pot-hole" geometry bears description. It will be recalled that the study of anode-cathode geometries reported at the beginning of this discussion was brought about by observations leading to the conclusions that emission was strongly enhanced at the array edge. This fact was borne out in the theoretical studies. It was thought on this basis that the edges of the pin array surrounding each pot-hole in this unique structure might preferentially emit; and it was thought this would possibly improve the emission uniformity over the sample surface resulting in an increase in J_m. Unfortunately the data in Table 15 shows that this was not the case. It appears that the effect of non-uniform tip geometries was still dominant.

This completes discussion of the gross current dc results, but similar concepts carried over into the testing of emitters under pulsed operating conditions. These results will now be reported and commented upon.

The results of a number of the pulse emission tests are presented in Table 16. All samples except P-12 were operated

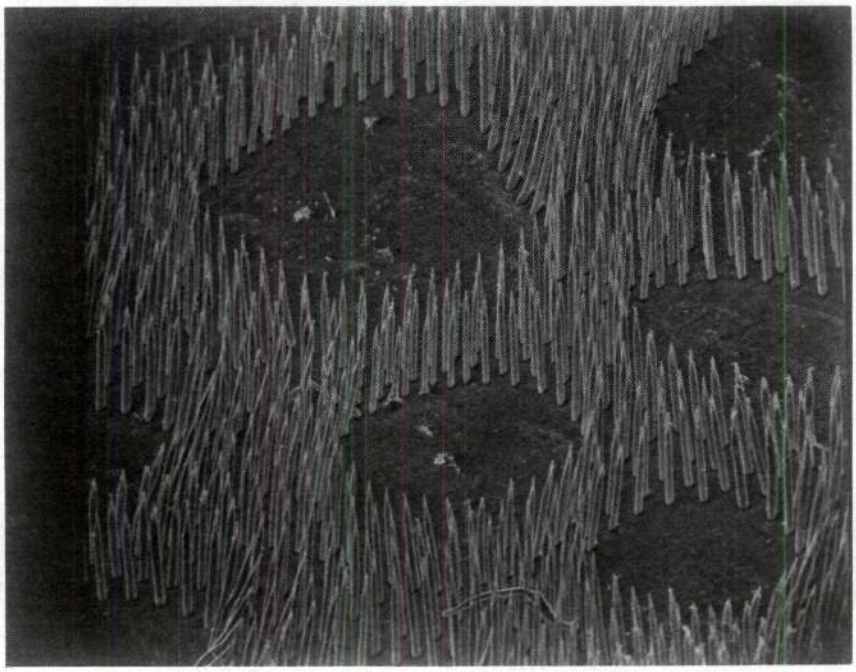

Figure 36. Scanning Electron Micrograph of the Pot-Hole Structure. x1060

Table 16. Summary of Conditions and Results for Several Gross Emission Current Tests Under Pulsed Conditions.

Experiment No.	ρ (pins/cm^2 x 10^{-6})	h(μm)	Tip Shape	d(inches)	Max I(mA) @ V(kV)	J_m(mA/cm^2)
P-3	24.7	10	Pointed	0.355	10 @ 105	34
P-7	7.5	12	Pointed	0.150	18 @ 32	61
P-9	5.8	10	Pointed	0.285	38 @ 107	130
P-11	4.6	9	Pointed	0.050	38 @ 12.9	130
P-12	16.5	10	Pointed	0.200	8.2 @ 60	150

in the guarded cathode geometry of Figure 15 (b); the limitations of this set-up will be discussed subsequently. Sample P-12 was a unique geometry and will receive specific comment.

The samples tested in the pulse mode except for P-12 were nominally 1/4 inch diameter, but minor variations occurred in diameter and consequently in active emitter areas due to individual variations. Values of J_m for each sample are reported in the table, and some possible trends are noticeable. Disregarding experiment P-12, there appears to be an improvement in the maximum J_m as packing density is reduced. This is the only instance in which this effect was noted. It will be recalled that all other tests of this effect gave very inconclusive results. Also the apparent improvement in performance at smaller interelectrode spacings and lower applied voltages is not conclusively supported by these data. Sample P-9 achieved the same results as P-11 at much higher voltage.

The lack of improvement noted in the dc tests of samples W-9 and W-10 using the "pot-hole" structure of Figure 36 was duplicated in pulsed testing. Sample P-11 shared this structure and achieved no better results than the uniform array of sample P-9.

Another approach to utilization of the enhanced edge emission phenomenon is represented by sample P-12. This structure was created by cutting a cross-hatch pattern on the emission surface of a sample, producing an array of about 135 approximately square blocks. A scanning electron micrograph

of this sample is shown in Figure 37. The average area of one of these individual blocks was about 4×10^{-4} cm^2, giving an approximate total emitter area of 5.5×10^{-2} cm^2. Thus the emitter area was only about 18% of the typical 0.3 cm^2 area of the other pulsed emission samples. More importantly, however, the total edge length on the sample was estimated to have been about 4.3 cm compared to the typical circumference of the other samples of two cm. Thus an improvement in performance by a factor of roughly two would be expected. Although an improvement of 15% was observed the measured J_m certainly did not increase by a factor of two. This result further supported the supposition that the principal limitation is non-uniform contribution from individual pins.

One fact that requires explanation is the substantial discrepancy between the reported J_m values for the dc samples and the pulse samples. Sample W-6, the best dc sample, operated at 1.2 A/cm^2 current density, but the best standard geometry pulsed sample (disregarding the unusual geometry of P-12) yielded only 130 mA/cm^2. This difference of approximately a factor of ten is adequately explained by consideration of the effects of edge enhanced emission, and leads to the conclusion that only about ten percent of the area of the pulsed samples in the guarded cathode geometry was emitting effectively.

Although no analytical use was made of Fowler-Nordheim plots from pulsed data two plots are given in Figure 38. These results were obtained at spacings of 0.285 inches and 0.116

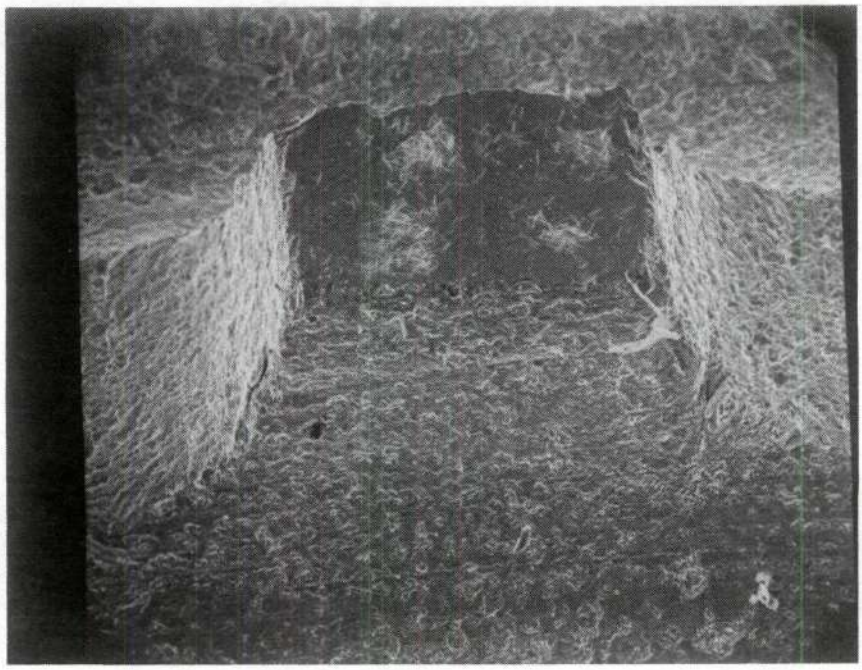

Figure 37. Scanning Electron Micrograph of Sample P-12. x215

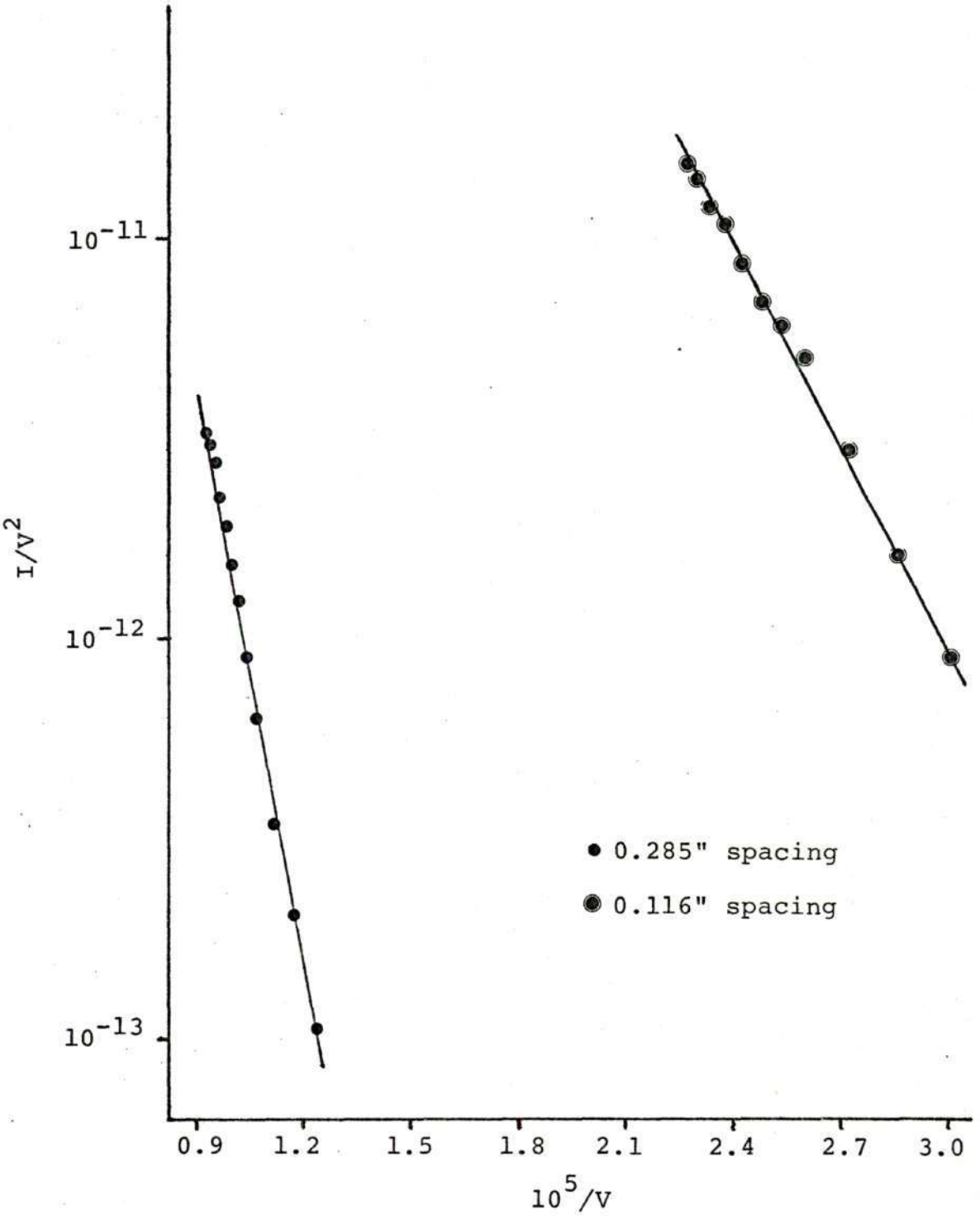

Figure 38. Fowler-Nordheim Curves Plotted from Current and Voltage Decay Traces for Two Interelectrode Spacings, Sample P-9.

inches with sample P-9. The change in slope of the Fowler-Nordheim plots with interelectrode spacing is in qualitative agreement with the results under dc operating conditions at smaller spacings.

The gross emission tests under both dc and pulsed conditions indicate that macroscopic current densities of about 1.2 A/cm^2 represent the present experimental performance limit for the composite arrays. Figure 35 showed the results of exceeding the current limit for an individual pin, and identical failures are observed under both dc and pulsed operation. This failure appears to be caused by overheating of the pin followed by melting and vaporization and in some instances a vacuum arc. The microscopic current density, J', at which damage such as that shown in Figure 35 is estimated to occur can be obtained from Table 11. At the highest applied field, E, of 1.8×10^8 V/cm the current density is 1.28×10^6 A/cm^2. The problem of resistive heating in field emitter tips has been treated by Dolan, et al.[71] These authors present equations for the temperature, T (°C), in conical tips and cylindrical tips as follows,

$$T = 9.5 \times 10^{-4} J^2 r^2 \quad , \quad \text{for conical tips,} \qquad (42)$$

$$T = 2.45 \times 10^{-7} J^2 \quad , \quad \text{for cylindrical tips.} \qquad (43)$$

Equation (42) is derived specifically for a cone half-angle of 11° and is said to err by no more than a factor of three for half-angles from five to 20°. The cylindrical tip is a limiting

case for very small cone angles, i.e., approaching a half-angle of 0°. The half angle of the pins in sample W-6 is about four degrees, and the measurable tip radius is about 400 Å. Calculation of T using equation (42) indicates a negligible temperature rise, but is probably in error by a considerable amount as a result of the small cone half-angle. Equation (43) yields a $T = 4 \times 10^5$ °C, which is obviously a poor estimate. The actual temperature is difficult to estimate, but is certainly sufficient to promote some vaporization of adsorbed gases from the pin surface if it is not sufficiently high to cause melting. This vaporization could promote arcing and pin melting by ion formation in the immediate vicinity of the tip.[72]

Pulsed operation of the emitters in this study did not produce detectable increases in the current density limit as reported by the aforementioned authors.[71] This is consistent with their results, however, since voltage pulse widths were considerably greater than the one microsecond maximum reported to be necessary to increase the current density limit.

This completes the presentation and discussion of the experimental results obtained in this study. The performance limits of the composite emitter arrays have been presented, and reasons for the inability to operate according to the theoretical predictions have been presented. The conclusions will be summarized in the next chapter, and in the final chapter some recommendations will be made regarding areas in which future research may prove most rewarding.

CHAPTER IV

CONCLUSIONS

Operation of UO_2-W composite emitter arrays at macroscopic current densities up to 1.2 A/cm^2 has been demonstrated. Reliable lifetime figures have not been obtained, but operation at the maximum current density for over 100 hours has been achieved. Based on the extent of damage occurring after 100 hours of operation it is estimated that lifetimes of 1000 to 10000 hours could reasonably be expected.

It was concluded that operation at the lowest possible applied voltages is desirable but not mandatory for realization of the indicated maximum performance level. Inconclusive results were obtained in attempts to relate pin tip radius to performance, since the experimental evidence showed that measured tip radii (as observed by scanning electron microscopy) were not equivalent to the radii of the actual emission sites. Likewise, attempts to relate pin packing density to performance were inconclusive. Little or no effect on performance was observed in varying the pin packing density from 4.4×10^6 to 16.6×10^6 pins/cm^2. Brief experimentation with one sample of 1.6×10^6 pins/cm^2 density yielded promising but inconclusive results.

The greatest uniformity of emission from the cathode arrays was obtained using a small anode-large cathode geometry.

This diode design was shown theoretically to provide the most uniform interelectrode macroscopic field distribution, and was shown to eliminate the strongly edge-enhanced field observed for large anode-small cathode geometries with and without guard rings. This theoretical prediction was conclusively borne out in the experimental findings. Experimentally it was also concluded that the criticality of locating the cathode array relative to the guard ring made this geometry a difficult one to use reliably.

Pulsed and dc mode operation over a range of voltages from 200 V to 110 kV demonstrated the great application flexibility of cathode arrays of the type studied. Failure of pins was concluded to occur at microscopic current densities of 10^6 A/cm^2 in agreement with results of other workers. It was concluded that the pins failed by a resistive heating mechanism resulting in melting, vaporization, and, occasionally, low-impedance vacuum arcs.

Specific quantitative values of the field enhancement factor were obtained for a variety of samples. These values ranged from 5.0×10^3 cm^{-1} to 4.5×10^5 cm^{-1}. Qualitative agreement between the experimental values of the field enhancement factor studied as a function of interelectrode spacing and the Levine model was observed. Strict quantitative agreement was not obtained.

The field enhancement factor varied from 5.03×10^3 cm^{-1} at a spacing of 1.0×10^{-1} cm to 1.18×10^5 cm^{-1} at 5.1×10^{-3}

cm spacing. These values were determined for a sample of 4.1×10^6 pins/cm^2 packing density and with emitting tip radii estimated to be 1.4×10^{-6} cm.

Attempted study of the effect of variation of the pin tip radius from 400 Å to 2000 Å led to the conclusion that the actual radii of the emission sites is between 75 Å and 285 Å. The actual emitter radii are concluded to be independent of the tip morphology and the emitter fabrication technique used. Essentially identical results were observed for blunt etched, pointed etched, hemispherical ion-milled and hemispherical heated tips.

Study of the effect of packing density on the field enhancement factor was similarly inconclusive. The range of densities which could be studied was limited by experimental difficulties, but no effect was detectable over a density range of 7.5×10^6 to 16.6×10^6 pins/cm^2.

A model of the cathode arrays was developed using experimentally determined values of the emission area radii and field enhancement factors. This model is far more realistic than any which has been presented previously. All other theoretical treatments have assumed that the field enhancement factor is determined by the observable pin shape and size and that emission is uniformly obtained over areas approximated by πr^2 with r in the range of 500 Å to 5000 Å. Experimental evidence obtained in the present study shows that the emitting area radii do not approach the dimensions of the pin which

are measurable from photomicrographs. It is concluded that the most probable value of the emitting area radii lies between 75 Å and 285 Å. Thus emitting areas are much smaller than assumed by other investigators. Furthermore the field enhancement factors obtained experimentally are large in comparison with those assumed by other workers based on their over estimate of the emitting area radii.

The model developed in this study predicted macroscopic current densities at operationally feasible fields of over 100 A/cm^2. Failure to experimentally obtain current densities of this order was concluded to be a result of non-uniform current contribution from individual pins of the array. This was assumed to result from the existence of a distribution of pin tip radii, and the effect of such a situation was theoretically modeled. Effects were experimentally observed which could be the result of this phenomenon. The low current densities obtained experimentally are concluded to result from the fact that only the pins of the smallest radii present contribute significant emission current. The percentage of pins contributing is estimated to be approximately one percent.

In summary the operation of the UO_2-W field emission cathode arrays has been demonstrated at levels commensurate with some commercial applications. Performance matching that of the best alternative sources has not been experimentally observed, but reasonable models show that such performance is readily within the capabilities of these arrays. It is

felt that certain directions for future work are indicated on the basis of the findings of this study. These will be briefly outlined in the final chapter of this dissertation.

CHAPTER V

RECOMMENDATIONS

The following recommendations are given in the hope that they can serve to delineate several areas of research that promise to yield the greatest returns. The most immediate need is improvement of the macroscopic current density to levels of approximately ten A/cm^2. This should be readily achieveable by improving the uniformity of emission. The first requirement is to devise techniques by which the actual emitting area morphology can be observed. It is suggested that this might be most easily done by the shadowgraph method in the transmission electron microscope.

Attempts to improve pin tip geometry uniformity by heating (see Appendix G) have not met with success. Operation of the emitters at intermediate temperatures of 200 to 500°C may be beneficial, however. Greater promise for improved results is felt to lie in the application of the field desorption technique.

Application of this technique to multi-pin arrays is reported by Garber, et al.[7], with encouraging results. The field desorption phenomenon and its application to W and oxygen-contaminated W was first described by Müller[65]. The latter author has reported the field strength requirement for desorption as well as giving an indication of desorption rates as a

function of applied field.

Several potential applications of field emitters find them attractive due to the narrowness of the energy distribution of the emitted electrons. Most measurements of the distribution have been accomplished using clean W emitters. It is likely that the contamination of the pins in the composite arrays will broaden the distribution. The extent of this broadening should be determined. No report of the energy distribution broadening for oxygen-coated W was found in the literature, but van Oostrom has reported substantial increases in distribution width for nitrogen on W.[21]

Noise is another important factor in many applications. As noted in the Survey of Literature, noise in field emitters has been studied rather extensively. There is no reason to believe that the composite array type emitters should differ drastically from other field emission sources in their noise characteristics, but documentation of the noise observed from the composite emitters should be an objective.

Another primary consideration in many potential applications is lifetime. Continuous operation at the stipulated performance level is required for up to 50000 hours. The life figures for improved performance cathode arrays should be well demonstrated.

Improvements in performance of the arrays would very likely be observed with samples of lower pin packing density. This is not a necessity since efficient operation of the

present samples would be satisfactory, but reduced operating voltages for comparable current densities would result. Achievement of pin packing densities as low as 5×10^5 pins/cm^2 would probably be beneficial.

A few research areas which promise the greatest rewards in the view of the author have been described. It is hoped that these guidelines will serve other workers well, and the author wishes to express his continuing interest.

APPENDICES

APPENDIX A

TABLES OF CONSTANTS AND NOMENCLATURE

The purpose of this appendix is to provide the reader with a convenient reference summarizing the symbols used in this dissertation and listing the values of appropriate universal constants.

Table 17. Values of Appropriate Universal Constants

Symbol	Definition	Value
e	Proton Charge	4.80325×10^{-10} esu
m	Electron Rest Mass	9.10959×10^{-28} g
h	Planck's Constant	6.62620×10^{-27} erg-sec
$\hbar$	$h/2\pi$	1.05459×10^{-27} erg-sec
k	Boltzmann's Constant	1.38054×10^{-16} erg/^{o}K

Table 18. Nomenclature

Symbol	Meaning
E	Electric Field Strength at Emitter Surface
F	Macroscopic Electric Field Strength (=v/d)
I	Field Emission Current
V	Applied Potential Difference Between Anode and Cathode
d	Interelectrode Spacing between Anode and Multi-pin Array Cathodes
ℓ	Interelectrode Spacing for Single Pin Geometries, Anode to Cathode Distance
r	Emitter Tip Radius
a	Inter-pin Spacing in Array
ρ	Pin Packing Density
h	Pin Height
J	Current Density Referred to Active Emission Area on a Single Pin
J'	Current Density Referred to Active Emission Area and Corrected for Adsorbed Gas Effects
J_m	Macroscopic Current Density--Referred to Total Cathode Array Area
A	Active Emission Area on a Single Pin
ϕ	Emitter Work Function
T	Emitter Temperature
β	Field Enhancement Factor--Relates Field, E, to Applied Voltage, V, units of cm^{-1}

Table 18. Nomenclature (continued)

Symbol	Meaning
ξ	Field Enhancement Factor--Relates Field, E, to Macroscopic Field, F, dimensionless
log	Denotes the Common Logarithm (base 10)
ln	Denotes the Natural Logarithm (base e)
m	Slope of the Fowler-Nordheim Curve
n	Correlation Coefficient for Best Fit Line

APPENDIX B

RAW V-I DATA FROM INTERELECTRODE SPACING TESTS

The purpose of this appendix is to tabulate the V-I data acquired in experiments run to determine the effect of interelectrode spacing on the field enhancement factor. The results of the linear regression analysis used to determine the best fit linear relationship are presented and the value of the slope of the Fowler-Nordheim plot, m, is given. The parameter m was tabulated for each curve in Table 4 and utilizing equation (20) was used to calculate β, the field enhancement factor. Note that in these tables the convention of using Y±X instead of $Yx10^{\pm X}$ has been adopted, e.g., 1.47+3 represents $1.47x10^{3}$ and 1.21-13 represents $1.21x10^{-13}$.

Table 19. V-I Data Set No. 1

Spacing = 0.003" (7.6×10^{-3} cm)

Data Point No.	Applied Voltage (V)	Emission Current (A)	$10^4/V$	I/V^2	$\log (I/V^2)$
1	1.47+3	2.62-7	6.80	1.21-13	-12.916
2	1.58+3	0.89-6	6.33	3.56-13	-12.448
3	1.70+3	1.5 -6	5.88	5.19-13	-12.285
4	1.92+3	0.48-5	5.21	1.30-12	-11.885
5	1.72+3	1.18-6	5.81	3.99-13	-12.399
6	1.58+3	0.52-6	6.33	2.08-13	-12.681
7	1.47+3	2.15-7	6.80	9.95-14	-13.002
8	1.34+3	0.56-7	7.46	3.12-14	-13.506
9	1.92+3	0.48-5	5.21	1.30-12	-11.885
10	1.47+3	1.90-7	6.80	8.79-14	-13.056

Slope, m = -7.03+3

Intercept = 6.25-9

n = 0.985

Table 20. V-I Data Set No. 2

Spacing = 0.005" (1.3×10^{-2} cm)

Data Point No.	Applied Voltage(V)	Emission Current(A)	$10^4/V$	I/V^2	log (I/V^2)
1	3.28+3	1.55-5	3.05	1.44-12	-11.841
2	3.07+3	0.81-5	3.26	8.59-13	-12.066
3	2.85+3	0.31-5	3.51	3.82-13	-12.418
4	2.67+3	2.0 -6	3.74	2.80-13	-12.552
5	2.47+3	0.72-6	4.05	1.18-13	-12.928
6	2.25+3	2.25-7	4.44	4.44-14	-13.352

Slope, m = -1.08+4

Intercept = 2.69-9

n = 0.998

Table 21. V-I Data Set No. 3

Spacing = 0.002" (5.1×10^{-3} cm)

Data Point No.	Applied Voltage (V)	Emission Current (A)	$10^4/V$	I/V^2	log (I/V^2)
1	0.86+3	1.5 -8	11.63	2.03-14	-13.693
2	0.97+3	0.95-7	10.31	1.01-13	-12.996
3	1.14+3	0.87-6	8.77	6.69-13	-12.174
4	1.23+3	2.70-6	8.13	1.78-12	-11.748
5	1.37+3	0.95-5	7.30	5.06-12	-11.296
6	1.58+3	2.74-5	6.33	1.10-11	-10.960
7	1.84+3	0.90-4	5.43	2.66-11	-10.575
8	1.95+3	1.98-4	5.13	5.21-11	-10.283
9	1.97+3	2.98-4	5.08	7.68-11	-10.115
10	0.81+3	1.4 -8	12.34	2.13-14	-13.671

Slope, m = -5.23+3

Intercept = 2.65-8

n = 0.997

Table 22. V-I Data Set No. 4

Spacing = 0.005" (1.3×10^{-2} cm)

Data Point No.	Applied Voltage (V)	Emission Current (A)	$10^4/V$	I/V^2	$\log (I/V^2)$
1	1.73+3	1.55-8	5.78	5.18-15	-14.286
2	1.98+3	0.72-7	5.05	1.84-14	-13.736
3	2.18+3	2.10-7	4.59	4.42-14	-13.355
4	2.40+3	0.84-6	4.17	1.46-13	-12.836
5	2.58+3	2.65-6	3.88	3.98-13	-12.400
6	2.79+3	0.77-5	3.58	9.89-13	-12.005
7	3.22+3	2.73-5	3.10	2.63-12	-11.580
8	3.69+3	0.89-4	2.71	6.54-12	-11.185
9	3.92+3	2.79-4	2.55	1.75-11	-10.757
10	1.67+3	1.55-8	5.99	5.56-15	-14.255

Slope, m = -1.10+4

Intercept = 7.18-9

n = 0.994

Table 23. V-I Data Set No. 5

Spacing = 0.010" (2.5×10^{-2} cm)

Data Point No.	Applied Voltage (V)	Emission Current (A)	$10^4/V$	I/V^2	$\log (I/V^2)$
1	3.20+3	1.50-8	3.12	1.46-15	-14.834
2	3.64+3	0.70-7	2.75	5.28-15	-14.277
3	4.00+3	2.10-7	2.50	1.31-14	-13.882
4	4.43+3	0.86-6	2.26	4.38-14	-13.358
5	4.87+3	2.60-6	2.05	1.10-13	-12.960
6	5.36+3	0.82-5	1.86	2.85-13	-12.544
7	6.06+3	2.90-5	1.65	7.90-13	-12.102
8	6.87+3	0.90-4	1.46	1.91-12	-11.720
9	7.40+3	2.50-4	1.35	4.56-12	-11.340
10	3.22+3	1.80-8	3.10	1.74-15	-14.760

Slope, m = -1.97+4

Intercept = 1.47-9

n = 0.997

Table 24. V-I Data Set No. 6

Spacing = 0.020" (5.1×10^{-2} cm)

Data Point No.	Applied Voltage (V)	Emission Current (A)	$10^4/V$	I/V^2	log (I/V^2)
1	6.63+3	1.5 -8	1.51	3.41-16	-15.467
2	7.50+3	0.92-7	1.33	1.64-15	-14.786
3	8.25+3	2.30-7	1.21	3.38-15	-14.471
4	9.03+3	0.94-6	1.11	1.15-14	-13.938
5	9.41+3	2.55-6	1.06	2.88-14	-13.541
6	10.48+3	0.85-5	0.954	7.74-14	-13.111
7	12.10+3	2.70-5	0.826	1.84-13	-12.734
8	13.57+3	0.72-4	0.737	3.91-13	-12.408
9	6.63+3	0.52-8	1.51	1.18-16	-15.927

Slope, m = -4.10+4

Intercept = 4.64-10

n = 0.995

Table 25. V-I Data Set No. 7

Spacing = 0.030" (7.6×10^{-2} cm)

Data Point No.	Applied Voltage (V)	Emission Current (A)	$10^4/V$	I/V^2	$\log (I/V^2)$
1	9.68+3	0.44-8	1.03	4.70-17	-16.328
2	10.66+3	2.45-8	0.938	2.16-16	-15.666
3	11.48+3	0.75-7	0.871	5.69-16	-15.245
4	12.41+3	2.75-7	0.806	1.78-15	-14.748
5	13.42+3	0.82-6	0.745	4.55-15	-14.342
6	14.64+3	2.30-6	0.682	1.07-14	-13.970
7	9.32+3	0.48-8	1.07	5.52-17	-16.258

Slope, m = -6.83+4

Intercept = 5.27-10

n = 0.999

Table 26. V-I Data Set No. 8

Spacing = 0.040" (1.0×10^{-1} cm)

Data Point No.	Applied Voltage(V)	Emission Current(A)	$10^4/V$	I/V^2	log (I/V^2)
1	13.35+3	0.4 -8	0.749	2.24-17	-16.649
2	14.73+3	2.3 -8	0.679	1.06-16	-15.975
3	15.30+3	0.4 -7	0.654	1.71-16	-15.767
4	17.02+3	2.3 -7	0.588	7.94-16	-15.100
5	18.20+3	0.58-6	0.549	1.75-15	-14.757
6	13.22+3	0.65-8	0.756	3.72-17	-16.430

Slope, m = -9.51+4

Intercept = 2.97-10

n = 0.999

Table 27. V-I Data Set No. 9

Spacing = 0.002" (5.1×10^{-3} cm)

Data Point No.	Applied Voltage (V)	Emission Current (A)	$10^4/V$	I/V^2	log (I/V^2)
1	0.67+3	0.50-8	14.92	1.11-14	-13.953
2	0.72+3	1.8 -8	13.89	3.47-14	-13.459
3	0.81+3	0.93-7	12.34	1.42-13	-12.848
4	0.86+3	2.40-7	11.63	3.24-13	-12.489
5	0.95+3	0.82-6	10.53	9.08-13	-12.042
6	1.05+3	2.45-6	9.52	2.22-12	-11.653
7	1.16+3	0.77-5	8.62	5.72-12	-11.242
8	1.32+3	2.47-5	7.58	1.42-11	-10.848
9	1.58+3	0.78-4	6.33	3.12-11	-10.505
10	1.80+3	2.45-4	5.56	7.56-11	-10.121
11	0.72+3	0.38-8	13.89	7.33-15	-14.135

Slope, m = -4.05+3

Intercept = 1.49-8

n = 0.999

Table 28. V-I Data Set No. 10

Spacing = 0.005" (1.3×10^{-2} cm)

Data Point No.	Applied Voltage (V)	Emission Current (A)	$10^4/V$	I/V^2	log (I/V^2)
1	1.66+3	0.32-8	6.02	1.16-15	-14.935
2	1.88+3	2.75-8	5.32	7.78-15	-14.109
3	2.13+3	0.82-7	4.69	1.81-14	-13.743
4	2.25+3	2.5 -7	4.44	4.94-14	-13.306
5	2.47+3	0.90-6	4.05	1.48-13	-12.831
6	2.63+3	2.90-6	3.80	4.19-13	-12.378
7	2.86+3	0.83-5	3.50	1.01-12	-11.994
8	3.23+3	2.60-5	3.10	2.49-12	-11.603
9	3.67+3	0.84-4	2.72	6.24-12	-11.205
10	3.95+3	2.75-4	2.53	1.76-11	-10.754
11	1.65+3	0.7 -8	6.06	2.57-15	-14.590

Slope, m = -1.19+4

Intercept = 1.24-8

n = 0.995

APPENDIX C

RAW V-I DATA FROM PIN TIP RADIUS TESTS

The purpose of this appendix is to tabulate the V-I data acquired in experiments run to ascertain the effect of the pin tip radius on the field enhancement factor. The results of the linear regression analysis used to determine the best fit linear relationship are presented, and the value of the slope of the Fowler-Nordheim plat, m, is given. The parameter m was tabulated for each curve in Table 6 and utilizing equation (20) was used to calculate β, the field enhancement factor. Note that in these tables the convention of using Y±X instead of $Yx10^{\pm X}$ has been adopted, e.g., 1.47+3 represents $1.47x10^{3}$ and 1.21-13 represents $1.21x10^{-13}$.

Table 29. V-I Data Set for Sample R-1

Data Point No.	Applied Voltage(V)	Emission Current(A)	$10^4/V$	I/V^2	log (I/V^2)
1	2.82+3	1.92-4	3.55	2.41-11	-10.617
2	2.68+3	1.60-4	3.73	2.23-11	-10.652
3	2.60+3	1.26-4	3.85	1.86-11	-10.730
4	2.57+3	9.0 -5	3.89	1.36-11	-10.866
5	2.41+3	5.9 -5	4.15	1.02-11	-10.993
6	2.19+3	3.0 -5	4.57	6.26-12	-11.204
7	1.81+3	7.0 -6	5.52	2.14-12	-11.670

Slope, m = -5.48+3

Intercept = 2.14-9

n = 0.991

Table 30. V-I Data Set for Sample R-2

Data Point No.	Applied Voltage(V)	Emission Current(A)	$10^4/V$	I/V^2	log (I/V^2)
1	2.75+3	2.1 -4	3.64	2.78-11	-10.556
2	2.65+3	1.5 -4	3.77	2.14-11	-10.670
3	2.48+3	9.0 -5	4.03	1.46-11	-10.835
4	2.17+3	4.1 -5	4.61	8.71-12	-11.060
5	2.00+3	1.8 -5	5.00	4.50-12	-11.347
6	1.86+3	1.3 -5	5.38	3.76-12	-11.425

Slope, m = -5.03+3

Intercept = 1.70-9

n = 0.992

Table 31. V-I Data Set for Sample R-3

Data Point No.	Applied Voltage (V)	Emission Current (A)	$10^4/V$	I/V^2	log (I/V^2)
1	1.71+3	1.61-4	5.85	5.50-11	-10.259
2	1.58+3	9.65-5	6.33	3.86-11	-10.413
3	1.48+3	6.95-5	6.76	3.17-11	-10.498
4	1.22+3	1.77-5	8.20	1.19-11	-10.925
5	0.95+3	1.5 -6	10.53	1.66-12	-11.779

Slope, m = -3.24+3

Intercept = 4.60-9

n = 0.997

APPENDIX D

RAW V-I DATA FROM PIN PACKING DENSITY TESTS

The purpose of this appendix is to tabulate the V-I data acquired in experiments run to delineate the effect of the pin packing density on the field enhancement factor. The results of the linear regression analysis used to determine the best fit linear relationship are presented, and the value of the slope of the Fowler-Nordheim plot, m, is given. The parameter m was tabulated for each curve in Table 9 and utilizing equation (20) was used to calculate β, the field enhancement factor. Note that in these tables the convention of using $Y \pm X$ instead of $Y \times 10^{\pm X}$ has been adopted, e.g., 1.47+3 represents 1.47×10^{3} and 1.21-13 represents 1.21×10^{-13}.

Table 32. V-I Data Set for Sample D-1

Data Point No.	Applied Voltage (V)	Emission Current (A)	$10^4/V$	I/V^2	log (I/V^2)
1	0.720+3	1.39-3	13.89	2.68-9	- 8.572
2	0.617+3	0.58-3	16.21	1.52-9	- 8.817
3	0.536+3	2.48-4	18.66	8.63-10	- 9.064
4	0.450+3	0.76-4	22.22	3.75-10	- 9.426
5	0.385+3	2.35-5	25.97	1.58-10	- 9.800
6	0.350+3	0.96-5	28.57	7.84-11	-10.106
7	0.298+3	2.70-6	33.56	3.04-11	-10.517
8	0.278+3	0.79-6	35.97	1.02-11	-10.990

Slope, m = -1.05+3

Intercept = 7.95-8

n = 0.997

Table 33. V-I Data Set for Sample D-2

Data Point No.	Applied Voltage(V)	Emission Current(A)	$10^4/V$	I/V^2	$\log(I/V^2)$
1	0.538+3	1.24-3	18.59	4.28-9	- 8.368
2	0.498+3	0.68-3	20.08	2.74-9	- 8.562
3	0.402+3	2.06-4	24.88	1.27-9	- 8.894
4	0.350+3	0.72-4	28.57	5.88-10	- 9.231
5	0.306+3	2.05-5	32.68	2.19-10	- 9.660
6	0.271+3	0.60-5	36.90	8.17-11	-10.088
7	0.246+3	1.75-6	40.65	2.89-11	-10.539

Slope, m = -9.60+2

Intercept = 2.75-7

n = 0.998

APPENDIX E

RAW V-I DATA FOR EXPERIMENTAL FOWLER-NORDHEIM PLOT, SAMPLE W-6

This appendix presents the raw V-I data acquired from sample W-6. These data were used to calculate values of β and r for use in derivation of the theoretical model described in Chapter III. The Fowler-Nordheim plot derived from these data is presented in Figure 31. Note that in this table the convention of using Y±X instead of $Yx10^{\pm X}$ has been adopted, e.g., 1.47+3 represents $1.47x10^{3}$ and 1.21-13 represents $1.21x10^{-13}$.

Table 34. V-I Data Set for Sample W-6

Data Point No.	Applied Voltage (V)	Emission Current (A)	$10^4/V$	I/V^2	$\log (I/V^2)$
1	0.509+3	2.78-3	19.6	1.07-8	- 7.969
2	0.471+3	1.49-3	21.2	6.72-9	- 8.173
3	0.431+3	0.72-3	23.2	3.85-9	- 8.415
4	0.389+3	0.38-3	25.7	2.51-9	- 8.600
5	0.364+3	2.52-4	27.5	1.90-9	- 8.721
6	0.340+3	1.48-4	29.4	1.28-9	- 8.893
7	0.324+3	0.98-4	30.9	9.34-10	- 9.030
8	0.307+3	0.62-4	32.6	6.58-10	- 9.182
9	0.291+3	0.36-4	34.4	4.25-10	- 9.371
10	0.283+3	2.23-5	35.3	2.78-10	- 9.555
11	0.264+3	0.96-5	37.9	1.38-10	- 9.861
12	0.250+3	0.45-5	40.0	7.20-11	-10.143
13	0.242+3	2.48-6	41.3	4.23-11	-10.373

Slope, m = -1.36+3

Note: For this data set m was calculated using data points 8-13 only because of non-linear behavior of curve at higher voltage and current (see Figure 31).

APPENDIX F

RAW V-I DATA FOR EXPERIMENTAL FOWLER-NORDHEIM PLOTS, SAMPLE P-9

This appendix presents the raw V-I data obtained for pulsed operation of sample P-9 at two different inter-electrode spacings. The Fowler-Nordheim plots derived from these data sets are presented in Figure 38. Note that in these tables the convention of using Y±X instead of $Yx10^{\pm X}$ has been adopted, e.g., 1.47+3 represents $1.47x10^{3}$ and 1.21-13 represents $1.21x10^{-13}$.

Table 35. V-I Data Set for Sample P-9

at 0.285" Spacing

Data Point No.	Applied Voltage (V)	Emission Current (A)	$10^5/V$	I/V^2	log (I/V^2)
1	107.5+3	37.5-3	0.93	3.23-12	-11.491
2	106.4+3	34.5-3	0.94	3.05-12	-11.516
3	105.3+3	30.3-3	0.95	2.73-12	-11.564
4	104.2+3	24.4-3	0.96	2.26-12	-11.646
5	102.0+3	19.9-3	0.98	1.91-12	-11.719
6	100.0+3	15.2-3	1.00	1.52-12	-11.818
7	98.0+3	11.6-3	1.02	1.21-12	-11.917
8	96.2+3	8.4-3	1.04	9.05-13	-12.043
9	93.4+3	5.5-3	1.07	6.34-13	-12.198
10	89.3+3	2.8-3	1.12	3.50-13	-12.456
11	84.7+3	1.5-3	1.18	2.08-13	-12.682
12	80.6+3	0.7-3	1.24	1.07-13	-12.971

Slope, m = -4.87+5

Intercept = 1.10-7

n = 0.999

Table 36. V-I Data Set for Sample P-9 at 0.116" Spacing

Data Point No.	Applied Voltage (V)	Emission Current (A)	$10^5/V$	I/V^2	$\log (I/V^2)$
1	44.0+3	29.5-3	2.27	1.52-11	-10.818
2	43.8+3	28.8-3	2.28	1.50-11	-10.824
3	43.5+3	26.1-3	2.30	1.38-11	-10.860
4	42.9+3	22.3-3	2.33	1.21-11	-10.917
5	42.0+3	18.6-3	2.38	1.06-11	-10.975
6	41.2+3	15.0-3	2.43	8.80-12	-11.056
7	40.3+3	11.4-3	2.48	7.02-12	-11.154
8	39.4+3	9.4-3	2.54	6.08-12	-11.216
9	38.5+3	7.5-3	2.60	5.10-12	-11.292
10	36.8+3	4.0-3	2.72	2.99-12	-11.524
11	35.0+3	2.0-3	2.86	1.61-12	-11.793
12	33.2+3	1.0-3	3.01	9.03-13	-12.044

Slope, m = -1.64+5

Intercept = 8.48-8

n = 0.998

APPENDIX G

REPORT OF PRELIMINARY HEATING AND FIELD DESORPTION TEST RESULTS

The purpose of this appendix is to report the results of a few cursory experiments involving heated operation of the field emission cathode and attempts to improve the pin tip uniformity by field desorption.

Heated Operation

Two testing procedures were used in this part of the research. The first sample was operated under dc conditions for approximately 100 hours at an emission current of 5 mA and an applied voltage of 11.8 kV. The power input to the anode (about 60 W) was sufficient to heat it to 1000°C (visual estimate). Without shutting the emitter off a set of V-I data was taken. This was done as quickly as possible to minimize the spacing change resulting from anode cooling as the power input decreased. The interelectrode spacing was 0.019 $\pm$ 0.001 inches. The Fowler-Nordheim plot for this data showed a slope, $m = -9.00 \times 10^{4}$, and an intercept value of 1.80×10^{-3}.

After cooling to room temperature the diode spacing was set at 0.020" and another V-I data set was obtained. The Fowler-Nordheim plot of this data was significantly different

from that obtained previously. The slope for this plot was -4.32×10^{4} and the intercept was 1.58×10^{-8}. The large difference in the slope values of these plots is probably significant, but interpretation is difficult. A decrease in the work function would be expected as a result of desorption of contaminants. This change would probably not be large and would result in a decreased slope rather than the increased value actually observed. Therefore a change in the field enhancement factor is indicated. To promote the observed change in the slope, assuming no change in work function, the field enhancement factor would have to decrease by a factor of 2.1. This is not an unreasonable change to expect from rounding of small surface protrusions.

Following this test the sample was operated for an additional 16 hours under similar conditions to those used for the previous 100 hours of operation. A Fowler-Nordheim plot for the sample obtained in identical fashion to that reported first showed a slope of -5.69×10^{4} and an intercept of 3.01×10^{-6}. Once again operation was terminated, the sample was allowed to cool, and another data set was obtained. These results closely agreed with the data previously reported for the cold sample. The smaller change in the slope and intercept observed in this second test is not readily interpreted.

Stability of the emission current was excellent throughout the entire sequence of tests, and further tests of

other types were run with this sample. Unfortunately the sample was destroyed by a large vacuum arc before it was removed from the test diode, and no assessment of a possible change in pin tip morphology was possible.

In the second test a composite cathode was mechanically clamped to a heater unit intended for a dispenser cathode assembly. This allowed the cathode array to be heated to an optical temperature (uncorrected) of about 800°C. At temperatures of 700-800°C operation was unstable with arcing periodically observed. No increase in the slope of the Fowler-Nordheim plot was noted for this sample. In fact the slope dropped from -1.10×10^4 (at RT) to -6.43×10^3 for operation at 730°C. The inconsistency of these results with those described above confuses the situation considerably. It should be noted that the actual temperature of the pins in the first test was unknown. There are indications that the temperature rise of the pins may be quite small under such conditions, and perhaps this operation at somewhat lower temperatures than those used in the later test is beneficial.

Field Desorption

For this test sample P-12 described in the thesis text was used. Operating at a spacing of 0.080" a V-I data set was obtained which yielded a Fowler-Nordheim plot slope of -3.20×10^4. The maximum current was 1.9 mA at 19.6 kV. An applied voltage of 8.5 kV gave an emission current of 2.55 x

10^{-6} A. The polarity of diode operation was subsequently reversed and a voltage of +13.7 kV was applied to the array relative to the opposite electrode. At this voltage a current of 2.5×10^{-6} A was measured. This current increased rapidly with increasing voltage and appeared to be a field emission current. It probably is obtained from microprotrusions on the electrode surface. In order to avoid breakdown and damage to the array, the experiment was terminated after the reverse polarity voltage had been applied for a total of 12 minutes.

The diode was then returned to the polarity of normal operation, and another data set was obtained. The Fowler-Nordheim plot of this data had a slope of -5.48×10^{4}. Thus an increase in slope by a factor of 1.7 was seen. It is felt that the field applied during the desorption test was probably not sufficiently high to remove oxygen or tungsten from the pins. Müller[65] has reported a field of 5×10^{8} V/cm to be necessary, a value several times that required to obtain field emission from the array used here. However, it is apparent that the voltage applied during desorption was less than that used for field emission. Larger voltages could not be applied during desorption because of the danger of damage to the array should an arc have occurred.

In order to satisfactorily apply the field desorption technique, it is felt that the anode will require some sort of conditioning to remove potential emission sites.

BIBLIOGRAPHY

1. R. W. Wood, Phys. Rev., 5, 1 (1897).

2. R. H. Fowler and L. W. Nordheim, Proc. R. Soc. Lond., A119, 173 (1928).

3. L. W. Nordheim, Proc. R. Soc. Lond., A121, 626 (1928).

4. W. P. Dyke and W. W. Dolan, Advances in Electronics and Electron Physics, 8, 89 (1956).

5. W. P. Dyke, Scientific American, 210, 108 (January 1964).

6. Ye. G. Shirokov, Radiotekh. Elektron. [Radio Eng. Electron. Phys.], 9, 1091 (1964).

7. R. I. Garber, et al., Prib. Tekh. Eksp. [Instrum. Exp. Tech.], 12, 213 (1969).

8. B. V. Okulov, et al., Prib. Tekh. Eksp. [Instrum. Exp. Tech.], 16, 1759 (1973).

9. S. P. Bugaev, et al., Prib. Tekh. Eksp. [Instrum. Exp. Tech.], 17, 485 (1974).

10. C. A. Spindt, et al., J. Appl. Aphys., 47, 5248 (1976).

11. H. E. Cline, J. Appl. Phys., 41, 76 (1970).

12. H. Pfleiderer and H. Pehme, Phys. Status Solidi, A11, 153 (1972).

13. R. K. Feeney, et al., J. Appl. Phys., 46, 1841 (1975).

14. R. K. Feeney, W. L. Ohlinger, A. T. Chapman and J. K. Cochran, "Investigation of Field Emission Electron Gun for Gas Lasers," Final Report, U. S. Army Missle Command Contract DAAH01-74-C-0229, Georgia Institute of Technology, Schools of Ceramic and Electrical Engineering, April 1976.

15. A. T. Chapman, et al., "Melt-Grown Oxide-Metal Composites," Final Technical Report (Report No. 6), ARPA Contract DAAH01-71-C-1046, Georgia Institute of Technology, School of Ceramic Engineering, December 1973.

16. E. Kemble, The Fundamental Principles of Quantum Mechanics, McGraw-Hill, New York, N. Y., 1937.

17. R. E. Burgess, H. Kroemer and J. M. Houston, Phys. Rev., 90, 515 (1953).

18. R. H. Good and E. W. Mueller, Handbuch der Physik, Springer-Verlag, Berlin, 1956, Volume 21.

19. E. L. Murphy and R. H. Good, Jr., Phys. Rev., 102, 1464 (1956).

20. R. D. Young, Phys. Rev., 113, 110 (1959).

21. A. G. J. van Oostrom, Phillips Res. Rep. Supplement, 1, 1 (1966).

22. W. Schottky, Ann. Phys. IV, 57, 541 (1918).

23. C. Kleint and H. Gasse, Z. Naturforsch., A15, 87 (1960).

24. C. Kleint and H. Gasse, Forschr. Phys., 13, 499 (1965).

25. C. Kleint, Surf. Sci., 25, 394 (1971); 25, 411 (1971).

26. R. Gomer, Surf. Sci., 38, 373 (1973).

27. L. W. Swanson and N. A. Martin, J. Appl. Phys., 46, 2029, (1975).

28. E. W. Mueller, Z. Phys., 108, 668 (1938).

29. R. Haefer, Z. Phys., 116, 604 (1940).

30. J. A. Becker, Bell Syst. Tech. J., 30, 907 (1951).

31. M. Drechsler and E. Henkel, Z. Angew. Phys., 6, 341 (1954).

32. W. P. Dyke, et al., J. Appl. Phys., 24, 570 (1953).

33. F. M. Charbonnier, private communication to R. Gomer reported in Field Emission and Field Ionization, Harvard University Press, Cambridge, Mass., 1961, Chapter 2, p. 45.

34. J. D. Levine, Surface Science, 10, 313 (1968).

35. J. D. Levine, RCA Rev. (Radio Corp. Am.), 32, 144 (1971).

36. A. T. Chapman, et al., "Melt-Grown Oxide-Metal Composites," Reports 3 thru 6, ARPA Contract DAAH01-71-C-1046, Georgia Institute of Technology, School of Ceramic Engineering, June 1971 thru December 1973.

37. W. P. Dyke, IRE Trans. Mil. Electron., Mil-4, 38 (1960).

38. G. N. Fursei, et al., Zh. Tekh. Fiz. [Sov. Phys.-Tech. Phys.], 17, 837 (1972).

39. I. Z. Gleizer and B. V. Okulov, Prib. Tekh. Eksp. [Instrum. Exp. Tech.], 16, 1214 (1973).

40. A. T. Chapman, et al., "Melt-Grown Oxide-Metal Composites," Reports 1 and 2, ARPA Contract DAAH01-70-C-1057, Georgia Institute of Technology, School of Ceramic Engineering, June 1970 to June 1971.

41. B. A. Keener, "An Experimental Investigation of the Emission from Oxide-Metal Composite Field Electron Emitters," Masters Thesis, School of Electrical Engineering, Georgia Institute of Technology, August 1974.

42. A. T. Chapman, et al., "Manufacturing Methods for Production of Field Effect Electron Emitters," U. S. Army Missle Command Contract DAAH01-75-C-0852, Final Report, Georgia Institute of Technology, School of Ceramic Engineering, to be published November 1977.

43. J. K. Cochran, et al., "Manufacturing Methods for the Production of Low Voltage Field Emitters," U. S. Army Missle Command Contract DAAK40-77-0096, Georgia Institute of Technology, School of Ceramic Engineering, April 1977 to October 1978.

44. C. L. Shackelford, "Long Life X-Ray Tubes for Portable Sources," U. S. Army Electronics Command Report ECOM-75-1334-F, ITT Electron Tube Division, Easton, Pa., August 1976.

45. C. Cason, G. J. Dezenberg and R. J. Huff, Appl. Phys. Lett., 23, 110 (1973).

46. C. D. Hendricks and S. Kassel, "Soviet Development of Needle-Tip Field Emission Cathodes for High Current Electron Beams," Rand External Report R-1311-ARPA, Rand Corporation, Santa Monica, Calif., July 1973.

47. C. A. Robinson, Aviation Week and Space Technology, 106, 16 (May 2, 1977).

48. C. M. Bowden, et al., Nucl. Instrum. Methods, 116, 201 (1974).

49. W. C. Wetmore, Aviation Week and Space Technology, 107, 22 (July 4, 1977).

50. J. D. Levine, (RCA Corporation), U. S. Patent No. 3921022, November 18, 1975.

51. T. Elfe, Georgia Tech Engineering Experiment Station, Atlanta, Georgia, private communication.

52. B. Smith, U. S. Army Electronics Command, Fort Monmouth, New Jersey, private communication.

53. R. E. Hughes and W. L. Ohlinger, Semicon Associates, Lexington, Kentucky, private communication.

54. A. T. Chapman, et al., J. Am. Ceram. Soc., 53, 60 (1970).

55. M. D. Watson, et al., J. Am. Ceram. Soc., 53, 112 (1970).

56. A. T. Chapman and G. W. Clark, J. Am. Ceram. Soc., 48, 494 (1965).

57. A. Bassi and G. Camona, Energia Nuclare, 10, 277 (1963).

58. A. J. Manley, J. Nucl. Mater., 15, 143 (1965).

59. A. T. Chapman, et al., "Melt-Grown Oxide-Metal Composites," Report 3, ARPA Contract DAAH01-71-C-1046, Georgia Institute of Technology, School of Ceramic Engineering, June 1971 to December 1971.

60. T. Y. S. Lin, "Orientational Relationships in Unidirectionally Solidified UO_2-W Composites," Masters Thesis, School of Ceramic Engineering, Georgia Institue of Technology, December 1971.

61. D. Robbins, Metallurgia, 55, 257 (1957).

62. B. V. Bondarenko, Zh. Tekh. Fiz. [Sov. Phys.-Tech. Phys.], 18, 1538 (1974).

63. E. W. Mueller, Z. Elektrochem., 59, 372 (1955).

64. J. A. Becker and R. G. Brandes, J. Chem. Phys., 23, 1323, (1955).

65. E. W. Mueller, Phys. Rev., 102, 618 (1956).

66. R. Gomer and J. K. Hulm, J. Chem. Phys., 27, 1363 (1957).

67. T. H. George and P. M. Stier, J. Chem. Phys., 37, 1935 (1962).

68. D. Menzeland R. Gomer, J. Chem. Phys., 41, 3311 (1964).

69. R. Gomer, Field Emission and Field Ionization, Harvard University Press, Cambridge, Mass., 1961, Chapter 2, p. 45.

70. J. P. Barbour, et al., Phys. Rev., 92, 45 (1953).

71. W. W. Dolan, et al., Phys. Rev., 91, 1054 (1953).

72. E. W. Webster, et al., J. Appl. Phys., 23, 264 (1952).

VITA

Wayne Laurance Ohlinger

October 3, 1944	-	Born - Lake Wales, Florida
June, 1962	-	Graduated Lake Wales High School, Lake Wales, Florida
1962-1968	-	Attended Georgia Institute of Technology
June, 1968	-	Bachelor of Ceramic Engineering, Georgia Institute of Technology, Atlanta, Georgia
1968-1971	-	Employed with Control Data Corporation, Minneapolis, Minnesota as Associate Scientist
1971-1977	-	Attended Georgia Institute of Technology, Employed as Graduate Research and Teaching Assistant
June, 1974	-	M. S. Ceramic Engineering, Georgia Institute of Technology, Atlanta, Georgia
September, 1977	-	Ph. D. Ceramic Engineering, Georgia Institute of Technology, Atlanta, Georgia

Publications and Presentations

"Investigation of Field Emission Electron Guns for Gas Lasers," Final Report, Army Missile Command, 1 April 1976.

"Pulsed Field Emission from Unidirectionally Solidified UO_2-W Emitter Structures," presentation at the American Ceramic Society, Southeastern Section Meeting, Gatlinburg, Tennessee, June, 1975.

"Melt-Grown Oxide-Metal Composites," Reports 2 through 6, Advanced Research Project Agency, Department of Defense, June, 1971-Demember, 1973.

"Selective Chemical Etching of Melt-Grown UO_2-W Composites for Electron Emitter Applications," presentation at the American Ceramic Society Annual Meeting, Cincinnati, Ohio, May, 1973.

"Thermogravimetric Studies of a Synthetic Hydroxyapatite," Bachelor of Ceramic Engineering thesis, Georgia Institute of Technology, June, 1968.

Fields of Study and Interests

Major - Ceramic Engineering
Minor - Metallurgy

Magnetic and electronic properties of ceramics and glasses.
Oxide-metal and oxide-oxide composites.
Phase equilibria.
Crystalline and non-crystalline structures.